PHOTODISSOCIATION AND REACTION DYNAMICS OF CHLORINE-CONTAINING SPECIES IMPORTANT IN STRATOSPHERIC OZONE CHEMISTRY

Thesis by

Christine Marie Nelson

In Partial Fulfillment of the Requirements

for the Degree of

Doctor of Philosophy

California Institute of Technology

Pasadena, California

1994

(Submitted October 15, 1993)

If I had waited long enough I probably never would have written anything at all since there is a tendency when you really begin to learn something about a thing not to want to write about it but rather to keep on learning about it always and at no time, unless you are very egotistical, which, of course, accounts for many books, will you be able to say: now I know all about this and will write about it. Certainly I do not say that now: every year I know there is more to learn, but I know some things which may be interesting now, and I may be away from the bull fights for a long time and I might as well write what I know about them now.

- Ernest Hemingway, *Death in the Afternoon*

ACKNOWLEDGMENTS

I dedicate this thesis to the memory of my grandfather, Folke Nelson. He emigrated to the United States in 1923 with dreams of getting a college education. Due to circumstances, he was never able to complete his university degree. However, because of his belief in an education, he supported all his children through college and ensured that all his grandchildren would have the same opportunity.

The conferment of a degree is not only the achievement of the student but also the accomplishment of many educators. Writing these acknowledgments gives me the opportunity to look back and thank many teachers and mentors who have encouraged, motivated and supported me throughout the years of my academic education.

I especially want to thank Mitchio Okumura for letting an Environmental Engineering student join his group five years ago and having the openmindedness and enthusiasm to work with me to find a project that was of mutual interest. I appreciate all of the support and encouragement he provided me throughout the endeavor; he was always willing to answer questions and help troubleshoot the inevitable problems inherent with experimentation. Mitchio is an exceptional scientist with many interesting ideas. I learned a lot working in his lab over the past few years and am sure that many generations of students will benefit from his mentorship and teaching.

Before coming to Caltech, many other people also helped me along the road. James Johnson, Roger McCarter and John Burke were all generous enough to open their labs to a young student which gave me my first tastes of working in a laboratory. Their support and enthusiasm of my work definitely influenced my decision to attend graduate school. Sharon Bartels, Elaine Patterson, Fred Stampa and John Burke taught me many of the basics. I can remember sitting through many classes wondering where in the world would I ever use this stuff. Well, I found out. They are excellent teachers whose excitement and enthusiasm for science has definitely shaped many students lives.

As for this thesis itself, Yi-Bin Cao, Ben Chew, Alan Frankel, Matt Johnson and Ching-Hwa Kiang contributed greatly to the protonated water cluster/chlorine nitrate experiment. Being there for the early days of the Okumura group, they had the privilege of building and getting running the time-of-flight mass spectrometer.

Chapters Two and Three would not have been possible without the help of Tim Minton and Teresa Moore. Tim graciously opened his laboratory at the Jet Propulsion Laboratory and allowed us to use the Crossed Molecular Beams Apparatus. His expertise and assistance on the instrument definitely made the project run much more smoothly. Tim and Teresa also helped set up the experiment and spent many long nights collecting data. Jessie Haldeman deserves a word of thanks for synthesizing the ClONO2 used in the experiment.

The supporting staff at Caltech merits a round of applause. Guy, Tony and Ray in the machine shop always patiently answered many mechanical questions and on occasion gave my projects special priority, even when I didn't particularly deserve it. Tom Dunn also deserves special mention. He solved endless electronic nightmares and stopped by on an occasional Friday evening to see if there were any last minute questions regarding the resuscitation of the quadrupole mass spectrometer. Dian Buchness always watched out for us graduate students making sure that our forms and papers were always in order to ensure that the paycheck would arrive on time.

Also, thanks to everyone with whom I shared the laboratory over the past few years -- Yi-Bin Cao, Ben Chew, Jong-Ho Choi, Alan Frankel, Bermi Haas, Matt Johnson, Keith Kuwata, Teresa Moore, Jim Spotts, and Leon Waxer. You guys always provided interesting dialogue, helped out and answered questions even when you were too busy with your own work. Matt and Jim deserve an added acknowledgment for graciously reading and editing my proposals.

When I look back on Caltech however my most special memories do not center around my work but rather the good friends that I made there. I don't know whether it is because similar personalities are drawn to graduate school or whether adversity binds people together. Jen Blank, Teri Longin, Barbara Wyslouzil, Jamie Schlessman, Dian Buchness, and Jeremy Semrau were always there to pick me up when I most needed it. Early morning jogs with Jen which many times turned out to be more talking than jogging helped keep my body and mind in shape. Jen also introduced me to the expensive habit of enjoying a nice glass of port after dinner. Teri was always willing to go out for a Friday night beer after which many times we would find ourselves at the half-price sushi bar. She also taught me the finer things to bring on a backpacking trip. A rainstorm in the desert doesn't seem so dreary with a bottle of Kamikazes on hand. Barbara played hooky with me in Santa Barbara when things would get too stressful in Pasadena and if there wasn't enough time for that a Bloody Mary lunch at Bullocks would pull us through. The world restaurant tour of Los Angeles with Jeremy gave me an excuse to explore the city and led to many late night discussions that emptied out my liquor cabinet. Jamie was always willing to lend a hand and deserves special mention for helping with the paper work of submitting this thesis. I also want to acknowledge the Caltech Women's and Chemistry Soccer Teams for always giving me something to do on Sunday afternoons.

Last but not least, I would like to thank my parents for their support and encouragement throughout my entire education.

Abstract

Chlorine oxide species have received considerable attention in recent years due to their central role in the balance of stratospheric ozone. Many questions pertaining to the behavior of such species still remain unanswered and plague the ability of researchers to develop accurate chemical models of the stratosphere. Presented in this thesis are three experiments that study various properties of some specific chlorine oxide species.

In the first chapter, the reaction between $ClONO_2$ and protonated water clusters is investigated to elucidate a possible reaction mechanism for the heterogeneous reaction of chlorine nitrate on ice. The ionic products were various forms of protonated nitric acid, $NO_2^+(H_2O)_m$, $m = 0, 1, 2$. These products are analogous to products previously reported in the literature for the neutral reaction occurring on ice surfaces. Our results support the hypothesis that the heterogeneous reaction is acid-catalyzed.

In the second chapter, the photochemistry of $ClONO_2$ was investigated at two wavelengths, 193 and 248 nm, using the technique of photofragmentation translational spectroscopy. At both wavelengths, the predominant dissociation pathways were Cl + NO_3 and ClO + NO_2. Channel assignments were confirmed by momentum matching the counterfragments from each channel. A one-dimensional stratospheric model using the new 248 nm branching ratio determined how our results would affect the predicted Cl_x and NO_x partitioning in the stratosphere.

Chapter three explores the photodissociation dynamics of Cl_2O at 193, 248 and 308 nm. At 193 nm, we found evidence for the concerted reaction channel, Cl_2 + O. The ClO + Cl channel was also accessed, however, the majority of the ClO fragments were formed with sufficient internal energies for spontaneous secondary dissociation to occur. At 248 and 308 nm, we only observed only the ClO + Cl channel. Some of the ClO formed at 248 nm was formed internally hot and spontaneously dissociated. Bimodal

translational energy distributions of the ClO and Cl products indicate two pathways leading to the same product exist.

Appendix A, B and C discuss the details of data analysis techniques used in Chapters 1 and 2. The development of a molecular beam source of ClO dimer is presented in Appendix D.

TABLE OF CONTENTS

Chapter 4: ClOOCl Molecular Beam Source

Appendix A

Appendix B

Appendix C

INTRODUCTION

Awareness of decreasing ozone concentrations over Antarctica started in 1985 with a paper published by Joseph Farman and his coworkers at the British Antarctic Survey. This paper presented the long term measurements of total column ozone over Halley Bay taken using ground-based spectrophotometers.[1] With records dating back to 1957, Farman *et al.* documented that since 1968 spring values for the total column ozone over Antarctica have consistently decreased each year. The daily value for mean total ozone in October prior to 1968 was greater than 300 Dobson units (DU), however, by 1984 the value had fallen to less than 200 DU. The total value over Antarctica in October 1991 was less than 150 DU.[2] Measurements recorded in Dobson units (DU), or milliatmosphere-centimeters, reflect the total amount of ozone in a vertical column extending upwards from the instrument. Multiplying a measurement recorded in DU by the number of air molecules in 1 cubic centimeter at standard temperature and pressure gives the total number of ozone molecules in a cross-sectional area of 1 cm^2 rising from the surface of the Earth. Nearly all of the ozone in the lower stratosphere (14 to 22 km) over Antarctica is destroyed during the six week period beginning with the first rays of sunlight in mid-August though the first week of October. Current austral spring losses represent the destruction of approximately 3% of the total stratospheric ozone.[3-6]

Comprehensive coverage of the Total Ozone Mapping Spectrometer (TOMS) on the Nimbus-7 satellite confirmed Farman's ground-based observations.[7] The TOMS measurements also illustrated the geographic extent of the ozone loss and showing it to reach from the south pole to about 60°S latitude, covering the entire continent of Antarctica or approximately one fifteenth of the entire surface area of the Earth.

Farman *et al.* suggested that reactions involving chlorine in a catalytic cycle were responsible for the observed phenomena and that these reactions were primed by the very low temperatures of the Antarctic winter producing a stratospheric environment uniquely

sensitive to ozone destruction. The idea of chlorine catalytically destroying stratospheric ozone was not new. Molina and Rowland had published a paper in 1974 discussing removal mechanisms for inert chlorofluorocarbons in the atmosphere.[8] They theorized that the chemical inertness of these species and their insolubility in water prevented their removal via classic tropospheric sinks, such as reaction with OH radicals and rainout. The primary sink for these inert species was hypothesized to be diffusion into the stratosphere where they could be degraded photolytically by ultraviolet solar radiation. Molina and Rowland predicted this would result in the release of significant amounts of chlorine atoms which could lead to the catalytic destruction of ozone;

$$Cl + O_3 \longrightarrow ClO + O_2$$

$$ClO + O \longrightarrow Cl + O_2.$$

Additional measurements made at Halley Bay indicated (in agreement with measurements made worldwide) that indeed the atmospheric concentrations of the chlorofluorocarbon species Freon 11 ($CFCl_3$) and Freon 12 (CF_2Cl_2) had increased by a factor of 3 during the years during the 1970's suggesting a link between CFCs and stratospheric ozone depletion.

Although Farman's postulate was generally accepted, other proposals were put forth to explain the phenomena. For instance, dynamical theories held that vertical advection driven by solar heating was responsible.[9] Detailed calculations of dynamical processes attempted to show that vertical motion caused ozone-poor air from the upper troposphere to displace the ozone layer either vertically or horizontally. Another theory postulated by Callis *et al.*[10] held that solar proton events could increase the production rate of nitrogen oxides in the polar region driving an alternative ozone depleting catalytic cycle involving NO and NO_3.

A critical experiment performed by J. Anderson *et al.* definitively tied the dramatic ozone losses over Antarctica to increased chlorine concentrations.[11] Using a medium-

range, high-altitude ER-2 reconnaissance aircraft, they simultaneously measured O_3 and ClO concentrations in the polar air mass and showed that regions with significant decreases in ozone coincided with regions of unusually high ClO concentrations. This confirmed that the "ozone hole" was man-made since more than 80% of the current chlorine loading of the stratosphere comes from anthropogenic sources such as chlorofluorocarbons.

Initially atmospheric models could not account for the observed losses in the southern polar region. These models predicted that the chlorine radicals would react with nitrates or methane in the stratosphere and form relatively inert reservoir species, $ClONO_2$ and HCl. A factor they had ignored in these calculations was the possibility of heterogeneous reactions. During the winter months, a vortex forms over Antarctica which isolates the polar air mass and results in temperatures cold enough (< 195 K) for polar stratospheric clouds (PSCs), composed of water and nitric acid, to form. On the surface of these clouds, reactions occur which convert the stable chlorine reservoir species into more reactive forms, HOCl and Cl_2.[12]

$$ClONO_{2\,(g)} + H_2O_{\,(s)} \longrightarrow HOCl_{\,(g)} + HNO_{3\,(ice)}$$

$$ClONO_{2\,(g)} + HCl_{\,(ice)} \longrightarrow Cl_{2\,(g)} + HNO_{3\,(ice)}$$

These reactions accomplish two tasks. First, they convert chlorine into species that when photolyzed release atomic chlorine; this chlorine, in turn, catalytically destroys ozone through the following mechanism:

$$2 \times (Cl + O_3 \longrightarrow ClO + O_2)$$

$$ClO + ClO \longrightarrow ClOOCl$$

$$ClOOCl + h\nu \longrightarrow Cl + ClOO$$

$$ClOO \longrightarrow Cl + O_2$$

Net: $2O_3 \longrightarrow 3O_2$.

This mechanism accounts for approximately 70% of the ozone loss in the polar regions.[13] The majority of the remaining depletion occurs via a bromine mechanism:[14]

$$Cl + O_3 \longrightarrow ClO + O_2$$

$$Br + O_3 \longrightarrow BrO + O_2$$

$$ClO + BrO \longrightarrow Cl + Br + O_2$$

$$\text{Net:} \quad 2O_3 \longrightarrow 3O_2.$$

The revisions of the mechanism originally proposed by Molina and Rowland reflects the realization that O atoms could not be involved quantitatively in O_3 destruction because concentrations of O atoms in the polar stratosphere are too low.

The heterogeneous reactions' second task is to denitrify the stratosphere by sequestering nitrate groups in the PSCs. The removal of the gas-phase nitrates prevents the back reactions that form $ClONO_2$ ($ClO + NO_2 \rightarrow ClONO_2$) and leaves the active chlorine unencumbered to participate in the ozone degrading cycles. Outside of the polar vortex, however, temperatures are high enough that PSCs do not form, and thus the nitrate groups remain free to react with active chlorine species to form reservoir species.

As for Arctic regions, data recorded by the Microwave Limb Sounder (MLS) on the Upper Atmosphere Research Satellite (UARS) reveal that the conditions ideal for ozone degradation can also form in the Northern hemisphere.[2] These data confirm that an Arctic polar vortex forms and that the extremely cold temperatures at which Polar Stratospheric Cloud (PSC) aerosols condense (<195 K) are achieved. This year, a warming trend at the end of January before the advent of spring prevented any large losses of ozone. However, an unusually cold winter could maintain the conditions until after solar illumination which would result in a major depletion of ozone in the Northern hemisphere.

Outside of the polar regions, a downward trend in lower stratospheric ozone of 10% per decade has been observed at all latitudes except the tropics.[15] In 1992, total

global ozone at mid-latitudes in the northern hemisphere (between 30° and 60°N where most Americans, Canadians and Europeans live) ozone levels were 9% below normal, and at 60°N (the latitude of Anchorage and southern Scandinavia) ozone levels were down 14%. These measurements are 2-3% lower than any earlier year and 1.5 percent lower than model predictions.[16] Such a dramatic loss of ozone over such a short time demonstrates that global-scale atmospheric changes can occur in very short time periods.

Model predictions in 1992 underestimated the amount of ozone loss at both polar and mid-latitudes.[16] Current explanations for the discrepancies between the models and 1992 measurements center around the impact of Mount Pinatubo's eruption in 1991 which spewed volcanic debris into the stratosphere. Questions surround whether volcanic aerosols, composed mainly of liquid sulfuric-acid, can catalyze reactions similar to those observed on PSCs. If so, this could increase ozone loss rates at both the polar caps and mid-latitudes.[17] Other explanations involve the idea that aerosol particles absorb solar radiation which results in perturbations of the wind patterns which in turn affect ozone transport. Aerosols might also cause changes in the photochemical production or loss rate of ozone by changing the stratospheric temperature. The inability of models to accurately predict and explain observed concentrations highlights the need to continually update and improve these models. Improvements are needed in our understanding of both the overall chemistry of the system and the dynamical forces involved in the atmosphere.

In this thesis, a series of experiments addressing uncertainties in reaction parameters used in the chemical models are presented. The first chapter presents an experiment investigating reactions between $ClONO_2$ and protonated water clusters. The impetus of the study is to elucidate a possible reaction mechanism for the ice catalyzed reaction, $ClONO_2 + H_2O$. By understanding the role the ice surface plays in the reaction mechanism, we improve our ability to predict whether other aerosols present in the stratosphere can catalyze similar reactions.

In the second chapter, the photochemistry of $ClONO_2$ is investigated at two wavelengths - 193 and 248 nm. We discovered that previous photolysis experiments failed to identify a major photolytic channel at both wavelengths which implies that the branching ratios for other chlorine oxide species may also be wrong.

Chapter Three explores the photodissociation dynamics of Cl_2O at 193, 248 and 308 nm. Although Cl_2O is not a major species in the stratosphere, this study does provide us with a greater understanding of the photolytic behavior of chlorine oxides.

Chapter Four discusses the development of a molecular beam of ClO dimer. The ultimate goal of this project is to use this source to study the photodissociation dynamics of ClOOCl in a collisionless environment. ClOOCl photolysis plays a pivotal role in current models of the stratosphere. Many questions still surround the accuracy of reported branching ratios and how excess energy is partitioned in the product fragments.

Improving our understanding of the chemical reactions and mechanisms important in the stratosphere will provide us with a foundation from which to develop better simulations of our global environment, allowing us to predict more accurately future trends and to create possible solutions to current concerns.

REFERENCES

1. J.C. Farman, B.G. Gardiner, J.D. Shanklin, *Nature* **315**, 207 (1985).

2. J.W. Waters, L. Froidevaux, W.G. Read, G.L. Manney, L.S. Elson, D.A. Flower, R.F. Jarnot, R.S. Harwood, *Nature* **362**, 597 (1993).

3. D.J. Hofmann, J.W. Harder, J.M. Rosen, J.V. Hereford, J.R. Carpenter, *J. Geophys. Res.* **94**, 16527 (1989).

4. T. Deshler, D.J. Hofmann, J.V. Hereford, C.B. Sutter, *Geophys. Res. Lett.* **17**, 151 (1990).

5. B.G. Gardiner, *Geophys. Res. Lett.* **15**, 901 (1988).

6. W.D. Komhyr, R.D. Grass, R.K. Leonard, *J. Geophys. Res.* **94**, 11429 (1988).

7. R.S. Stolarski, A.J. Krueger, M.R. Schoeberl, R.D. McPeters, *Nature* **322**, 808 (1986).

8. M.J. Molina, F.S. Rowland, *Nature* **249**, 810 (1974).

9. K.K. Tung, *Geophys. Res. Lett.* **13**, 13 (1986).

10. L.C.Callis and M. Natarajan, *J. Geophys. Res.* **91**, 771 (1986).

11. J.G. Anderson, D.W. Toohey, W.H. Brune, *Science* **251**, 39 (1991).

12. S. Solomon, R.R. Garcia, F.S. Rowland, D.J. Wuebbles, *Nature* **321**, 755 (1986).

13. L.T. Molina and M.J. Molina, *J. Phys. Chem.* **91**, 433 (1987).

14. M.B. McElroy, R.J. Salawitch, S.C. Wofsy, J.A. Logan, *Nature* **321**, 759 (1986).

15. R.S. Stolarski, R. Bojkov, L. Bishop, C. Zerefos, J. Staehelin, J. Zawodny, *Science* **256**, 342 (1992).

16. J.F. Gleason, P.K. Bhartia, J.R. Herman, R. McPeters, P. Newman, R.S. Stolarski, L. Flynn, G. Labow, D. Larko, C. Seftor, C. Wellemeyer, W.D. Komhyr, A.J. Miller, W. Planet, *Science* **260**, 523 (1993).

17. D.J. Hofmann, S. Solomon, *J. Geophys. Res.* **94**, 5029 (1989).

Chapter 1:

Reaction of Chlorine Nitrate with Protonated Water Clusters: A Model for Heterogeneous Reactions on Polar Stratospheric Clouds

ABSTRACT

The reactions of small protonated water clusters , $H_3O^+(H_2O)_n$, with chlorine nitrate, $ClONO_2$, were investigated to elucidate the molecular mechanism for the heterogeneous reaction of chlorine nitrate with ice. The ionic reaction products were various forms of protonated nitric acid, $NO_2^+(H_2O)_m$, $m = 0, 1, 2$. These products are analogous to products previously reported in the literature for the neutral reaction occurring on ice surfaces. Our results support the hypothesis that the heterogeneous reaction is acid-catalyzed.

I. INTRODUCTION

Heterogeneous reactions occurring on polar stratospheric cloud particles (PSCs) play a central role in the depeletion of stratospheric ozone which has been observed over Antarctica during the austral spring.[1,2] The PSCs form during the polar winter, when temperatures in the strosphere drop below 195 K. Reactions on the surface of the cloud particles, which include

$$ClONO_2 + H_2O(s) \longrightarrow HOCl(g) + HNO_3(ad) \quad (1)$$

$$ClONO_2 + HCl(ad) \longrightarrow Cl_2(g) + HNO_3(ad) \quad (2)$$

$$HOCl + HCl(ad) \longrightarrow Cl_2(g) + H_2O(s) \quad (3)$$

convert the stable chlorine reservoirs, chlorine nitrate ($ClONO_2$) and hydrogen chloride (HCl), into more photosensitive species Cl_2 and HOCl.[3] These reactions are extremely slow in the gas phase.[4-6] Photolysis of Cl_2 and HOCl in the spring generates chlorine radicals which destroy ozone through catalytic cycles involving ClO.[2,7-9] Because the heterogeneous reactions leave nitric acid sequestered in the PSCs, they enhance the chlorine radical concentration by removing NO_x from the gas phase, thus preventing recombination of ClO and NO_2 to form $ClONO_2$.

Laboratory experiments using flow tubes and Knudsen cell flow reactors have demonstrated that ice and nitric acid hydrate surfaces catalyze the reactions of $ClONO_2$ with water and HCl. The studies determined final products, sticking coefficients, and reaction probabilities of these heterogeneous reactions.[10-14] Though much effort has been put into understanding the kinetics, the reaction mechanism at the molecular level remains unclear. How does an ice surface act as a catalyst? Molina *et al.* have proposed an acid-catalysis mechanism,[15] in which the chlorine nitrate reacts with a proton and forms a Cl^+ leaving group

$$ClONO_2 + H^+ \longrightarrow HNO_3{-}Cl^+. \quad (4)$$

Another possible mechanism is the lowering of the activation barrier when water molecules solvate the chlorine nitrate which could lead to facile heterolytic or homolytic bond cleavage. The role of solvation and the relative contributions of ionic versus neutral reaction paths are key issues that remain unresolved for these and other heterogeneous reactions occurring in the atmosphere.

We have undertaken a study of the reactions of chlorine nitrate with hydrated cluster ions to explore the mechanism of these reactions on ice. Unlike catalysis on metal surfaces, reactions on the surface of molecular solids are more likely to be localized processes; thus, a small cluster of water molecules may mimic the catalytic properties of an ice surface. Although the detailed structure differs, the energetics of hydrogen bonding in clusters are comparable to the bulk. Thus, studies of the reactions of $ClONO_2$ with water clusters could elucidate the mechanism of the heterogeneous reaction on type II PSCs (ice) in the stratosphere. Here, we report initial results on a study of the reaction

$$ClONO_2 + H_3O^+(H_2O)_n \longrightarrow \text{products} \qquad (5)$$

where $\langle n \rangle \approx 14$. The ionic products are mass analyzed and detected, allowing us to probe the reaction mechanisms without the fragmentation induced by electron impact ionization.

A number of investigators have studied the reactions of hydrated ion clusters that are relevant in the atmosphere. Yang, Castleman, and coworkers investigated the nucleation and reactions of protonated water clusters in a flow tube to determine their importance in noctilucent clouds.[16] In similar flow tube experiments, Bohringer *et al.* studied the catalysis by a solvated inert ion of the reaction of N_2O_5 with water to form HNO_3.[17] They did not extrapolate their results to the bulk phase but expected that for larger clusters ($n > 7$), the reaction would be catalyzed by the same mechanism as on surfaces. None of these studies has attempted to use cluster reactions to model the chemistry of the condensed phase.

II. EXPERIMENT

A schematic of the source and reaction cell is shown in Figure 1. Cluster ions were formed in the expansion of a pulsed glow discharge. The skimmed beam was introduced into a reaction cell containing chlorine nitrate, and the product ions were then mass analyzed.

We saturated helium or argon ($p \approx 2$ atm) with water vapor by passing it through room temperature wet molecular sieves. Next the saturated gas was expanded through the 0.5-mm orifice of a piezo-driven pulsed valve and was ionized with a dc glow discharge (-600 V, ≈5-10-mA peak current) in a 3-mm-diameter channel. The resulting plasma was expanded through a 10°, 3-cm-length expansion cone. After collimation by a skimmer (4-mm aperture) positioned 8.5 cm downstream from the end of the expansion cone, the beam entered the reaction flow cell. The cell had an effective length (including skimmer) of 8 cm. The chlorine nitrate was introduced through a Teflon sleeve with four 0.6-mm injection ports. The pressure of chlorine nitrate in the cell was varied from zero to 10 mtorr. After passing through the reaction cell, the ions drifted 7 cm into the extraction region of a reflectron time-of-flight mass spectrometer.

The chlorine nitrate was synthesized from the reaction of Cl_2O and N_2O_5 and then distilled, using procedures described in the literature.[18] The sample, a clear yellow liquid, was kept at -60°C during the experiment, and the vapor was bled into the reaction cell through a Teflon line. The line pressure, measured with a capacitance manometer, was typically 1 torr. At these temperatures, the vapor pressure of any nitric acid impurity was less than 1 mtorr.

III. RESULTS

Figure 2a shows a typical distribution of protonated water clusters in the absence of chlorine nitrate. The distribution was centered around $n = 14$, and no monomers, dimers or trimers were present (see Figure 3a).

Collisional Dissociation. As we increased the pressure of the chlorine nitrate (see Figure 2b,c), the cluster distribution shifted to smaller cluster sizes. We attribute this result to collision-induced dissociation of larger water clusters when they collided with chlorine nitrate.

The collision energy was determined from the beam velocity, which was approximately the terminal velocity of a supersonic expansion of helium ($\langle v_{beam} \rangle \approx 1.5 \times 10^5$ cm/s). The chlorine nitrate velocity was negligible in comparison to the beam velocity ($\langle v_{ClONO_2} \rangle \approx 0$ cm/s). The chlorine nitrate could be entrained or "picked up" into the beam through multiple collisions with the helium atoms. If the chlorine nitrate were not completely entrained before collision with a water cluster, the hyperthermal collisions could lead to dissociation of the larger water clusters. An upper limit on the collision energy in the center of mass frame, as a function of the number n of water molecules in the cluster is given by the relation $T = 26.3((18n + 19)/(18n + 116))$ kcal/mol.[19] The collisional energy would be less if the chlorine nitrate was first partially or completely entrained into the jet.

We estimated the maximum number of H_2O molecules lost per collision under these conditions. The maximum collision energy of a water 10-mer with a chlorine nitrate molecule under our conditions was approximately 17 kcal/mol, and that of a 20-mer, 21 kcal/mol. The hydrogen bond energies of water molecules to the hydronium ion decreases as the number of water molecules in the cluster increases.[20] In clusters containing more than eight water molecules, the binding energy approaches 12 kcal/mol, the heat of

sublimation of ice.[12] Therefore, when a 20-mer collides with a chlorine nitrate molecule, the maximum number of water molecules that can evaporate is one.

The number of collisions, and hence the degree of fragmentation, depends on the $ClONO_2$ pressure. Assuming a cross section of 5×10^{-15} cm^2, Figure 2b corresponds to five collisions; Figure 2c, to ten collisions. The shift in the water cluster distribution confirmed these numbers. No monomers were present because the collisions were not energetic enough to overcome the 31.6 kcal/mol binding energy of $H_3O^+(H_2O)$.

Cluster Reactions. In addition to the shift of the cluster distribution, a new series of peaks appeared with masses at 46, 64 and 82, as seen in Figure 3. These peaks correspond to the products NO_2^+, $NO_2^+(H_2O)$ and $NO_2^+(H_2O)_2$, demonstrating that the chlorine nitrate reacts with protonated water clusters. The observed products indicate that the reaction proceed via the lowest energy channels

$$ClONO_2 + H_3O^+ \longrightarrow HOCl + H_2NO_3^+ \qquad \Delta H_{298} = 0 \text{ kcal/mol} \quad (6)$$

$$\longrightarrow HOCl + H_2O + NO_2^+ \qquad \Delta H_{298} = 10 \text{ kcal/mol} \quad (7)$$

Recent configuration interaction calculations suggest that the proton affinity of nitric acid may be higher than previously reported by as much as 14 kcal/mol,[22] in which case, reaction 6 becomes exothermic.

NO_2^+ was the primary product, although reaction 7 is 10 kcal/mol higher in energy than reaction 6. This is probably due to a barrier for the transfer and reorganization of solvent molecules. Collisional energies that exceed the endothermicity of the dehydration of $H_2NO_3^+$ also contribute to this result.

We did not observe any other product peaks, e.g., $H_3O^+(H_2O)_nClO$ or $H_3O^+(H_2O)_nClONO_2$, which correspond to other reaction channels or ligand association. In contrast, we found methanol was readily picked up by protonated water clusters using similar conditions to form a new series, $H_3O^+(H_2O)_nCH_3OH$. These results are consistent with the low sticking probability of $ClONO_2$ on ice surfaces observed in bulk experiments.

Peaks labeled with an asterisk in Figure 3b were fragment ions produced from the dissociation of larger, vibrationally excited metastable clusters in the field-free flight path of the mass spectrometer. The fragment ions were formed with different energies than the parent ions, and the two sets of ions were distinguished by using the reflectron, a retarding electric field which was used as an energy analyzer. By varying the potential on the reflectron, we shifted the arrival times of the metastable peaks with respect to those of the parent ions.

When a cluster ion collides with a chlorine nitrate molecule, two possible channels can occur, collision-induced dissociation (CID) and reaction to form the NO_2^+ products species:

$$ClONO_2 + H_3O^+(H_2O)_n \longrightarrow ClONO_2 + m(H_2O) + H_3O^+(H_2O)_{n-m}$$
$$\longrightarrow HOCl + (H_2O)_{n-m} + NO_2^+(H_2O)_m$$

Armentrout and colleagues have shown that, for reactions involving cluster ions, dissociation occurs at higher collisional energies (> 0.5 eV), while ion-molecule reactions have larger relative cross sections at lower energies.[23]

To better quantify the relative contributions from dissociation versus reaction, we investigated the relative appearance rates for the various products. We plotted the integrated peak intensities (normalized to the total ion count) as a function of the pressure of chlorine nitrate in the reaction region (Figure 4). Because these are essentially beam scattering experiments with multiple collisions, the appearance or disappearance of ions was fit using a kinetic model based on a cascading reaction, A→B→C. Two competitive pathways account for the size dependent behavior in the water clusters: loss of water clusters due to reaction or collision-induced dissociation and gain from the formation of smaller clusters as the larger water clusters dissociate. The position of the water cluster in the cluster distribution determined which pathway was dominant. As for the appearance

rate for reaction products, the three $NO_2^+(H_2O)_m$ peaks were comparable to each other and approximately on third the appearance rate of $H_3O^+(H_2O)_2$.

IV. DISCUSSION

These experiments provide the first direct evidence of an ionic mechanism for the reaction of chlorine nitrate with water. The products that we observed for the reaction of chlorine nitrate with protonated water clusters are analogous to those observed for neutral reactions on ice surfaces (reaction 1). The mass 64 product $H_2NO_3^+$ is protonated nitric acid which when formed in gas-phase reactions, fragments readily to NO_2^+ and H_2O.[24] Although we could not observe the neutral products directly, HOCl is the most likely product because other channels are significantly more endothermic. These reactions conserve the excess proton, which may serve as a catalyst. A plausible mechanism is that the proton directly attacks the chlorine nitrate at the center oxygen

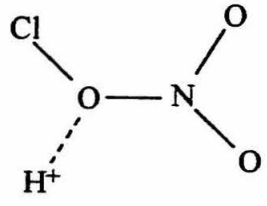

to form HOCl followed by charge transfer to NO_2 (IP = 9.75 eV) as occurs in the protonation of nitric acid, $HNO_3 + H^+ \rightarrow NO_2^+(H_2O)$.[22,24]

The high yields for collisional dissociation indicate that the collision energies are high, therefore, this experiment does not duplicate stratospheric conditions. To arrive at quantitative measurements of relevance to stratospheric ozone degradation, experiments to study these reactions at thermal energies are being developed.

Our results demonstrate that $ClONO_2$ will react with small water aggregates if a proton is present and support the general hypothesis of Molina *et al.* predicting acid-catalysis. This mechanism may well be operable on the surfaces of PSCs. Our

observation of NO_2^+ instead of Cl^+ provides evidence that Molina's reaction scheme is incorrect. This result is anticipated on thermodynamic grounds, since solvation leading to NO_3^- and Cl^+ provides evidence that Molina's reaction scheme is incorrect. This result is anticipated on thermodynamic grounds, since solvation leading to NO_3^- and Cl^+ is unfavorable due to the high ionization potential of Cl (12.97 eV). Other reaction channels are also improbable because they are highly endothermic

$$ClONO_2 + H_3O^+ \longrightarrow HOCl^+ + H_2O + NO_2 \qquad \Delta H_{298} = 41 \text{ kcal/mol} \quad (8)$$

$$\longrightarrow HNO_3^+ + Cl + H_2O \qquad \Delta H_{298} = 68 \text{ kcal/mol} \quad (9)$$

$$\longrightarrow Cl^+ + HNO_3 \qquad \Delta H_{298} = 91 \text{ kcal/mol.} \quad (10)$$

Previous experiments investigating reactions of chlorine nitrate on surfaces using concentrated acidic solutions found the reaction probabilities to be lower than on neutral pH ice surfaces.[11,13] These results appear to negate the acid-catalysis hypothesis; however, high concentrations of anions may inhibit the reaction if ion-ion interactions suppress proton transfer to an adsorbate. Similar experiments using weak acidic surfaces doped with HCl found the reaction probabilities to be higher than those on neat ice surfaces,[10,25] indicating that proton reactions may be more facile when the counteranion is sufficiently screened. Recent results in the literature suggest that on HCl-doped ice surfaces $ClONO_2$ initially reacts with water followed by a rapid secondary reaction of HOCl with HCl on the surface to produce the observed Cl_2.[26,27] Acid catalysis of reaction 1 could explain the increased reaction probabilities for $ClONO_2$ on HCl-doped surfaces observed by Tolbert *et al.*,[12] Leu *et al.*,[10,14] and Molina *et al.*,[25] and is consistent with the liquid surface layer proposed by Abbatt *et al.*.[28] To test the catalytic effect of the proton, we plan to study the reactions of hydrated sodium ions, $Na^+(H_2O)_n$.

V. REFERENCES

1. J.C. Farman, B.G. Gardiner, J.D. Shankin, *Nature* **315**, 207 (1985).
2. J.G. Anderson, D.W. Toohey, W.H. Brune, *Science* **251**, 39 (1991).
3. S. Solomon, R.R. Garcia, F.S. Rowland, D.J. Wuebbles, *Nature* **321**, 755 (1986).
4. R. Atkinson, E.C. Tuazon, H. MacLeod, S.M. Aschmann, A.M. Winer, *Geophys. Res. Lett.* **13**, 117 (1986).
5. R. Atkinson, S.M. Aschmann, E.C. Tuazon, M.A. Goodman, A.M. Winer, *J. Atmos. Chem.* **5**, 83 (1987).
6. L.T. Molina, M.J. Molina, R.A. Stachnik, R.D. Tom, *J. Phys. Chem.* **89**, 3779 (1985).
7. L.T. Molina, M.J. Molina, *J. Phys. Chem.* **91**, 433 (1987).
8. S. Solomon, *Rev. Geophys.* **26**, 131 (1988).
9. M.B. McElroy, R.J. Salawitch, *Science* **243**, 763 (1989).
10. M.T. Leu, *Geophys. Res. Lett.* **15**, 17 (1988).
11. M.A. Tolbert, M.J. Rossi, D.M. Golden, *Geophys. Res. Lett.* **15**, 847 (1988).
12. M.A. Tolbert, M.J. Rossi, R. Malhotra, D.M. Golden, *Science* **238**, 1258 (1987).
13. M.J. Rossi, R. Malhotra, D.M. Golden, *Geophys. Res. Lett.* **14**, 127 (1988).
14. M.T. Leu, S.B. Moore, L.F. Keyser, *J. Phys. Chem.* **95**, 7763 (1991).
15. S.C. Wofsy, M.J. Molina, R.J. Salawitch, L.E. Fox, M.B. McElroy, *J. Geophys. Res.* **93**, 2442 (1988).
16. X. Yang, X. Zhang, A.W. Castleman, Jr., *Int. J. Mass Spectrom. Ion. Processes* **109**, 39 (1991). X. Yang, A.W. Castleman, Jr., *J. Geophys. Res.* **96**, 2573 (1991).
17. H. Bohringer, D.W. Fahey, F.C. Fehsenfeld, E.E. Ferguson, *Planet. Space Sci.* **31**, 185 (1983).
18. M. Schmeisser, *Inorg. Synth.* **9**, 127 (1967).
19. R.D. Levine, R.B. Bernstein, *Molecular Reaction Dynamics and Chemical Reactivity*; Oxford Press: New York, 1987; pp. 37-38.

$$T = \frac{1}{2}\frac{m_1 m_2}{m_1 + m_2}(v_1 - v_2)^2$$

20. Y.K. Lau, S. Ikuta, P. Kebarle, *J. Am. Chem. Soc.* **104**, 1462 (1982).

21. *CRC Handbook of Chemistry and Physics*; D.R. Lide, Ed.; CRC Press: Boston, 1990; pp. 6-11.

22. T.J. Lee, J.E. Rice, *J. Phys. Chem.* **96**, 650 (1992).

23. R.H. Schultz, P.B. Armentrout, *Int. J. Mass Spectrom. Ion. Processes* **107**, 29 (1991).

24. F. Cacace, M. Attina, G. de Petris, M. Speranza, *J. Am. Chem. Soc.* **112**, 1014 (1990).

25. M.J. Molina, T.L. Tso, L.T. Molina, F.C. Wang, *Science* **238**, 1253 (1987).

26. J.P.D. Abbatt, M.J. Molina, *Geophys. Res. Lett.* **19**, 461 (1992).

27. M.J. Prather, *Nature* **355**, 534 (1992).

28. J.P.D. Abbatt, K.D. Beyer, A.F. Fucaloro, J.R. McMahon, P.J. Woolridge, R. Zhang, M.J. Molina, *J. Geophys. Res.* **97**, 15819 (1992).

VI. FIGURE CAPTIONS

Figure 1. Schematic of the source region showing the expansion and reaction flow regions.

Figure 2. Mass spectra of water cluster distributions for various pressures of $ClONO_2$ in the reaction flow region. a) P_{ClONO_2} = 0.0 mtorr; b) P_{ClONO_2} = 3.4 mtorr; c) P_{ClONO_2} = 7.4 mtorr.

Figure 3. An enlargement (15x) of the mass spectra in Figure 2 for the masses 0-90 amu. Masses 46, 64 and 82 coresspond to the $NO_2^+(H_2O)_n$ series. The peaks labelled with asterisks (*) correspond to metastable ions. a)P_{ClONO_2} = 0.0 mtorr; b) P_{ClONO_2} = 3.4 mtorr; c) P_{ClONO_2} = 7.4 mtorr.

Figure 4. The integrated peak intensities (normalized to the total ion count) plotted as a function of $ClONO_2$ pressure in the reaction region. The data was fit using a kinetic model based on a cascading reaction, $A \rightarrow B \rightarrow C$.

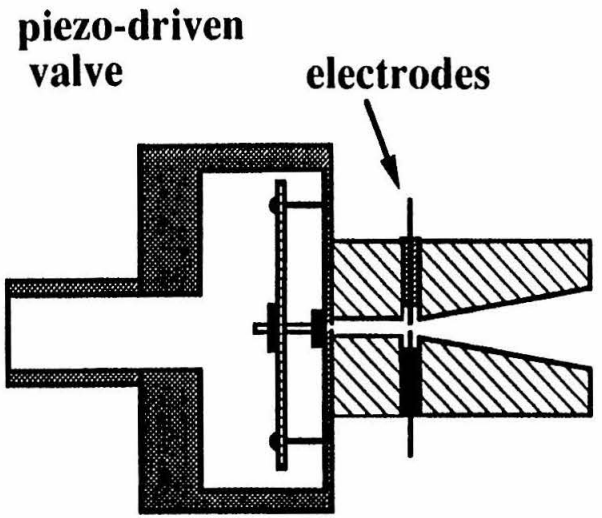
piezo-driven
valve
electrodes

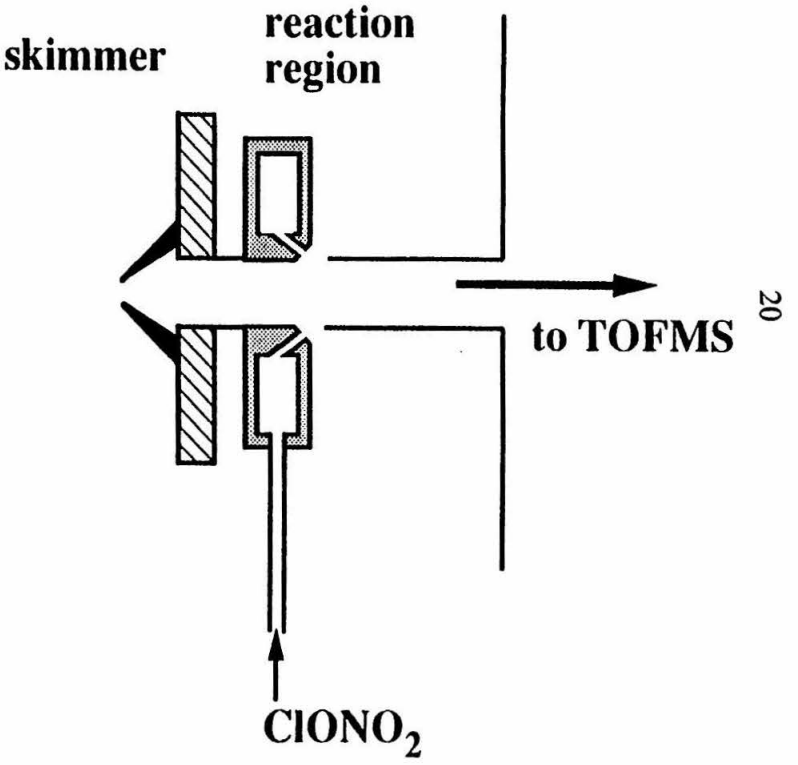
skimmer
reaction
region
to TOFMS
ClONO2

Figure 1

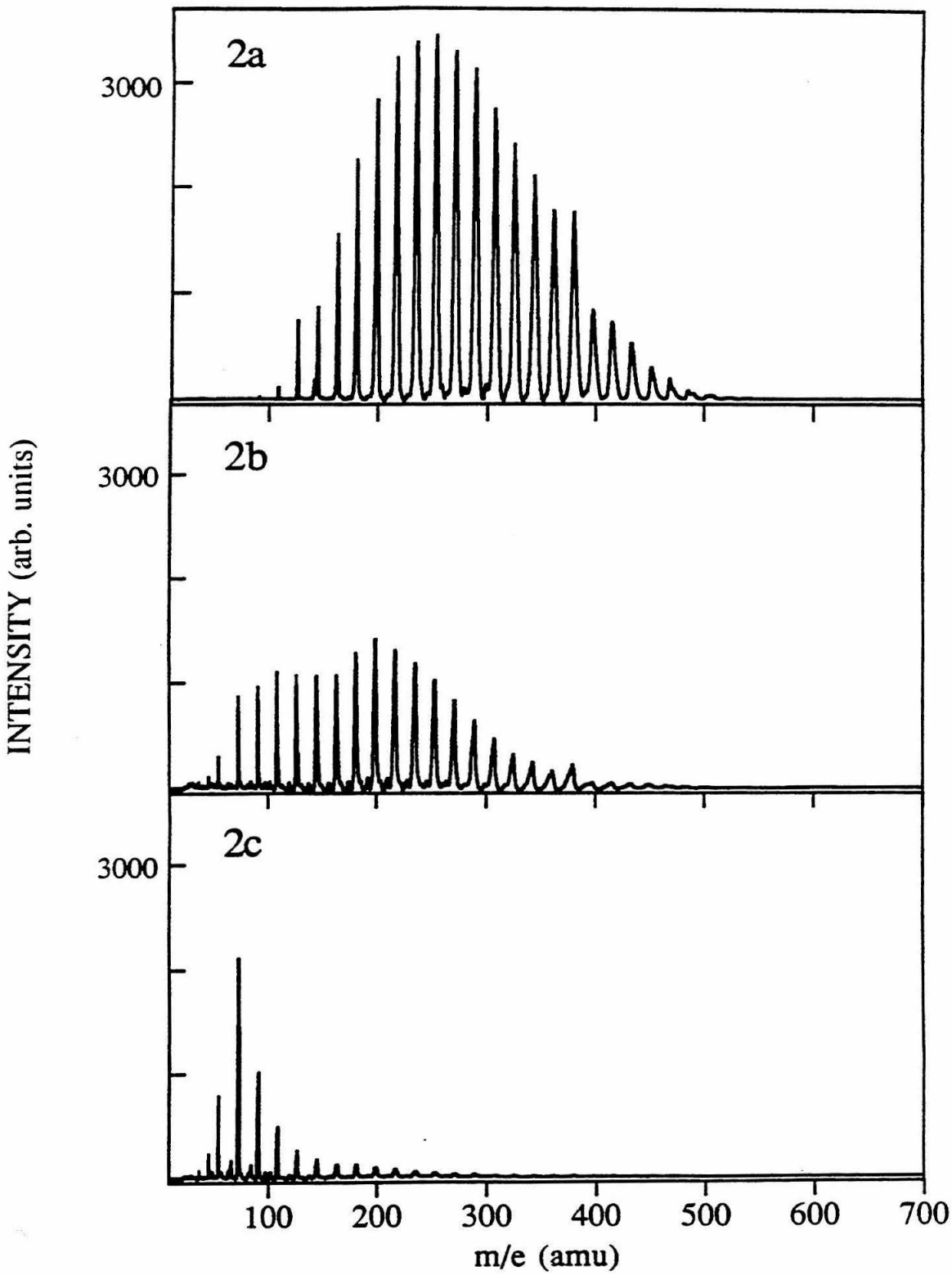
2a
3000
2b
3000
2c
3000
INTENSITY (arb. units)
100
200
300
400
500
600
700
m/e (amu)

Figure 2

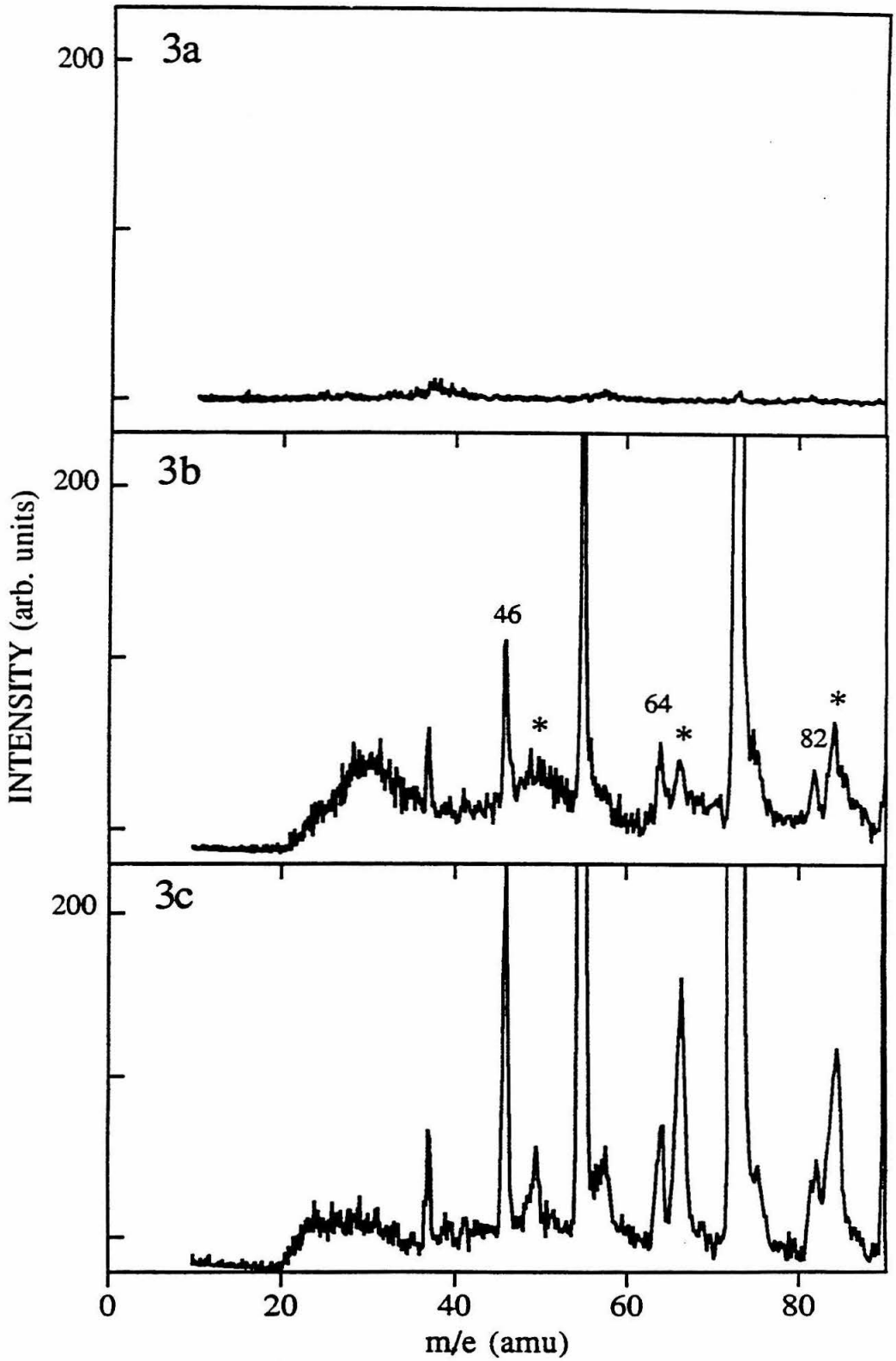
3a
200
3b
200
46
*
64
*
82
*
3c
200
INTENSITY (arb. units)
0
20
40
60
80
m/e (amu)

Figure 3

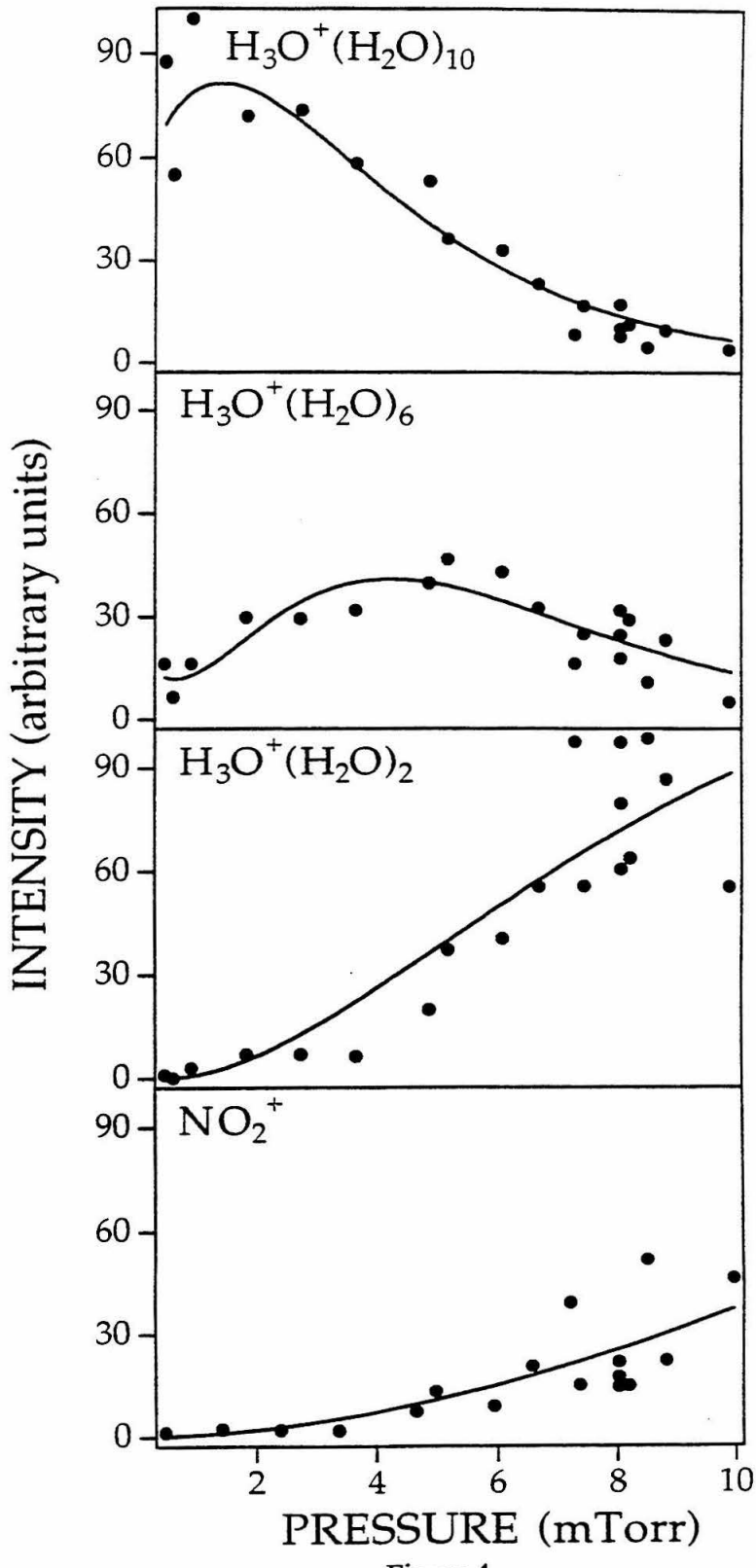
$H_3O^+(H_2O)_{10}$
$H_3O^+(H_2O)_6$
$H_3O^+(H_2O)_2$
NO_2^+
90
60
30
0
INTENSITY (arbitrary units)
2
4
6
8
10
PRESSURE (mTorr)

Figure 4

Chapter 2:

Photodissociation Dynamics of $ClONO_2$ at 193 and 248 nm: Evidence of the ClO + NO_2 Channel

ABSTRACT

Photodissociation dynamics of chlorine nitrate, $ClONO_2$, were investigated at 193 and 248 nm using the molecular beam technique of photofragmentation translational energy spectroscopy. At both wavelengths, the predominant dissociation channels were Cl + NO_3 (Φ_{193nm}= 0.66, Φ_{248nm}= 0.57) and ClO + NO_2 (Φ_{193nm}= 0.34, Φ_{248nm}= 0.43). We saw no evidence at either wavelength of the previously observed ClONO + $O(^3P)$ channel. Channel assignments were confirmed by momentum matching the two counterfragments from each channel. A one-dimensional stratospheric model using our new 248 nm branching ratio was employed to determined how our results would affect the predicted Cl_x and NO_x partitioning in the stratosphere.

I. INTRODUCTION

Catalytic cycles involving Cl_x and NO_x play central roles in regulating ozone abundance in the lower stratosphere.[1-5] Understanding the interactive balance between these species is a key issue in determining the net potential for ozone depletion. The two radical families are closely coupled through the formation and photolysis of the reservoir compound chlorine nitrate ($ClONO_2$). Many photolytic pathways are possible

(1)	$ClONO_2 + h\nu \longrightarrow ClO + NO_2$	26 kcal/mol
(2)	$\longrightarrow Cl + NO_3$	40 kcal/mol
(3)	$\longrightarrow ClONO + O(^3P)$	65 kcal/mol
(4)	$\longrightarrow Cl + NO_2 + O(^3P)$	90 kcal/mol
(5)	$\longrightarrow ClONO + O(^1D)$	110 kcal/mol

Depending on which channel is accessed either a decrease or an increase in the catalytic destruction of odd oxygen could result.[6] The production of Cl radicals via channel 2 is predicted to result in a larger depletion of ozone in the lower stratosphere than channels 1 or 3. Thus, understanding the photolytic processes of $ClONO_2$ is imperative to developing reliable and accurate models of stratospheric chemistry.

Previous photolytic studies on chlorine nitrate using a variety of experimental approaches have obtained conflicting results. Two studies deduced that the ClONO + $O(^3P)$ is the predominant pathway even though it is a spin forbidden process. Smith *et al.*[7] inferred this result using end product analysis after irradiating a neat sample of chlorine nitrate with 302.5 nm light. Adler-Golden and Wiesenfeld[8] alternatively used a broad-band UV source and atomic absorption spectroscopy to reach the same conclusion. They monitored the appearance of $O(^3P)$ by probing the $^3S_1 \leftarrow {}^3P_{2,1,0}$ transition at 131 nm. The existence of the $Cl + NO_3$ channel was ruled out when they saw no signal from the $Cl[4s(^2P_{3/2,1/2}) \leftarrow 3p(^2P_{3/2,1/2})]$ transition.

On the other hand, five other experiments determined that $Cl + NO_3$ was dominant.

Using a very low pressure photolysis technique and a high pressure xenon lamp, Chang *et al.*[9] calculated an atomic chlorine quantum yield of $\Phi_{Cl} = 1.0 \pm 0.2$. This quantum yield was determined from both the amount of Cl_2 formed in neat chlorine nitrate samples and the amount of HCl produced in $C_2H_6/ClONO_2$ mixtures. They directly detected the NO_3 counterfragment with a mass spectrometer and calibrated their measurements by the decrease in intensity of the *m/e*=62 (NO_3^+) peak when the reaction mixture was titrated with NO; $NO + NO_3 \rightarrow 2NO_2$. From this they calculated a quantum yield for NO_3 of $\Phi_{NO_3} = 0.5 \pm 0.3$. Using a similar titration technique involving NO, $ClO + NO \rightarrow Cl + NO_2$, they saw no evidence for the production of ClO. Additionally, $O(^3P)$ or $O(^1D)$ formation was also found to be negligible when NO_2 and N_2O were added; $NO_2 + O(^3P) \rightarrow NO + O_2$, $N_2O + O(^1D) \rightarrow 2NO$, $N_2O + O(^1D) \rightarrow N_2 + O_2$.

Marinelli and Johnston[10] alternatively used a flash photolysis/laser absorption experiment to measure a NO_3 quantum yield of $\Phi_{NO_3} = 0.55$. NO_3 formation was monitored by probing the $NO_3(v = 0,0)$ transition at 662 nm. They did not attempt to look for evidence of other contributing channels or the chlorine counterfragment, so their results only confirm the presence of the $Cl + NO_3$ channel but do not exclude contributions from other channels.

Using atomic resonance fluorescence spectroscopy, Margitan[11] determined the Cl and $O(^3P)$ quantum yields at 266 nm and 355 nm. He observed no discernible difference in the yields at the two wavelengths and reported the averaged values of $\Phi_{Cl} = 0.9 \pm 0.1$ and $\Phi_O = 0.1$. ClO production was checked by adding NO to the photolysis mixture. He saw no change in Cl concentration when the NO was present and thus determined that the $ClO + NO_2$ channel did not exist.

Knauth *et al.*[12] also studied the photolysis of chlorine nitrate at two wavelengths, 263 and 313 nm. They photolyzed $ClONO_2$ in the presence of NO_2 and used end product analysis to establish that $Cl + NO_3$ was the predominant channel.

Finally, Burrows *et al.*[13] used a variety of flow and static cell techniques coupled with FTIR matrix isolation spectroscopy at 254 nm. They deduced that Cl + NO_3 is the primary mechanism with a minor contribution from ClONO + O(^3P). They monitored the production of O(^3P) by the appearance of ozone which was detected by absorption at 270 nm and found that the O(^3P) quantum yield exceeded the ClONO quantum yield. They also observed the production of NO_2 when $ClONO_2$ was photolyzed which they attributed to either Cl + NO_2 + O(^3P) or secondary chemical reactions. They made no attempt to directly measure ClO production.

None of these previous experiments determined ClO + NO_2 to be a major channel, even though it is energetically the lowest channel by 14 kcal/mol. In order for the the higher energy bonds to break exclusively, the electronic transitions must be highly localized over these specific bonds and dissociation must occur on a time scale fast enough for none of the excitation energy to delocalize throughout the molecule. The absorption spectra of $ClONO_2$ does lend credence to this theory. It shows two strong absorption bands in the 190-310 nm region (see Figure 1). The band centered around 220 nm is attributed to the Cl($3P$)$\rightarrow\sigma^*$ transition. All of the previous studies have been performed at wavelengths which appear to correspond to this transition. The rise to the lower side of 195 nm is the trailing edge of the $\pi\rightarrow\pi^*$ transition. If the excitation energy is localized as previous experiments predict, exciting the $ClONO_2$ molecule at two wavelengths which correspond to two different transitions should result in unique dissociation dynamics at each wavelength. Since previous experiments suggest that the Cl($3P$)$\rightarrow\sigma^*$ transition is localized on the ClO chromophore,[14] exciting chlorine nitrate at 248 nm should lead to atomic chlorine production. Whereas, exciting the molecule at 193 nm which correlates to the $\pi\rightarrow\pi^*$ transition should lead to atomic oxygen formation.

Additionally, all of these previous experiments have large discrepencies between the Cl and NO_3 quantum yields. If Cl + NO_3 is in fact the primary dissociation channel,

then all of these experiments have failed to detect approximately 50% of the NO_3 photoproduct. Reasons for the unobserved NO_3 products usually invoke accessing the Cl + NO_2 + $O(^3P)$ channel, however, none of the experiments have been able to detect $O(^3P)$ quantum yields large enough to account for this explanation.

We investigated the photodissociation of chlorine nitrate at 193 nm and 248 nm using photofragmentation translational energy spectroscopy in order to answer questions concerning wavelength dependence and the small NO_3 quantum yield. Our technique allowed us to directly detect all of the primary photoproducts in a collision free environment. Thus, any interference from secondary intermolecular reactions is eliminated. We were also able to obtain detailed information about the photoproducts' recoil velocities and angular distributions enabling us to determine branching ratios, partitioning of energy in the photoproducts, extent of secondary dissociation, and heats of formation for unstable photoproducts. We present conclusive evidence that at both wavelengths ClO + NO_2 is a major dissociation channel; a result missed in all previous chlorine nitrate photolysis experiments. Our results also confirm the presence of the Cl + NO_3 channel and show that the ClONO + $O(^3P)$ channel does not exist.

II. EXPERIMENT

We performed the experiment on a crossed molecular beams apparatus modified for laser photodissociation of a single molecular beam (see Figure 2). The instrument, described in detail elsewhere,[15] is located at the Jet Propulsion Laboratory. A supersonic molecular beam was crossed at right angles with the focused output of a pulsed ultraviolet laser. The photodissociation products were detected off-axis in the plane of the laser and molecular beams with a rotatable mass spectrometer which consists of an ionizer, a quadrupole mass filter and a Daly ion detector. Since the detector only observed fragments which scattered out of the molecular beam as a result of photodissociation, contaminants in

the beam which do not dissociate are constrained to the beam axis and thus do not contribute to signal.

A continuous molecular beam was formed by flowing helium over liquid $ClONO_2$ (-60°C, vapor pressure = 6.7 torr) to a stagnation pressure of 200 torr and expanding the mixture through a 0.1 mm diameter water-cooled glass nozzle (4.9°C). To prevent decomposition of the $ClONO_2$, the inlet gas-line was constructed of Teflon tubing with stainless steel fittings sealed by Kalrez O-rings. The beam source had two stages of differential pumping. A skimmer (0.76 mm diam.) mounted 6.4 mm downstream from the nozzle defined the beam's angular divergence to 3.4°. A rectangular aperture (1.7 mm horizontal by 2.2 mm) mounted on the differential wall further defined the beam to a 2.3 m by 3.0 mm spot at the interaction region. The rectangular aperture also served to reduce the amount of effusive background entering the detector at small viewing angles. The beam traveled 4.8 cm before intersecting the laser beam. We estimated that the $ClONO_2$ density in the interaction region was $\sim 10^{11}$ molecules/cm^3.

The photodissociation products traveled 34.1 cm to a Brinks electron bombardment ionizer. The electron energy was nominally 160 eV, but was somewhat lower due to space charge. The ion products were then mass analyzed with a quadrupole mass filter. The mass filter resolution was set low in order to minimize mass discrimination. We collected the time-of-flight (TOF) signals of photodissociation products using an EG&G Ortec 4096 channel scaler set at a 2 μs dwell time.

The ultraviolet radiation source was a Lambda Physik EMG 101 excimer laser using the ArF (193 nm) or KrF (248 nm) transitions at a repetition rate of 40 Hz. Typical maximum pulse energies at 193 nm were 160-210 mJ/pulse and at 248 nm were 230-275 mJ/pulse. The unpolarized, rectangular-shaped laser beam was focused horizontally with a +600 mm focal length CaF_2 cylindrical lens and an ultraviolet grade fused silica focal length +300 mm plano-convex lens to a 0.1 cm^2 spot at the interaction region.

Laser power dependence measurements were taken to determine the optimum conditions for recording TOF spectra. We attenuated the laser powers using quartz slides and chose power levels which corresponded to sufficient signal with the minimum amount of stimulated secondary photodissociation. This proved to be critical for the m/e=35 signal at 248 nm as the ClO absorption cross-section there is much greater than $ClONO_2$ (see Figure 1). At 193 nm, this problem is greatly reduced since the ClO absorption cross-section is much less in this region. At 248 nm, the attenuated laser pulse energies were 46-60 mJ/pulse in the interaction region in a 2.4 mm horizontal by 4.7 mm spot. For the 193 nm experiments, the attenuated pulse energies were 14-25 mJ/pulse of lower with a spot size of 2.3 mm horizontal by 3.3 mm. Pump oil on the optics rapidly photolyzed at 193 nm forming a film which could reduce the pulse energy at the interaction region by as much as 75%.

$ClONO_2$ was synthesized from Cl_2O and N_2O_5 using Schmeisser's technique.[16] We purified the sample using trap-to-trap distillation at 195 K and 175 K to remove Cl_2 and Cl_2O impurities. We further removed nitric acid by cannulating the $ClONO_2$ off of the solid HNO_3 at 195 K. The purity of the beam was checked with the mass spectrometer.

The molecular beam velocity distribution of the parent molecules was determined by fitting TOF measurements of the beam to an assumed velocity distribution $N(v) \propto v^2 \exp[-(v/\alpha - S)^2]$. $N(v)$ is the number density of molecules with speeds in the range v to dv, α is the width of the speed distribution as measured by an observer in the beam and S is the speed ratio which is defined as $S=v_s/\alpha$ where v_s is the mean stream velocity.[17,18] The TOF measurements were obtained using a "single shot" slotted disk to chop the beam. During the photodissociation experiments, when the chopper wheel was removed, we intermittently confirmed the stability of the beam velocity using a "hole-burning" method. In hole-burning, the detector is aligned along the molecular beam axis and tuned to a fragment ion mass of the parent; when the parent ion photodissociates the products scatter

out of the beam giving rise to a "hole" in the spectrum. The location and shape of the "hole" contain the information pertaining to the beam velocity and distribution. From the TOF measurements, we calculated a $ClONO_2$ beam velocity of $1.3x10^5$ cm/s with a velocity spread (FWHM) of 9%.

The measured TOF is the total time for a photofragment to travel from the interaction region to the ionizer and after the ionization for the resultant ion to travel through the mass filter to the ion detector. The neutral TOF from the interaction region to the ionizer is determined by subtracting the ion flight time from the measured TOF. The ion flight time for a singly charged ion with a mass to charge ratio *m/e* was experimentally determined and was expressed in microseconds by the formula $\alpha(m/e)^{1/2}$ where the parameter α is a function of ion energy and other spectrometric parameters and is equal to 3.54.

At both wavelengths, TOF distributions were collected at *m/e*=51, 35, 81, 62, 46, 30 and 16 corresponding to ClO^+, Cl^+, $ClONO^+$, NO_3^+, NO_2^+, NO^+ and O^+. The TOFs were recorded at detector angles of 10° to 50° and were averaged for 100,000 to 1,000,000 laser pulses. At 193 nm, an additional *m/e*=35 TOF spectrum was recorded at 123°. At 248 nm, the $ClONO^+$ TOF distribution was also recorded at 7° where we observed no significant signal. TOF spectra were also recorded at 7°, to check for possible cracking products of ClONO, ClO^+ and NO_2^+, but showed no evidence of ClONO. To check for the possible concerted reaction, $ClONO_2 \rightarrow ClON + O_2$, a TOF at *m/e*=32 ($O_2^+$) was recorded at 20° (25,000 laser pulses). No signal was observed.

At 248 nm, the respective counts/laser pulse at the peak channel for *m/e*=35, 51, 46 and 30 at a detector angle of 30° were 0.0124, 0.0048, 0.0127 and 0.0081. The *m/e*=16 TOF recorded at 45° had 0.0276 counts/pulse at the peak channel. We observed no significant signal at *m/e*=62.

At 193 nm, the respective counts/laser pulse at the peak channel for *m/e*=35, 51, 30

and 16 with a detector angle of 30° were 0.0164, 0.0114, 0.0053 and 0.0184. The *m/e*=46 TOF recorded at 20° had 0.0446 counts/pulse at the peak channel. We observed no significant signal at *m/e*=62 (30°) or *m/e*=81 (10°).

At both 193 and 248 nm, angular distributions for *m/e*=35 and 51 were recorded. The detector angles ranged from 10° to 50°. The *m/e*=51 TOF were recorded in 5° increments with four scans for a total of 40,000 laser pulses at each incremental angle. The *m/e*=35 scans were recorded in 10° increments for a total of 80,000 laser pulses at each angle.

To ensure the correct relative signal intensities between the *m/e*=35 and *m/e*=51 signals, TOFs at the two masses were recorded in an alternating manner. Scans of 10,000 laser pulses per scan were recorded alternating between the two masses for a total of 200,000 laser pulses at each mass. If laser power fluctuations of drift occurred, this technique guaranteed that the relative signals were correct for the branching ratio calculations. At 248 nm, the measurements were made at 20° and 30°. The 193 nm measurements were recorded at 20° and 40° and were averaged for only 100,000 laser pulses.

III. RESULTS AND ANALYSIS

Neutral photofragments scatter out of the interaction region with velocities equal to the vector sum of the molecular beam velocity and the recoil velocity imparted by dissociation. Velocity vector or Newton diagrams are shown in Figure 3. For the experimental TOF and angular distributions, we derived the center-of-mass (c.m.) translational energy distributions $P(E_T)$ and the c.m. angular distributions $\omega(\theta)$ of the photofragments. For a single photon absorption, $\omega(\theta)$ must have the form $\omega(\theta) = 1/4\pi[1+\beta P_2(\cos\theta)]$,[19,20] where P_2 denotes the second order Legendre polynomial and θ the angle between the electric field vector of the photon and the product recoil

direction in the c.m. frame. β is the anisotropy parameter and must lie in the range $-1 \leq \beta \leq 2$. For a direct dissociation on a repulsive surface, β reflects the orientation of the transition moment with respect to the bond dissociation axis. When the dipole is parallel to the dissociation axis, β is 2 and $\omega(\theta)$ reduces to a $\cos^2\theta$ angular distribution. For a perpendicular transition, β is -1 and $\omega(\theta)$ reduces to a $\sin^2\theta$ angular distribution.

The $P(E_T)$ distribution and β are determined using a forward convolution technique. Trial distributions are convoluted with parameters such as the velocity distribution of the molecular beam, the effective ionizer length, the angular divergence of the molecular beam and the detector acceptance angle. The resulting calculated TOF distributions are then compared with the experimental data. β and the $P(E_T)$ distribution are varied until the TOF spectra at all angles are fit simultaneously.

248 nm

Figure 3 shows the Newton diagram for the two channels observed from the photodissociation of $ClONO_2$ at 248 nm. The TOF spectra and best fits at various angles for the *m/e*=51 (ClO^+) signal are shown in Figure 4. We observed a prominent peak which we assigned to ClO recoiling from NO_2. The assignment of this channel was confirmed by momentum matching the two product fragments as is discussed below. Based on this assignment, we fit the observed *m/e*=51 TOF spectra in Figure 4 using the $P(E_T)$ distribution displayed in Figure 5. The total energy available for translation $E_{avl} = h\nu - D_0(ClO\text{-}NO_2)$ indicated in the figure is 89 kcal/mol which assumes no internal energy in the parent. The average translational energy $\langle E_T \rangle$ of 22.6 kcal/mol is 25% of E_{avl}. We fit the measured angular distribution and found an anisotropy parameter of $1.1 \leq \beta \leq 1.4$, indicative of a predominantly parallel transition.

An incidental feature at small angles is the long slow tail. At 7°, a distinct peak is resolved with a maximum around 275 μs (see Figure 6). As the $ClONO_2$ concentration in

the molecular beam increased, the signal intensity of this peak relative to the primary peak also increased. The shift in arrival times is due to changes in the beam velocity as the composition of the beam is altered. This pressure dependence indicates that the second peak in the *m/e*=51 spectra is due to $ClONO_2$ clusters in the molecular beam and not ClONO cracking in the ionizer. No observable peak was apparent at *m/e*=81 and we were unable to find a peak at *m/e*=16 that would correspond to an oxygen atom recoiling from ClONO. Overall, we found no evidence to support the ClONO + $O(^3P)$ channel.

The TOF spectra for the *m/e*=35 signal at various angles are shown in Figure 7. Two components are apparent. The slower peak can be fit using the $P(E_T)$ and β calculated from the *m/e*=51 data, with a small correction for the difference between the *m/e*=51 and *m/e*=35 ion flight times. Thus, this peak is the result of ClO from the ClO + NO_2 channel cracking in the ionizer to Cl^+. The fast, sharp peak was not observed in higher *m/e* TOF spectra, and we assigned it to chlorine atoms generated form the Cl + NO_3 channel. None of the larger Cl containing fragments, e.g., ClONO, could be formed with such high velocities without violating energetic or kinematic constraints. The channel assignment was also confirmed using momentum matching. The $P(E_T)$ for the Cl + NO_3 channel is displayed in Figure 5. E_{avl} is marked (75 kcal/mol) and was calculated assuming that the chlorine atom is formed in the ground state, $^2P_{3/2}$. $\langle E_T \rangle$ is 40.7 kcal/mol which is 54% of E_{avl}. The laboratory angular distribution was fit with an anisotropy parameter of β~0.5.

All of the spectra at *m/e*=35 were taken using low laser powers in order to limit stimulated secondary photodissociation. At 248 nm, the ClO absorption cross-section is much greater than $ClONO_2$ (see Figure 2); therefore, ClO may absorb a second photon and photodissociate to form Cl and $O(^1D)$.[21] Figure 8 compares the *m/e*=35 TOF spectra taken at 10° using low and high laser powers. The peak arriving at t~250 μs and the shoulder on the slow side of the sharp peak arising from the Cl + NO_3 channel are both due to atomic

chlorine produced form stimulated secondary dissociation. In the laboratory frame of reference, these secondary photofragments may be formed with either higher or lower translational energies than the parent molecule depending on whether the fragments recoiled forward into or backward away from the detector. Because the ClO absorption transition is predominantly parallel ($\beta \sim 1.0$)[22] and the primary channel $ClO + NO_2$ is predominantly parallel ($\beta \sim 1.3$), the net angular distribution for Cl and O are weighted in a $\cos^n\theta$ distribution with $n \sim 3$-4. Thus, the signal is enhanced at smaller angles and is negligible at wider angles.

The assignment of the peaks to the various reaction channels can be confirmed using momentum matching. In the c.m. frame of reference, both fragments form a two-body primary photodissociation process will have equal and opposite momenta; thus the $P(E_T)$ and β obtained from fitting the Cl peak should also fit the signal from NO_3.[23] We observed no signal at *m/e*=62 (NO_3^+). However, NO_3 readily fragments under our ionizer conditions and is unobservable at *m/e*=62. At *m/e*=46 (NO_2^+) (see Figure 9), we find that the observed peak closely matches the calculated TOF distribution for NO_3 using the $P(E_T)$ and β for the $Cl + NO_3$ channel determined from the *m/e*=35 data. A fit using the $P(E_T)$ and β for the $ClO + NO_2$ channel determined form the *m/e*=51 data (dotted line) predicts the peak to arrive at slightly faster times and does not give a satisfactory fit for the TOF spectrum at *m/e*=46. Since the leading edge of the spectrum nicely fits the $Cl + NO_3$ channel, we deduce that NO_2 also cracks in the ionizer.

The tail of the fit predicts more signal at the trailing edge of the peak than was observed. This loss of signal is due to spontaneous secondary dissociation of metastable NO_3 fragments before they reach the ionizer. Excess energy that is not partitioned into translation will remain in the photofragments as internal energy. The trailing edge of the calculated fit corresponds to NO_3 fragments with internal energies which are greater than the bond dissociation energy of NO_3. We calculated a new $P(E_T)$ to fit the *m/e*=46 data

(see Figure 5). The shaded area corresponds to uncertainties in the fit. The cut-off of the $P(E_T)$ is 19 $^{+4}/_{-2}$ kcal/mol.

Figure 9 shows the experimental data and best fits for *m/e*=30 at 30°. The TOF spectrum consists of a central peak with a fast shoulder and a broad tail at longer times. The central peak is due to NO_3 cracking in the ionizer to form NO^+. Unlike the *m/e*=46 peak, the leading edge does not fit well. By combining fits calculated using the $P(E_T)$ and β from both the ClO + NO_2 and the Cl + NO_3 channels, we were able to calculate an accurate fit. This corroborates the theory that both NO_3 and NO_2 crack in the ionizer and therefore are not detectable at their parent masses. The underlying signal at the leading and trailing edges of the spectrum are due to secondary products arising from the spontaneous dissociation of NO_3 fragments in the flight path.

193 nm

The *m/e*=51 and *m/e*=35 TOF spectra from the photodissociation of chlorine nitrate at 193 nm are shown in Figures 10 and 11. Strong similarities to the 248 nm results are apparent. At *m/e*=51, a single peak was observed which we assigned to ClO arising from the ClO + NO_2 channel. This spectra was fit using the $P(E_T)$ shown in Figure 12 with an anisotropy parameter of $0.1 \leq \beta \leq 0.4$. The average translational energy of this channel was 22.5 kcal/mol which is 18% of E_{avl}. As at 248 nm, there was some contribution from clusters in the molecular beam at smaller angles.

The *m/e*=35 TOF had two components. The faster sharper peak was assigned to the Cl + NO_3 channel while the slower peak was attributed to ClO from the ClO + NO_2 channel. The Cl + NO_3 spectra was fit using the $P(E_T)$ shown in Figure 12 with $\beta \sim 0.5$. The average translational energy for the Cl + NO_3 channel was 42.8 kcal/mol which is 40% of E_{avl}. As at 248 nm, we attenuated the laser power for the *m/e*=35 TOF measurements to limit the amount of stimulated secondary photodissociation of ClO,

however, this is not as critical at 193 nm since the ClO absorption cross-section is much less here.

Figure 13 displays the *m/e*=46 (20°) and *m/e*=30 (30°) TOF spectra. The *m/e*=46 spectrum consists of a sharp peak followed by a long broad tail. The fits calculated using the $P(E_T)$s and βs obtained from the *m/e*=51 and *m/e*=35 data do not accurately fit the data. However, much of the NO_3 is formed with internal energies sufficient for NO_3 to undergo spontaneous secondary dissociation. If the $P(E_T)$ for the Cl + NO_3 channel obtained from the *m/e*=35 data was truncated at translational energies which corresponded to internal energies in the NO_3 fragment equal to or greater than the NO_2–O bond strength, we could accurately fit the fast sharp peak arriving at 139 μs. The early part of the slow shoulder could be accounted for assuming NO_2 arising from the ClO + NO_2 channel. Signal at longer times was due to neutral NO_2 arising from the secondary dissociation of NO_3. At 248 nm, the NO_3 signal swamped out the signal from neutral NO_2, however, at 193 nm most of the NO_3 is undergoing secondary dissociation so we are able to see the weak underlying neutral NO_2 signal.

The *m/e*=30 data recorded at 30° is accurately fit using the truncated $P(E_T)$ for the Cl + NO_3 channel and the full $P(E_T)$ for the ClO + NO_2 channel except for some signal at the leading and trailing edges. The spectrum was taken at low laser powers but stimulated secondary photodissociation of the NO_3 fragment is still possible. The absorption cross-section of NO_3 at 193 nm is not known, however, it is predicted to be large from comparison with other nitrate containing molecules. The extra signal at the edges can be accounted for using stimulated and spontaneous secondary dissociation of the NO_3 fragment.

IV. BRANCHING RATIO

The ion flux detected at a specific mass is directly proportional to the total flux of a neutral product at the ionizer. The ion flux at *m/e*=35 due to neutral ClO at the ionizer is

$$I^{+}_{ClO}(m/e=35) = I_{ClO} \cdot \sigma_{ClO} \cdot f_{ClO}(m/e=35) \qquad \text{Eqn. 1}$$

I_{ClO} is the total flux of neutral ClO at the ionizer, σ_{ClO} is the total ionization cross-section for ClO, and $f_{ClO}(m/e=35)$ is the fraction of ClO that is detected at *m/e*=35. $f_{ClO}(m/e=35)$ was determined from only the *m/e*=35 and *m/e*=51 data, since the ClO signal at *m/e*=16 was negligible. A similar expression can be derived for Cl products with $f_{Cl}(m/e=35)=1$. From these expressions, we can derive the ratio of neutral ClO and Cl at the ionizer

$$\frac{I_{ClO}}{I_{Cl}} = \frac{I^{+}_{ClO}(m/e=35)}{I^{+}_{Cl}(m/e=35)} \cdot \frac{\sigma_{Cl}}{\sigma_{ClO}} \cdot \frac{f_{Cl}(m/e=35)}{f_{ClO}(m/e=35)} \qquad \text{Eqn. 2}$$

A Cl_2O photodissociation experiment allowed us to calcualte the ionization cross-section ratio for Cl and ClO since the neutral product ratio of Cl versus ClO is unity.

$$\frac{\sigma_{Cl}}{\sigma_{ClO}} = \frac{I^{+,Cl_2O}_{Cl}(m/e=35)}{I^{+,Cl_2O}_{ClO}(m/e=35)} \cdot f^{Cl_2O}_{ClO}(m/e=35) \qquad \text{Eqn. 3}$$

The Cl_2O experiment was performed at 308 nm because at shorter wavelengths spontaneous secondary dissociation of the ClO fragment prevented us from obtaining an accurate value for $f^{Cl_2O}_{ClO}(m/e=35)$. Also at 308 nm, the Cl_2 + O channel is energetically inaccessible. The experimental and fitting details of the Cl_2O experiment are described in our subsequent paper.

In the $ClONO_2$ photodissociation experiments, we observed only the Cl + NO_3 and ClO + NO_2 channels; thus, the ratio of neutral ClO and Cl at the ionizer is equal to the branching ratio.

$$\frac{I_{ClO}^{ClONO_2}}{I_{Cl}^{ClONO_2}} = \frac{I_{Cl}^{+,Cl_2O}(m/e=35)}{I_{Cl}^{+,Cl_2O}(m/e=35)} \cdot \frac{f_{ClO}^{Cl_2O}}{f_{ClO}^{ClONO_2}} \cdot \frac{I_{ClO}^{+,ClONO_2}(m/e=35)}{I_{Cl}^{+,ClONO_2}(m/e=35)} \qquad \text{Eqn. 4}$$

The values used to calculate the branching ratios were determined from TOF distributions which were collected using the alternating method. The branching ratios for the photodissociation of $ClONO_2$ at 193 and 248 nm are

Wavelength	$Cl + NO_3$	$ClO + NO_2$
248 nm	0.54 ± 0.8	0.46 ± 0.8
193 nm	0.64 ± 0.8	0.36 ± 0.8

In the Cl_2O experiments, we were unable to get a precise fit due to some minor experimental errors introduced because of the instability of the molecular beam and slight misalignments problems. We determined the opitmum ratio for $I_{ClO}^{+,Cl_2O}(m/e=35)$ and $I_{Cl}^{+,Cl_2O}(m/e=35)$ by averaging the best fitting values obtained at various angles. The $f_{ClO}(m/e=35)$ values for the Cl_2O and the $ClONO_2$ were not equal because ClO from the photolysis of $ClONO_2$ at 193 and 248 nm fragmented more in the ionizer than ClO from Cl_2O photolysis at 308 nm.

V. DISCUSSION

The quantitative results from our experiments are collected in Table I. Comparing the dissociation dynamics at 193 and 248 nm, many similarities, such as branching ratios, energy partitioning, and the Cl + NO_3 anisotropy parameter, are apparent. At both wavelengths, we observed similar yields from the ClO + NO_2 and Cl + NO_3 channels and found no evidence for the ClONO + O(^3P) channel. Also, the maximum and average amounts of available energy partitioned into translation (E_T(max)/E_{avl} and $\langle E_T \rangle / E_{avl}$, respectively) for the two channels were wavelength independent.

We observed a large yield of ClO at both wavelengths [Φ_{ClO}(193 nm)=0.36 and Φ_{ClO} (193 nm)=0.46]; a result not detected in previous chlorine nitrate photolysis experiments. The similarity in branching ratios at the two wavelengths indicates that electronic transitions in chlorine nitrate are not highly localized as previously thought, since 193 and 248 nm correspond to two different electronic transitions in the molecule. If the excitation energy was localize in specific bonds, the branching ratios for the two wavelengths should have been markedly different. An interesting feature about our new branching ratios was that we observed a larger yield of atomic chlorine at 193 nm than at 248 nm. This indicates that the Cl($3P$)$\rightarrow\sigma^*$ transition may occur at wavelengths shorter than previously thought and that the absorption band centered around 220 nm may in fact be due to a $\pi\rightarrow\pi^*$ transition localized on the NO_2 moiety instead.

An anomaly in the dynamics is the large discrepancy in the β value for the ClO + NO_2 channel at the two wavelengths. Here we examine some of the factors that could account for this large difference. One explanation is that a different excited state of $ClONO_2$ is accessed at each wavelength. Information about the initially prepared excited states can be obtained from the anisotropy results using a simple recoil model (see Appendix C). Assuming that the molecule dissociates instantaneously on absorption of the photon and that the kinetic energy of dissociation is very large compared to the kinetic

energy of rotation, β has the form $\beta=2P_2(\cos\theta)$. By assuming a single electronic transition in the parent molecule leads to both channels, we calculated the orientation of the transition moment.

At 248 nm, we found that the angular distributions for both the ClO + NO_2 ($\beta \sim 1.3$) and Cl + NO_3 ($\beta \sim 0.5$) channels could be accounted for by a transition moment located in the plane of the molecule. However, at 193 nm to simultaneously satisfy the β values for the two channels, the transition moment must rotate out of the symmetry plane of the parent molecule. The difference in the calculated transition moments, in-plane versus out-of-plane, along with the absorption spectrum of chlorine nitrate lend credence to the theory that at each wavelength a different excited state is accessed. However, the similarities in the rest of the dissociation dynamics at the two wavelengths, such as branching ratios and energy partitioning, indicate elsewise.

Distortion of the excited complex before dissociation could also account for the reduction in β at 193 nm by changing the recoil direction of the fragments in the c.m. frame. Using a rigid radical impulsive model,[24,25] we predicted from the ground state geometry of $ClONO_2$ the fraction of available energy which theoretically could be partitioned into translation. This fraction reflects the maximum amount of energy that could appear in translation (assuming no distortion) because a softer radical would channel energy into vibration and reduce the ratio. At both 193 and 248 nm, some products from the Cl + NO_3 channel are formed with translational energies exceeding the rigid radical model predictions indicating that distortion must be occurring. The ClO + NO_2 channel, on the other hand, has $E_T(\max)/E_{avl}$ values (~0.5) which can be explained without distortion. Note though that while the rigid radical model is useful for predicting when distortion must be occurring, distortion might still be occurring if the translational energy is less than or equal to the values predicted by the model. For example, if deformation resulted in vibrational excitation of the radical, the rigid picture would not apply. In

addition, bending does not have to occur only in the excited complex. Depending on the wavelength, Franck-Condon factors might favor absorption from a distorted ground state. The similarities in energy partitioning indicate that dissociation is occurring on the same potential surface at both wavelengths contradicting the transition moment calculations. Distortion of the excited state though would change the results obtained from the transition moment calculations. If dissociation at both wavelengths was occurring on the same surface, the differences in β would reflect the extent of distortion in the excited complex. However, as the excited complex distorts so should the exit impact parameter which would affect the fraction of available energy partitioned into translation; a result which we do not observe.

Rotational and vibrational motion of the parent molecule could also lower β by imparting a velocity component perpendicular to the axial velocity of recoil. If the lifetime of the excited complex at 193 nm was increased, the molecule could have sufficient time to rotate prior to dissociation resulting in a more isotropic distribution and thus a lower value of β. This lengthening could be caused by a well or an exit barrier on the excited state potential energy surface. Note though that the molecular beam is produced by a supersonic expansion so rotational temperatures are expected to be very low (30-40 K). At these temperatures, rotational periods are on the order of picoseconds. Therefore, in order for rotation to account for the change in β, the lifetime of the excited state must also be on the order of picoseconds.

NO_3 Centrifugal Barrier

From our data, we concluded that some NO_3 photofragments were formed with sufficient internal energies to undergo spontaneous secondary dissociation. The minimum translational energy at which stable NO_3 radicals are formed corresponds by energy conservation to the maximum amount of internal energy at which the radicals can survive.

The difference between this threshold translational energy and the available energy is an upper limit to the sum of the Cl–ONO_2 bond energy and the required energy for NO_3 decomposition (see Figure 14). Assuming that some of the secondary products were formed vibrationally cold and knowing the Cl–ONO_2 bond dissociation energy (40 kcal/mol), we calculated the lowest transition barrier for NO_3 decomposition.

NO_3 radicals may dissociate via two channels, a direct dissociation to form NO_2 and O or a concerted reaction forming NO + O_2. Davis and Lee determined that the two channels have nearly identical barriers, with a NO_2–O bond energy of 48.6 kcal/mol and an activation barrier for the NO + O_2 channel of 48.4 kcal/mol.[26]

From examining the translational energy distribution for this channel, the maximum internal energy of an NO_3 radical in our experiment is 56 kcal/mol which is 7.4 kcal/mol greater than the values measured by Davis and Lee. Our value, however, only represents an upper bound, since greater internal energies will be required to surmount any potential or rotational barrier or to provide some minimum product excitation as the radical decomposes. Posssible reasons for our discrepency are uncertainty in the fit, formation of spin-orbit excited chlorine or a centrifugal barrier on the exit channel. The $P(E_T)$ obtained from the *m/e*=46 data truncates at 19 $^{+4}/_{-2}$ kcal/mol. The uncertainty in the fit therefore could only account for at most 4 kcal/mol of the difference. Also, if some of the Cl fragments were formed in the spin-orbit excited state $^2P_{1/2}$, the transition barrier value would be lowered by 2 kcal/mol since only 73 kcal/mol would be available for translation and internal excitation. At the extreme, these two reasons can only account for a 6 kcal/mol difference.

In order to investigate the plausibility of a centrifugal barrier on the exit channel, we calculated an effective potential energy surface from the ground state geometry of chlorine nitrate (see Appendix B). By imposing the conservation of angular momentum to the primary and secondary products, we used a soft radical model to approximate the

amount of available energy partitioned into rotational energy.[27] The model assumes that the oxygen atom initially recoils off of the chlorine atom and then proceeds to collide with the rest of the molecule, i.e., the NO_2 fragment, imparting both vibrational and rotational energy. Using this model, we determined the angular momentum of the system. Since angular momentum is conserved, a rotational potential energy surface could be calculated for the dissociation of O–NO_2. Summing the NO_3 fragment's rotational potential with a Morse potential for the O–NO_2 bond, we calculated the shape of the effective potential energy surface to determine the height of any exit barrier. The model predicts an ~18 kcal/mol centrifugal barrier which is much higher than the observed 7.4 kcal/mol. Though the model calculates a centrifugal barrier which is larger than what we observed, it does predict that enough rotational energy can be imparted to the NO_3 fragment to create a centrifugal barrier. If the NO_3 fragments were formed with rotational energies less than what the model predicts the resultant centrifugal barrier would be less that ~18 kcal/mol.

Previous Experiments

All of the previous experiments determined that either Cl + NO_3 or ClONO + $O(^3P)$ was the dominant photochemical pathway. None found evidence for the dissociation pathway which involved breaking the weakest bond, ClO + NO_2. Our molecular beam results however demonstrate conclusively that at 193 and 248 nm, ClO + NO_2 is a major photolytic channel. Our discrepancy with past experiments cannot be readily explained, so here we will examine the previous experiments in order to evaluate their evidence against the formation of ClO + NO_2.

Results from the flow cell study by Margitan are currently the accepted branching ratios for stratospheric modeling.[28] He photolyzed $ClONO_2$ at 266 nm and 355 nm in a flow reactor, detected both Cl and O atoms by resonance fluorescence, and reported absolute quantum yields of 0.9 and 0.1, respectively.[11] ClO detection was attempted using

the indirect method of titration with NO ($ClO + NO \rightarrow Cl + NO_2$). He observed no significant effect on the Cl signal upon addition of NO so an upper bound of 0.2 on the ClO yield was inferred. Unfortunately, the NO concentration was not reported, and no ClO calibration (e.g., Cl_2O photolysis) was apparently performed. Other laboratories have noted that high concentrations of NO though can interfere with the VUV resonance fluorescent intensities in such experiments.[29] While there is no a priori reason to doubt the NO titration measurements, the published information is insufficient to make an independent evaluation.

The absence of ClO signal could also arise if all of the ClO products were undergoing stimulated secondary photodissociation. Our results show that the ClO products, while hot, were not formed metastable but could still photolyze to form Cl and $O(^1D)$. This is a serious concern at 266 nm, the peak of the ClO continuum, where the ClO cross-section (σ_{ClO}=5.3 x 10^{-18} cm^2) is over 20 times larger than the $ClONO_2$ cross-section. Furthermore, at the largest pulse energy reported (40 mJ), and assuming a typical Nd:YAG spot size and shape, the ClO absorption is close to saturation. While a power dependence was performed, variations of a factor of 3 to 4 are often insufficient to reveal saturation of a secondary absorption, since the weaker absorption would lead to a linear dependence on fluence.

The possibility of ClO photolysis is also compounded by the likely inhomogeneity of the photolysis beam profile. The nonguassian transverse mode (donut pattern) of the Quanta Ray Nd:YAG laser beam is severely distorted by harmonic generation resulting in much of the intensity being concentrated in small regions of the beam spot. Furthermore, hot spots exist in the near field (<10 m) of a 266 nm quadrupled Nd:YAG beam. Most of the photolysis may be occurring in regions of high intensity, where ClO photolysis is saturated even at low energies (<10 mJ).

Oxygen atoms from the photolysis of ClO should be detected in the O atom resonance fluorescence measurements; however, for all vibrationally excited ClO (v=1 and higher), O(^1D) formation will predominate and will not contribute to the ^3P resonance fluorescence signal. With an average internal energy of ~67 kcal/mol distributed between the ClO and NO_2, the probability of ClO initially being in v=0 is small. Secondary photolysis must occur during the laser pulsewidth of 7 ns, so the ClO will not have time to relax. Additionally, the spin-orbit excited O atoms will not be efficiently quenched in the He or Ar buffer gas. Thus, the low O(^3P) signal does not preclude the occurrence of significant amounts of ClO photolysis.

The above considerations open the possibility that despite the attention to detail with which the Margitan experiment was performed, ClO photoproducts could have gone undetected. Alternatively, the discrepancy could be attributed to the different wavelengths. Although 248 and 266 nm differ by only 8 kcal/mol and there is no noticeable inflection in the absorption spectrum, a change in branching ratios cannot be ruled out.

The flashlamp study by Adler-Golden and Wiesenfeld[8] also used atomic resonance fluorescence detection but saw only atomic O and failed to detect any Cl atoms; however, their reported branching ratio is believed to be incorrect. Margitan points out that no Cl would be detected under their experimental conditions due to rapid removal of Cl by the secondary reaction $Cl + ClONO_2 \rightarrow Cl_2 + NO_3$.

The results of Marinelli and Johnston's study at 248 nm are consistent with our molecular beam results.[10] They detected NO_3 by monitoring the $NO_3(v=0,0)$ absorption at 661.9 nm and found a prompt (2 μs) NO_3 yield of 0.55 with additional NO_3 formed at later times. The total yield of NO_3 is 0.75, after extrapolating the secondary products to $t \approx 0$. These yields are now considered to be too large, because the ClNO absorption cross-section used to calibrate their laser fluences was a factor of two smaller than the currently accepted value. The NO_3 yields corrected for the new absorption cross-section are 0.28

(prompt) and 0.38 (total). The secondary NO_3 has two sources, vibrationally excited NO_3 relaxing to v=0 and products from the reaction of Cl + $ClONO_2$. The two values thus place bounds on the NO_3 yield. These results, while not in exact agreement with our experiment, imply the existence of a second channel.

Several other experiments were performed either in static cells, with end product analysis[7,12] or under steady state conditions.[9,13] None of these studies conclude that ClO + NO_2 is a major channel even though they all observed N_2O_5 which requires the presence of NO_2. In general, however, the data from these studies are difficult to explicate, since the methods are indirect and require interpreting multi-step mechanisms which include homogeneous and heterogeneous reactions. These problems in analysis become especially severe for experiments using neat $ClONO_2$ samples, since excited photoproducts will collide with $ClONO_2$ or the walls, leading to highly nonthermal reactions and dissociation probabilities.

This is the case for the experiment by Chang *et al.*,[9] the first paper to conclude that the primary channel was Cl + NO_3. Their experiment consisted of photolyzing the chlorine nitrate in a very low pressure reaction chamber coupled to a mass spectrometer; the use of an effusive cell precluded the direct detection of the primary photoproducts. Their NO_3 yield of 50 ± 30% obtained by monitoring the *m/e*=62 peak intensity agrees with our molecular beam results, however their Cl yield of 100 ± 20% determined from detecting secondary products does not. This result though could be explained if significant amounts of the ClO were undergoing stimulated secondary dissociation.

Burrows *et al.*[13] also concluded that Cl + NO_3 was dominant even though they observed a significant yield of NO_2 (Φ_{NO_2}=0.24). They dismissed the NO_2 production to contamination from thermal decomposition of $ClONO_2$, the Cl + NO_2 + O(^3P) channel, or some other secondary reactions. Our results though show that it is likely due to the ClO + NO_2 channel. Evidence of ClO is also present in their study. They investigated the

production of atomic oxygen by photolyzing $ClONO_2$ in the presence of O_2 and looked for the subsequent formation of ozone by monitoring the absorption at 270 nm (σ_{O_3} = 7.7 x 10^{-18} cm^2). Overlooked was the fact that ClO also has a strong absorption cross-section at 270 nm (σ_{ClO} = 5 x 10^{-18} cm^2). Thus, if the signal which they attributed to ozone was really from ClO absorbing, it would correlate to a ClO quantum yield of ~0.4 which agrees with our results.

With the exception of Margitan's experiment, the evidence against a significant fraction of ClO + NO_2 products is not strong, and there is even some evidence in favor of the ClO + NO_2 channel in the form of low NO_3 yields, steady state concentrations of NO_2 and N_2O_5 formation. While we cannot resolve the disagreement with Margitan's work some questions concerning their ClO measurements remain. These uncertainties lead us to believe that ClO + NO_2 is a significant channel for the photodissociation of $ClONO_2$ which was missed in all previous experiments.

Stratospheric Implications

The branching ratios relating the primary photodissociation channels of $ClONO_2$ measured in the beam experiment should be identical to the photolytic pathways in the stratosphere. From the anisotropies of the angular distributions, we conclude that dissociation occurs in less than a rotational period, i.e., picoseconds or less, orders of magnitude faster than the mean collision rate at stratospheric pressures. The dissociation of $ClONO_2$ is therefore sufficiently fast that it is an isolated process in the stratosphere and that primary product yields obtained using the molecular beam technique should be identical to the yields obtained under stratospheric conditions despite the nonequilibrium conditions of the beam. The internal energies of molecules in the beam should also approximate stratospheric temperatures. A supersonic expansion efficiently cools rotational and translational temperatures to well below 100 K, but vibrational degrees of

freedom are only partially relaxed. With similar vibrational temperatures, differences due to vibrational factors will be small. Results from the beam experiments will differ from bulk gas phase studies only for processes which occur on time-scales which are slower than the mean collision times at high pressures, i.e., dissociation of long-lived metastable parents or fragments.

Our results show that at 248 nm few metastable products are formed. With an average internal energy of ~67 kcal/mol partitioned between NO_2 and ClO, the probability is small that either fragment will be formed with sufficient internal energy to spontaneously dissociate. As for the NO_3 fragment, we know that only a small fraction (17%) of the NO_3 fragments are formed metastable.

Alternatively at 193 nm, the majority of the NO_3 fragment (86%) are formed metastable and undergo secondary dissociation. Nevertheless, the products from the ClO + NO_2 channel are still formed with internal energies small enough to preclude secondary dissociation. The fate of any NO_3 metastable photoproducts in the atmosphere will depend on the metastable lifetime versus the rate of collisional relaxation.

Previous calculations by Molina *et al.*[30] determined the stratospheric photodissociation rates of $ClONO_2$ at various altitudes. Their results show that above 35 km, photolysis occurs predominantly in the wavelength region 200-220 nm where the $ClONO_2$ cross-section is approximately 3×10^{-18} cm^2. Below 30 km, ozone starts to absorb the short-wave radiation so the dominant wavelength range for $ClONO_2$ photolysis shifts to 300-400 nm and the absorption cross-section decreases to $\sim 10^{-21}$ cm^2. Thus, the formation of metastable NO_3 photoproducts should be a concern only at higher altitudes in the stratosphere.

Our new branching ratios for the photolysis of chlorine nitrate are quite different from previously accepted values. These new results could significantly affect how current stratospheric models partition chlorine and nitrate species as well as the predicted rates of

ozone depletion. In order to determine the extent of these effects, we used a one-dimensional model of the stratospheric collar region surrounding the "ozone hole."

The new branching ratio had a minimal effect on the Cl and ClO concentrations since photolysis of $ClONO_2$ is a minor source for both species. The rates of formation for these two radicals are dominated by the reactions

$$ClO + NO \longrightarrow Cl + NO_2$$

$$Cl + O_3 \longrightarrow ClO + O_2$$

The production rates from these reactions are over an order of magnitude larger than those from the photodissociation of $ClONO_2$.

The new branching ratio does have an affect on the stratospheric concentrations of NO_3 and N_2O_5 since photolysis is one of the two major channels for the formation of NO_3.

$$NO_2 + O_3 \longrightarrow NO_3 + O_2$$

$$ClONO_2 + h\nu \longrightarrow Cl + NO_3.$$

If the yield of NO_3 from photolysis of $ClONO_2$ is reduced by almost 50%, the stratospheric concentration of NO_3 is decreased by approximately 15-20%. At lower altitudes, this loss of NO_3 is even more prevalent since the photolysis of $ClONO_2$ plays a larger role in NO_3 production there. The N_2O_5 concentration is strongly linked to the NO_3 concentration through the reaction

$$NO_2 + NO_3 + M \longrightarrow N_2O_5 + M.$$

Thus, any perturbation of the NO_3 concentration will be reproduced in the N_2O_5 concentration. The new branching ratio does not affect either the NO_2 or NO concentrations because the photolysis of $ClONO_2$ plays a minor role in NO_2 formation.

As for the rate of ozone loss, the new branching ratio has a negligible effect, since it affects neither the Cl nor NO concentration; the two species which dominate the catalytic cycles of stratospheric ozone degradation

$$NO + O_3 \longrightarrow NO_2 + O_2$$

$$Cl + O_3 \longrightarrow ClO + O_2.$$

Though the new branching ratios do not directly affect the predicted rates of ozone degradation, they do suggest that another mechanism important in stratospheric ozone loss could be flawed. The ClO dimer is implicated as a causal link in the catalytic cycle

$$ClO + ClO + M \longrightarrow ClOOCl + M$$

$$ClOOCl + h\nu \longrightarrow Cl + ClOO$$

$$ClOO + M \longrightarrow Cl + O_2 + M$$

$$2(Cl + O_3 \longrightarrow ClO + O_2)$$

$$\text{Net:} \qquad 2\,O_3 \longrightarrow 3\,O_2$$

responsible for approximately 70% of the ozone depletion in current polar models. The photochemical step in the pathway plays the pivotal role of releasing atomic chlorine from the ClO dimer. If ClOOCl dissociates to form ClO photoproducts a null cycle would result with no impact on ozone loss. The branching ratio of ClOOCl photolysis into Cl and ClO products is therefore critical in determining the effectiveness of the mechanism for destroying ozone. ClOOCl possesses an absorption band peaked at 245 nm and UV excitation of ClOOCl is currently believed to lead solely to the formation of Cl + OOCl. This channel requires that the stronger Cl–O bond break preferentially over the weaker peroxy bond. When first proposing the catalytic cycle Molina and Molina[14] rationalized the bond selective nature of ClOOCl photolysis by arguing that the UV absorption excites an $n \rightarrow \sigma^*$ transition localized on the ClO chromophore analogous to the results obtained from $ClONO_2$. In a flash photolysis experiment of ClOOCl, they found a Cl quantum yield of $\Phi_{Cl}=1.03$. These results are questionable since they used techniques similar to those employed in the $ClONO_2$ experiments which failed to detect ClO. Our observation that the two photodissociation channels have comparable yields at two distinct wavelengths

suggests that strong coupling exists among the excited state of $ClONO_2$ and that the photolysis of ClOOCl is likely to be equally complex. Any revision of the branching ratio in the photolysis of this key species will have a large impact on current models of stratospheric ozone depletion.

VI. REFERENCES

1. P.J. Crutzen, *J. Geophys. Res.* **76**, 7311 (1971).

2. H.S. Johnston, *Science* **173**, 517 (1971).

3. R. Stolarski, R.J. Cicerone, *Can. J. Chem.* **52**, 1610 (1974).

4. M.J. Molina, F.S. Rowland, *Nature* **249**, 810 (1974).

5. S.R. Kawa, D.W. Fahey, S. Solomon, W.H. Brune, M.H. Proffitt, D.W. Toohey, D.E. Anderson, L.C. Anderson, K.R. Chan, *J. Geophys. Res.* **95**, 18597 (1990).

6. Y. Yung, J.P. Pinto, R.T. Watson, S.P. Sander, *J. Atmos. Sci.* **37**, 339 (1980).

7. W.S. Smith, C.C. Chou, F.S. Rowland, *Geophys. Res. Lett.* **4**, 517 (1977).

8. S.M. Adler-Golden, J.R. Wiesenfeld, *Chem. Phys. Lett.* **82**, 281 (1981).

9. J.S. Chang, J.R. Barker, J.E. Davenport, D.M. Golden, *Chem. Phys. Lett.* **60**, 385 (1979).

10. W.J. Marinelli, H.S. Johnston, *Chem. Phys. Lett.* **93**, 127 (1982).

11. J.J. Margitan, *J. Phys. Chem.* **87**, 674 (1983).

12. H.D. Knauth, R.N. Schindler, *Z. Naturforsch* **38a**, 893 (1983).

13. J.P. Burrows, G.S. Tyndall, G.K. Moortgat, *J. Phys. Chem.* **92**, 4340 (1988).

14. L.T. Molina, M.J. Molina, *J. Phys. Chem.* **91**, 433 (1987).

15. Y.T. Lee, J.D. McDonald, P.R. LeBreton, D.R. Herschbach, *Rev. Sci. Instrum.* **40**, 1402 (1969).

16. M. Schmeisser, *Inorg. Synth.* **9**, 127 (1967).

17. D.J. Krajnovich, UC Berkeley, Ph.D. Thesis (1983).

18. R.B. Bernstein, *Chemical Dynamics Via Molecular Beam and Laser Techniques,* Oxford Univ. Press, New York (1982); 30.

19. R.N. Zare, *Mol. Photochem.* **4**, 1 (1972).

20. G.E. Busch, K.R. Wilson, *J. Chem. Phys.* **56**, 3638 (1972).

21. J.A. Coxon, D.A. Ramsey, *Can. J. Phys.* **54**, 1034 (1976).

22. H.F. Davis, personal communication.

23. R.D. Levine, R.B. Bernstein, *Molecular Reaction Dynamics and Chemical Reactivity,* Oxford Univ. Press, New York (1987); 37.

24. A.F. Tuck, *J. Chem. Soc., Faraday Trans. 2* **73**, 689 (1977).

25. C.S. Effenhauser, P. Felder, J.R. Huber, *J. Phys. Chem.* **94**, 296 (1990).

26. H.F. Davis, Y.T. Lee, (1992).

27. G.E. Busch, K.R. Wilson, *J. Chem. Phys.* **56**, 3626 (1972).

28. W.B. DeMore, S.P. Sander, D.M. Golden, R.F. Hampson, M.J. Kurylo, C.J. Howard, A.R. Ravishankara, C.E. Kolb, M.J. Molina, *Chemical Kinetics and Photochemical Data for Use in Stratospheric Modeling, Evaluation Number 10,* JPL Publication 92-10, JPL (1992).

29. M.J. Molina, A.J. Colussi, L.T. Molina, R.N. Schindler, T.L. Tso, *Chem. Phys. Lett.* **173**, 310 (1990).

30. L.T. Molina, M.J. Molina, *J. Photochem.* **11**, 139 (1979).

31. S.P. Sander, R.R. Friedl, *J.Phys. Chem.* **93**, 4764 (1989).

TABLE I: Photodissociation Results

Channel	Fraction	E_{avl}[a]	$\langle E_T \rangle / E_{avl}$	$E_T(\max)/E_{avl}$	Models Rigid	Soft	β
193 nm							
$ClO + NO_2$	0.36 ± 0.08	122	0.18	0.49	0.52	0.31	0.1-.04
$Cl + NO_3$	0.64 ± 0.08	108	0.40	0.85	0.69	0.49	0.5
248 nm							
$ClO + NO_2$	0.46 ± 0.08	89	0.25	0.52	0.52	0.31	1.1-1.4
$Cl + NO_3$	0.54 ± 0.08	75	0.54	0.81	0.69	0.49	0.5

[a] kcal/mol

VII. FIGURE CAPTIONS

Figure 1. UV absorption spectra of $ClONO_2$[30] and ClO[31] (——). In the $ClONO_2$ spectrum, the peak centered around 220 nm is attributed to the (Cl)$3P \rightarrow \sigma^*$ transition and the rise around 195 nm is assigned to the NO_2 $\pi \rightarrow \pi^*$ transition.

Figure 2. Schematic diagram of the Crossed Molecular Beams Apparatus adapted for a photodissociation experiment. The numbers correspond to pressures in Torr of the various regions.

Figure 3. Newton diagram representing the dissociation dynamics of chlorine nitrate at 248 nm. The fragment's velocity in the laboratory frame of reference is the sum of the molecular beam velocity v_b and the c.m. recoil velocity of the respective fragment $v_{Cl,\ ClO,\ ...}$ at the relevant laboratory angle of detection. The c.m. velocities for counterfragments for a specific channel are related through the conservation of linear momentum; $|v_{ClO}| = (m_{NO_2}/m_{ClO})|v_{NO_2}|$, $|v_{Cl}| = (m_{NO_3}/m_{Cl})|v_{NO_3}|$.

Figure 4. Laboratory TOF distributions of *m/e*=51 at 248 nm for four detector angles. Circles are experimental points and the solid lines are the calculated fits using the $P(E_T)$ for the ClO + NO_2 channel shown in the bottom panel of Figure 5.

Figure 5. $P(E_T)$s for the photodissociation of $ClONO_2$ at 248 nm. The bottom panel shows the $P(E_T)$ for the ClO + NO_2 channel calculated from the *m/e*=51 data, and the top panel displays the $P(E_T)$ for the Cl + NO_3 channel calculated from the *m/e*=35 data minus the contribution from the ClO + NO_2 channel. The inner line is derived form fitting the *m/e*=46 data. The shaded area shows the uncertainty in the fits of the slow tail in Figure 9.

Figure 6. Laboratory TOF distributions of *m/e*=51 recorded for two different molecular beam concentrations of $ClONO_2$. The slower peak is attributed to clusters in the molecular beam. The shift in arrival times is due to the variance in the molecular beam's velocity due to different beam compositions.

Figure 7. Laboratory TOF distributions of *m/e*=35 at 248 nm for five detector angles. The dashed lines represent the contributions from the two separate channels. The fast peak was fit using the $P(E_T)$ shown in the top panel of Figure 5. The slow signal at small angles resulting in a broad underlying signal at wider angles was fit assuming stimulated secondary dissociation of ClO.

Figure 8. Comparison of the *m/e*=35 TOF spectra detected at 10° using high and low laser powers.

Figure 9. Laboratory TOF distributions of *m/e*=46 and *m/e*=30 at 30°. The top panel displays the fits calculated using the $P(E_T)$s calculated for the $Cl + NO_3$ (——) and the $ClO + NO_2$ (------) channels from the *m/e*=51 and *m/e*=35 data. The experimental data was fit by trimming the $P(E_T)$ for the $Cl + NO_3$. The shaded area corresponds to uncertainty in the fit.

Figure 10. Laboratory TOF distributions of *m/e*=51 at 193 nm for five detector angles. The data was fit using the $P(E_T)$ shown in the bottom panel of Figure 12.

Figure 11. Laboratory TOF distributions of *m/e*=35 at 193 nm for five detector angles. $P(E_T)$s used to fit the data are shown in Figure 12.

Figure 12. $P(E_T)$s for the two channels at 193 nm. The shaded area in the top panel corresponds to the $P(E_T)$ used to fit the *m/e*=46 and *m/e*=30 data presented in Figure 13.

Figure 13. Laboratory TOF distributions of *m/e*=46 and *m/e*=30 at 193 nm. The fast sharp peak was fit using the truncated Cl + NO_3 $P(E_T)$ shown in Figure 12 and the slower broad peak was fit using the full $P(E_T)$ for the ClO + NO_2 channel.

Figure 14. Energy level diagram for the photodissociation of $ClONO_2$ at 248 nm. The $P(E_T)$ for the Cl + NO_3 channel is shown to illustrate how the available energy is partitioned.

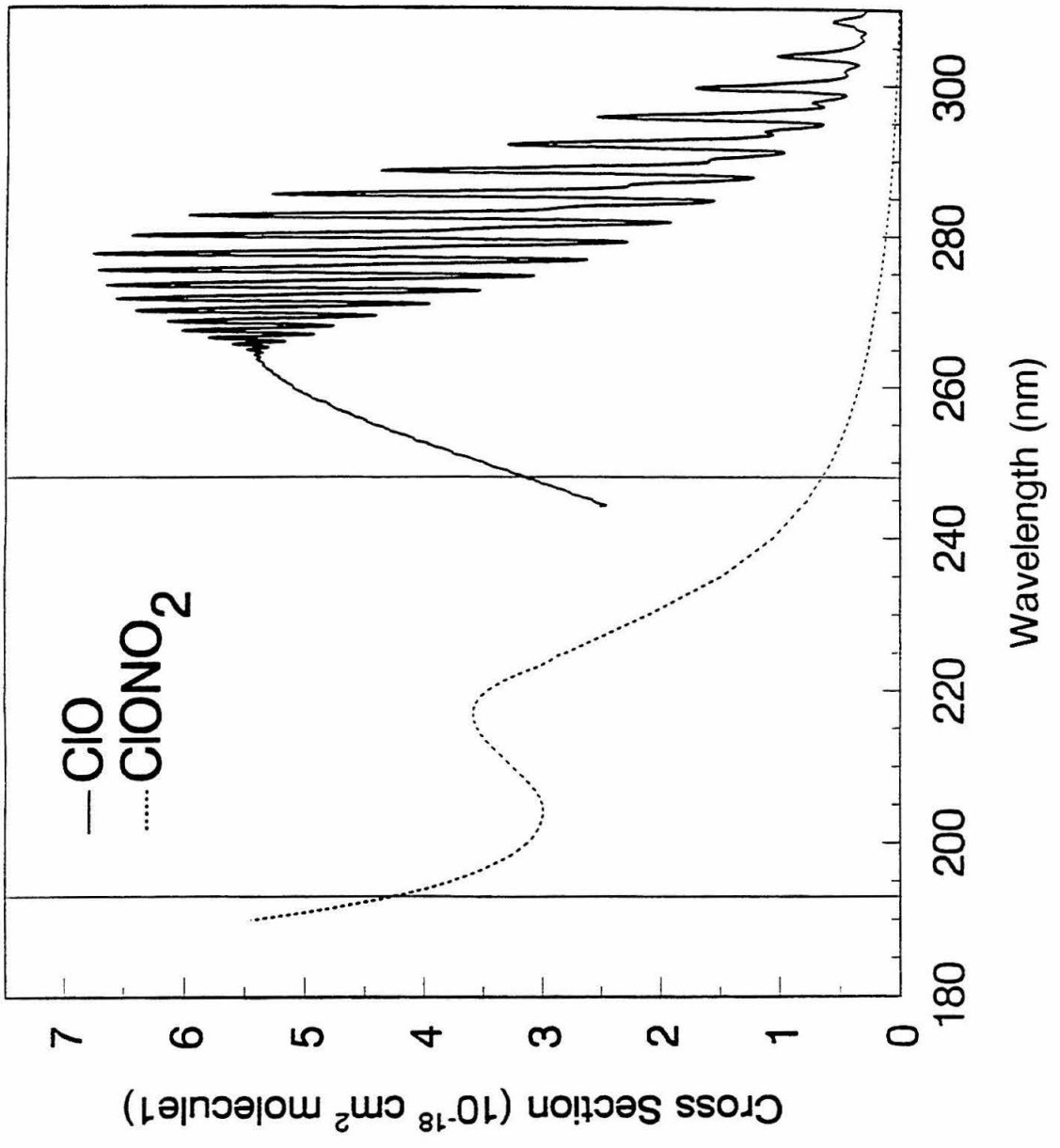
ClO
ClONO2
Cross Section (10-18 cm2 molecule-1)
Wavelength (nm)
0
1
2
3
4
5
6
7
180
200
220
240
260
280
300

Figure 1

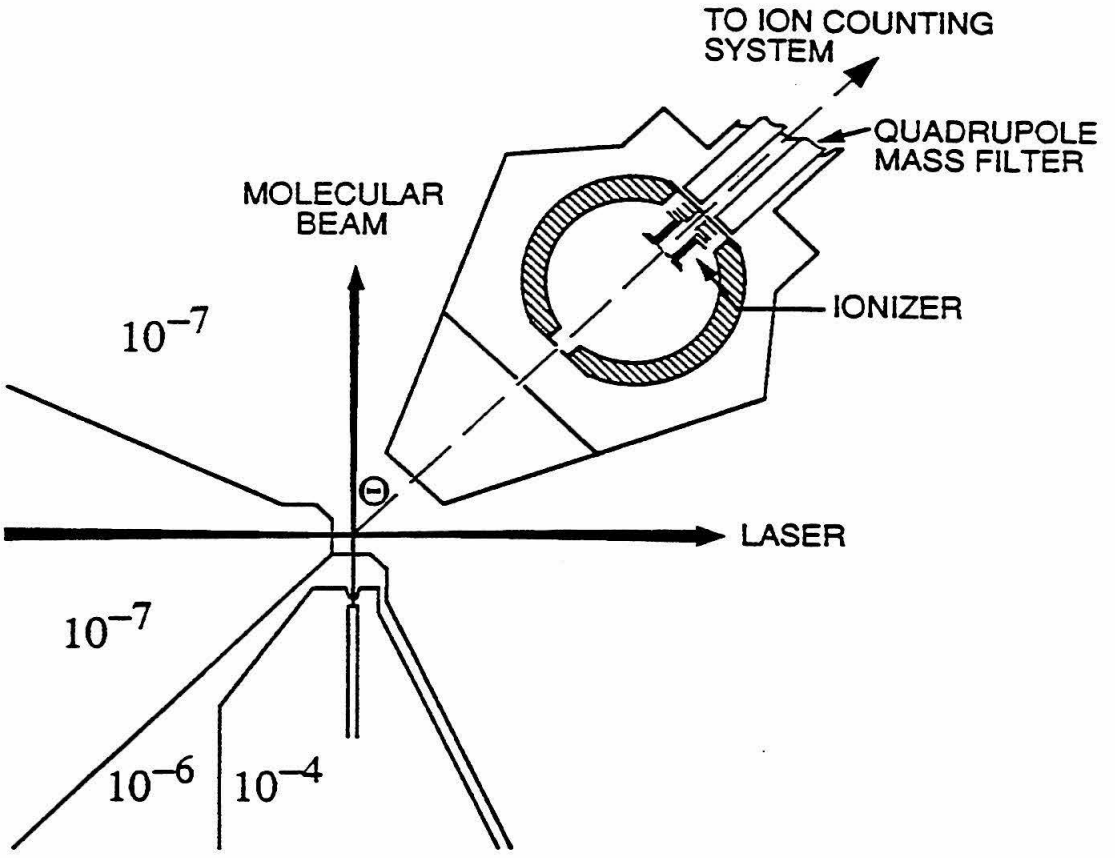
TO ION COUNTING SYSTEM
QUADRUPOLE MASS FILTER
MOLECULAR BEAM
IONIZER
10^{-7}
Θ
LASER
10^{-7}
10^{-6}
10^{-4}

Figure 2

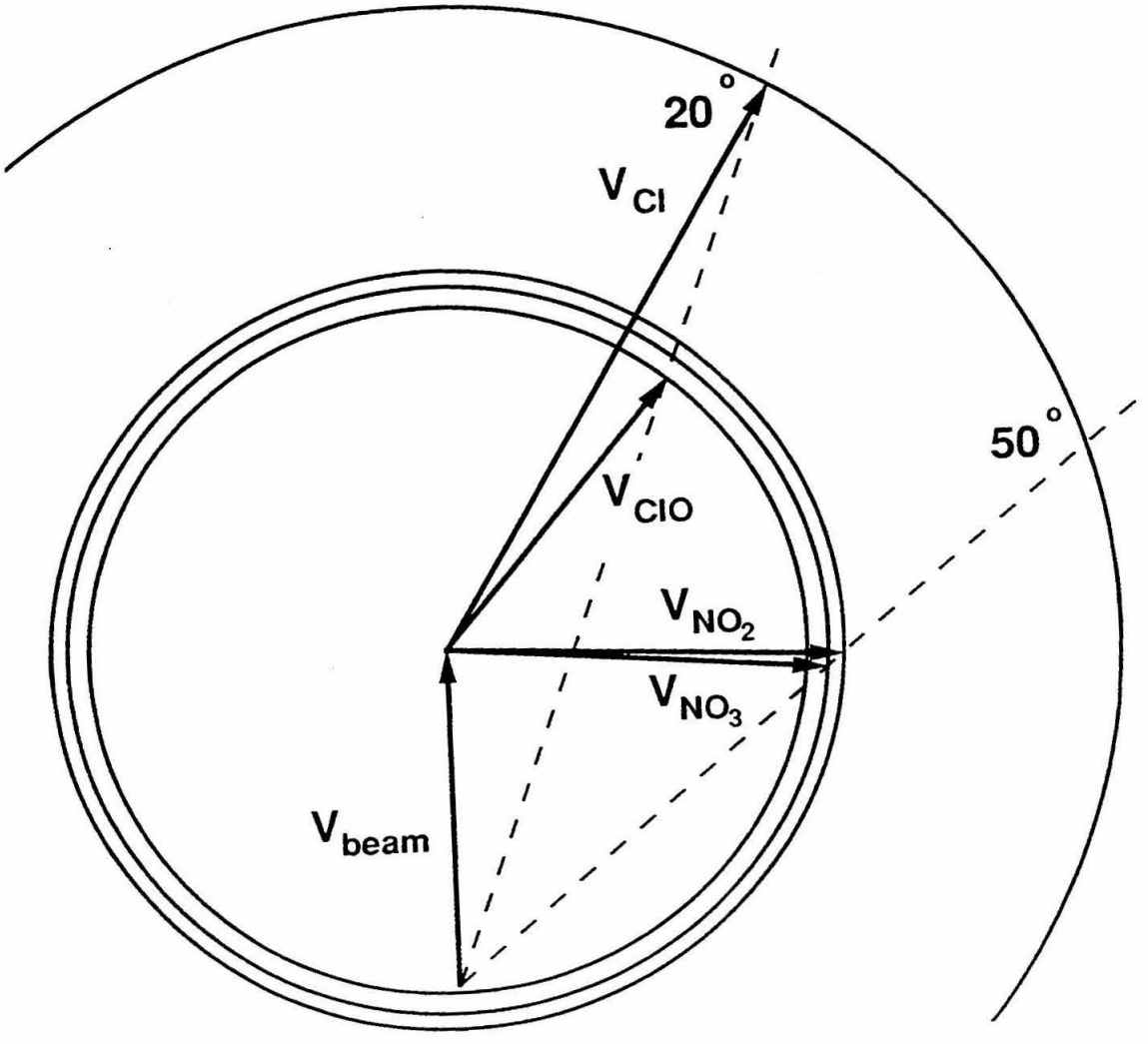

Figure 3

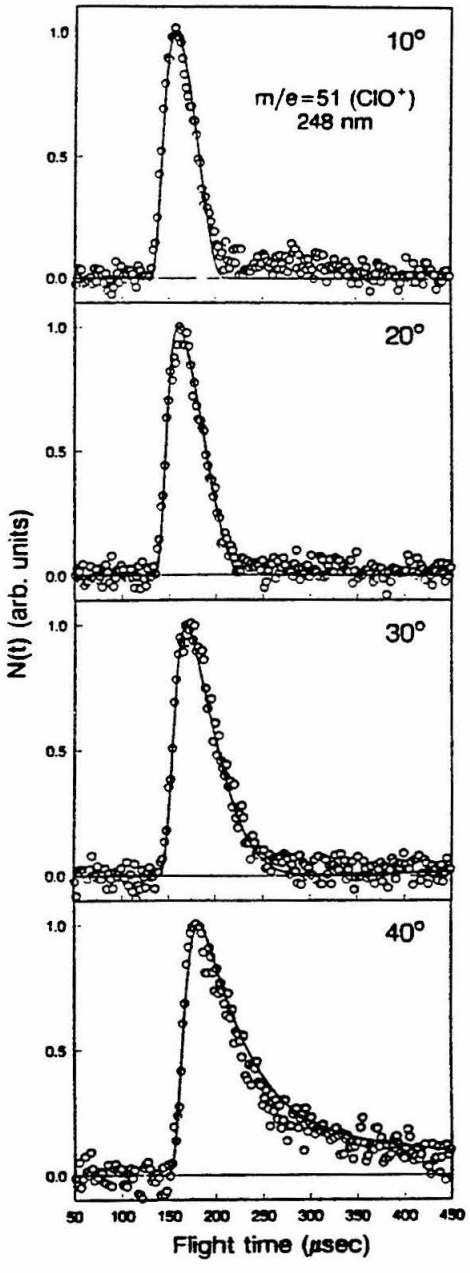
10°
m/e=51 (ClO+)
248 nm
20°
30°
40°
N(t) (arb. units)
Flight time (μsec)
1.0
0.5
0.0
50
100
150
200
250
300
350
400
450

Figure 4

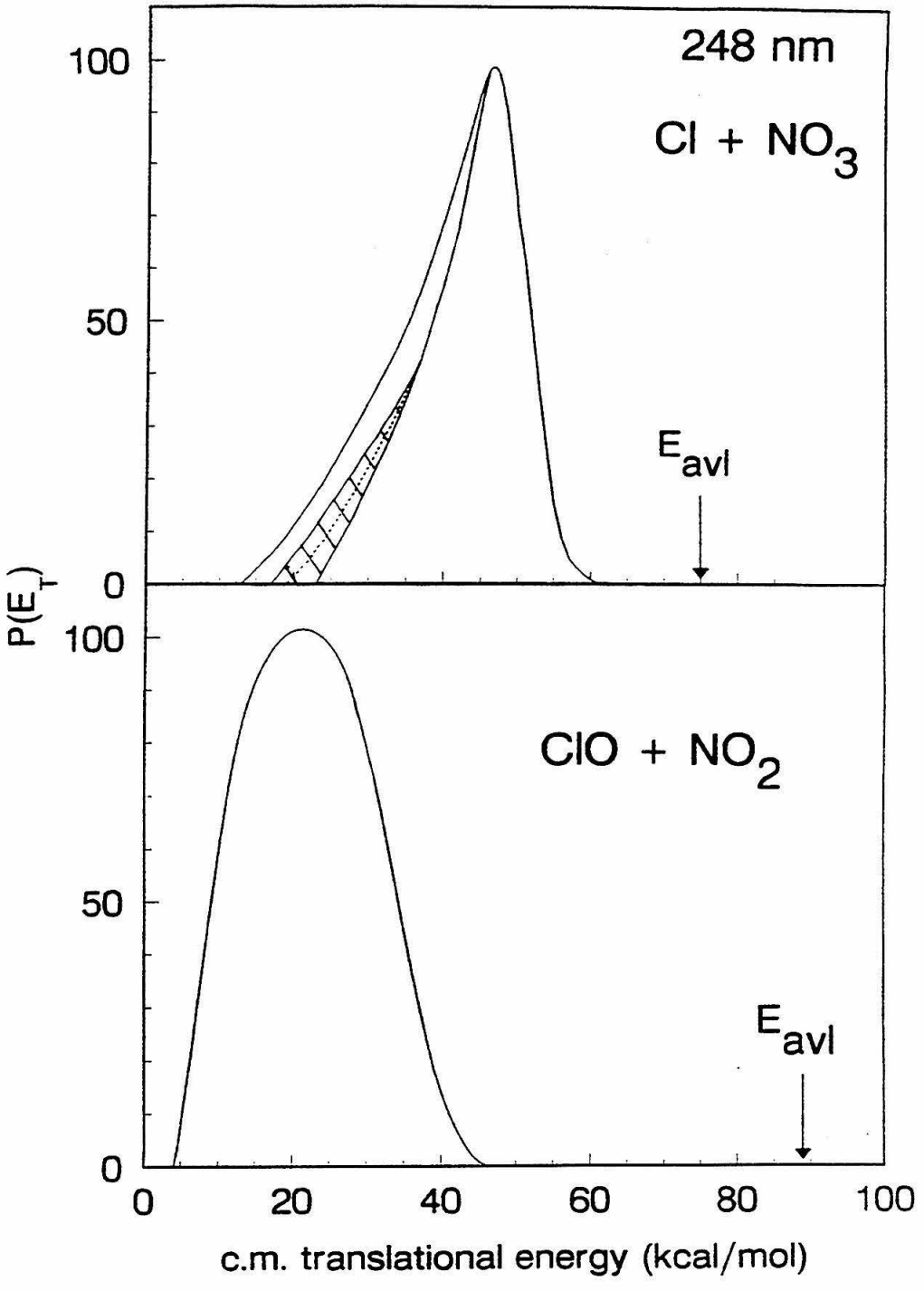
248 nm
Cl + NO3
Eavl
ClO + NO2
Eavl
P(ET)
100
50
0
100
50
0
0
20
40
60
80
100
c.m. translational energy (kcal/mol)

Figure 5

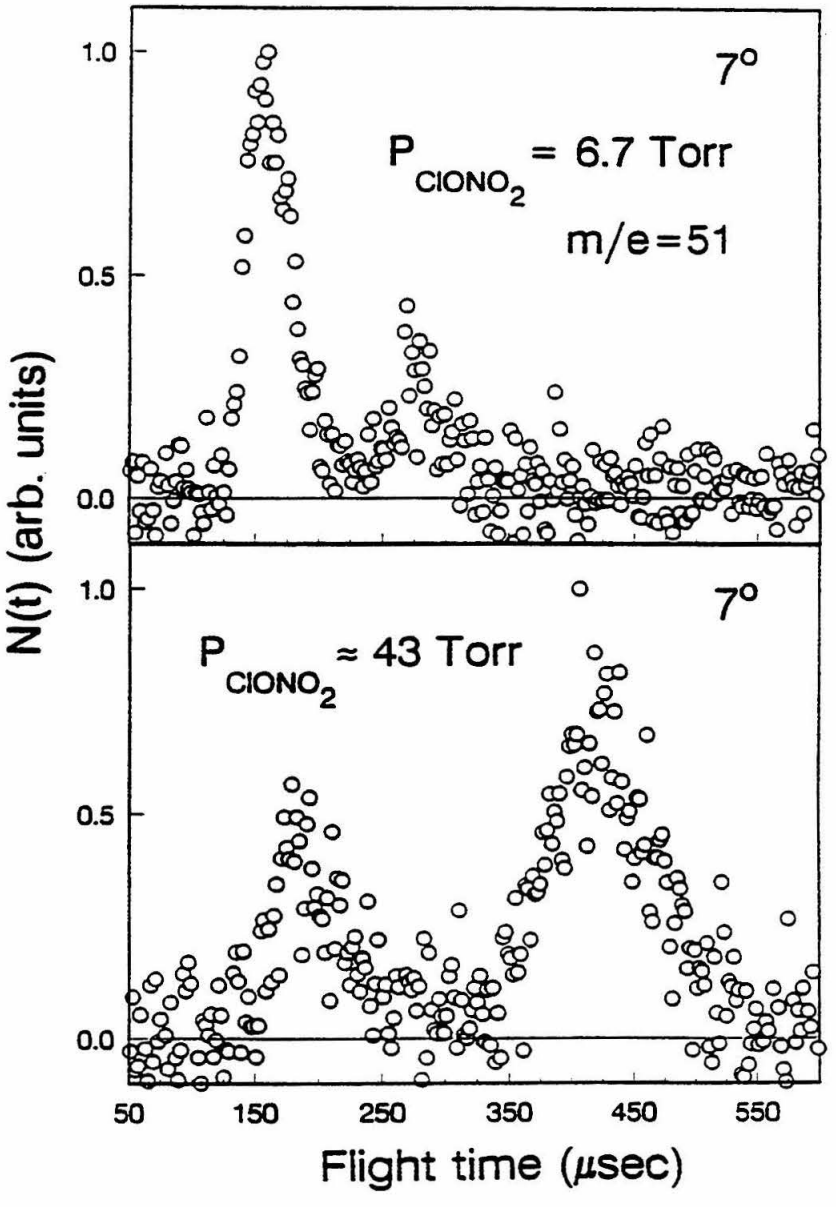
7°
P_{ClONO_2} = 6.7 Torr
m/e=51
7°
P_{ClONO_2} ≈ 43 Torr
N(t) (arb. units)
1.0
0.5
0.0
50
150
250
350
450
550
Flight time (μsec)

Figure 6

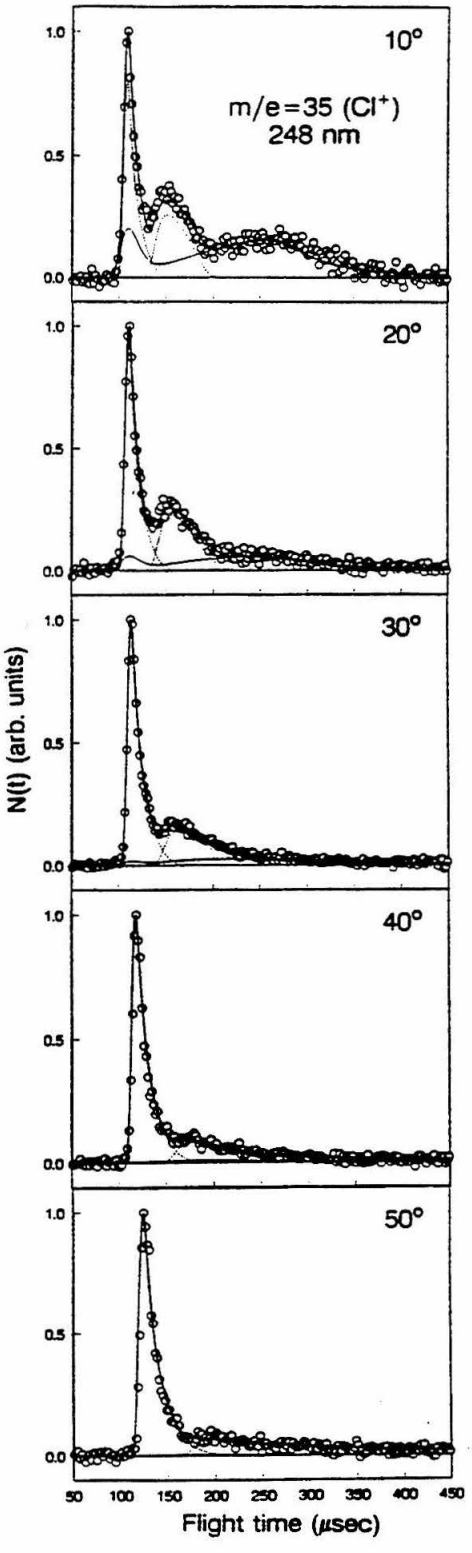
10°
m/e=35 (Cl+)
248 nm
20°
30°
40°
50°
N(t) (arb. units)
1.0
0.5
0.0
50
100
150
200
250
300
350
400
450
Flight time (μsec)

Figure 7

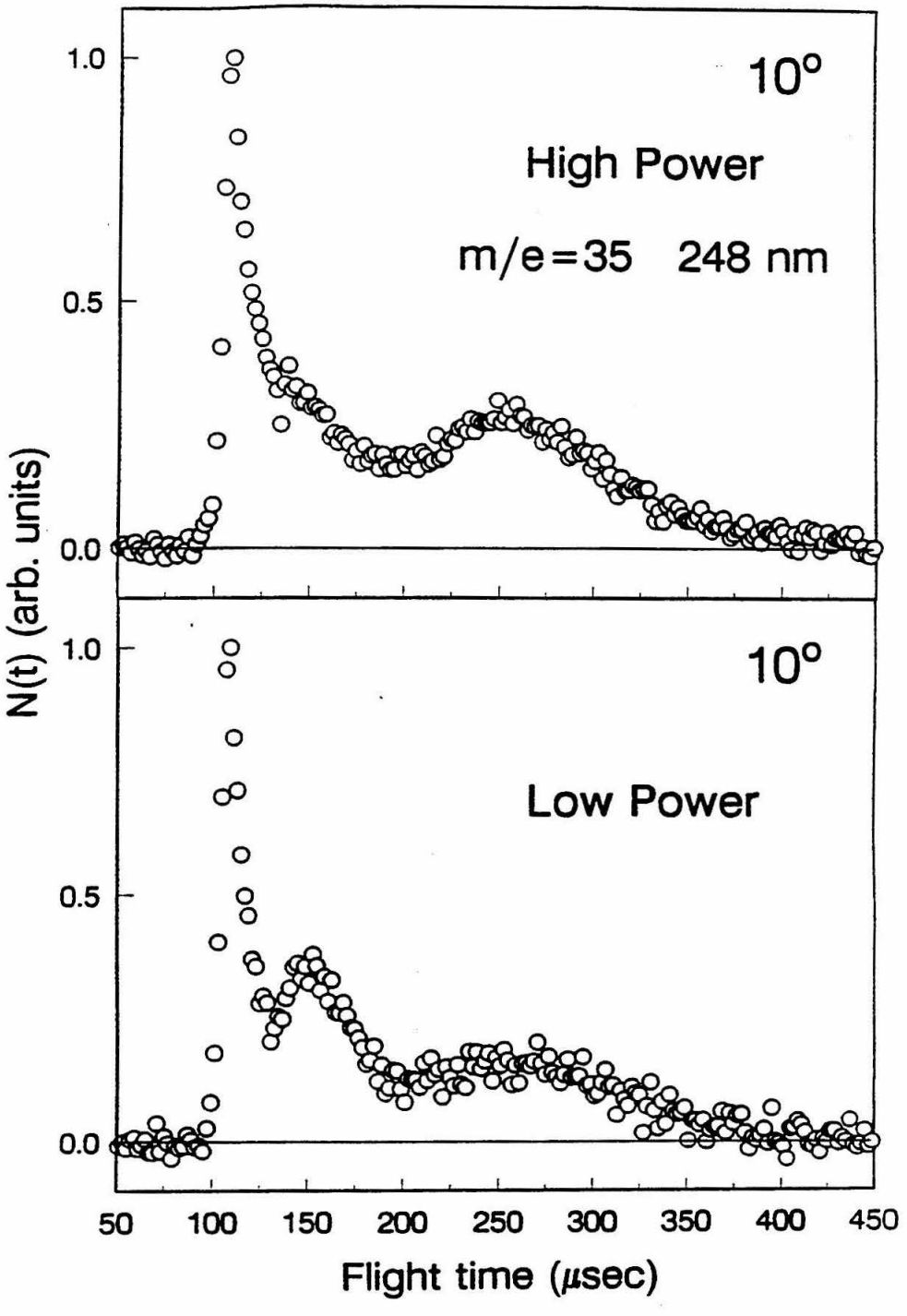
10°
High Power
m/e=35 248 nm
10°
Low Power
1.0
0.5
0.0
N(t) (arb. units)
50
100
150
200
250
300
350
400
450
Flight time (μsec)

Figure 8

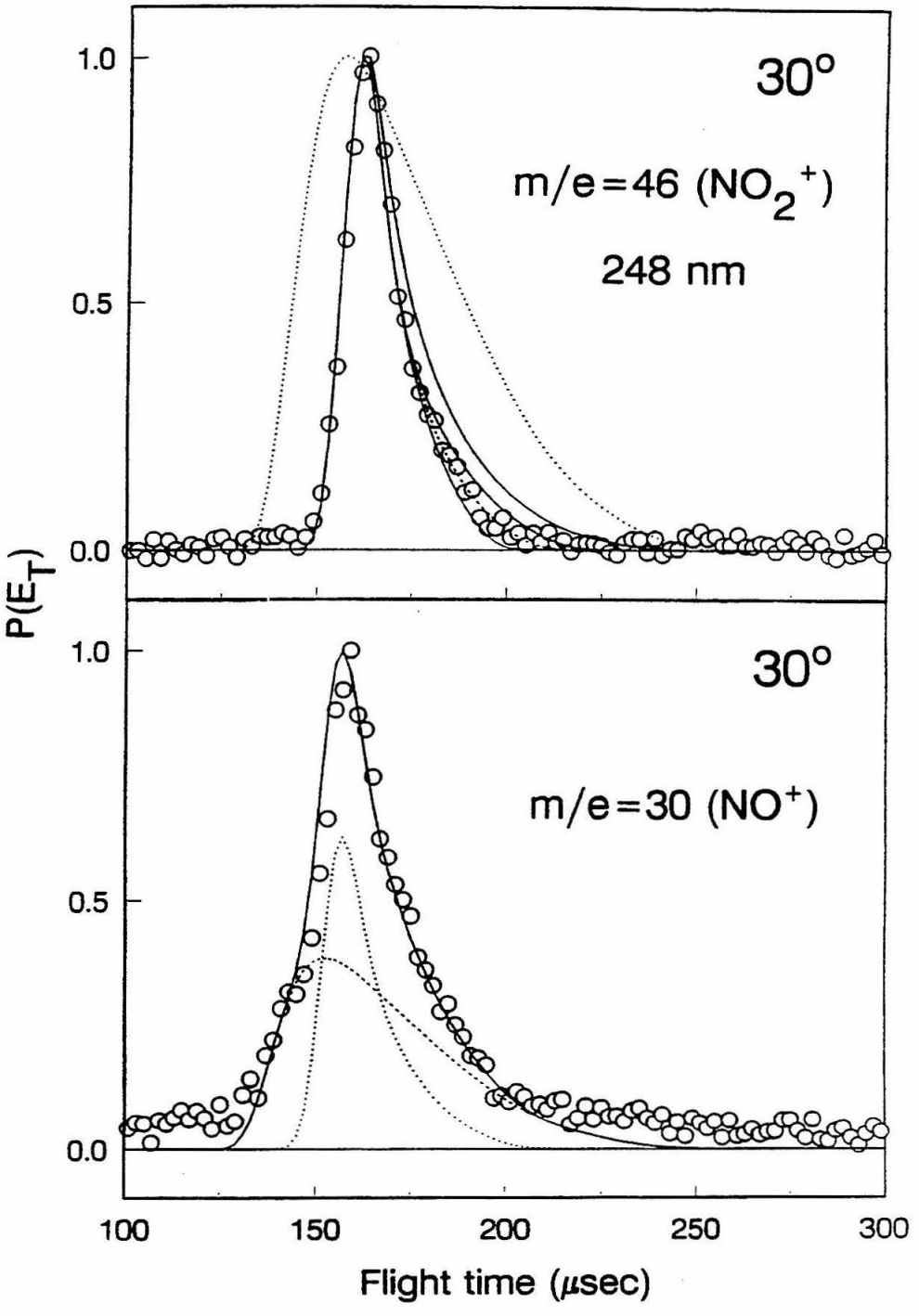
30°
m/e=46 (NO_2^+)
248 nm
30°
m/e=30 (NO^+)
1.0
0.5
0.0
$P(E_T)$
100
150
200
250
300
Flight time (μsec)

Figure 9

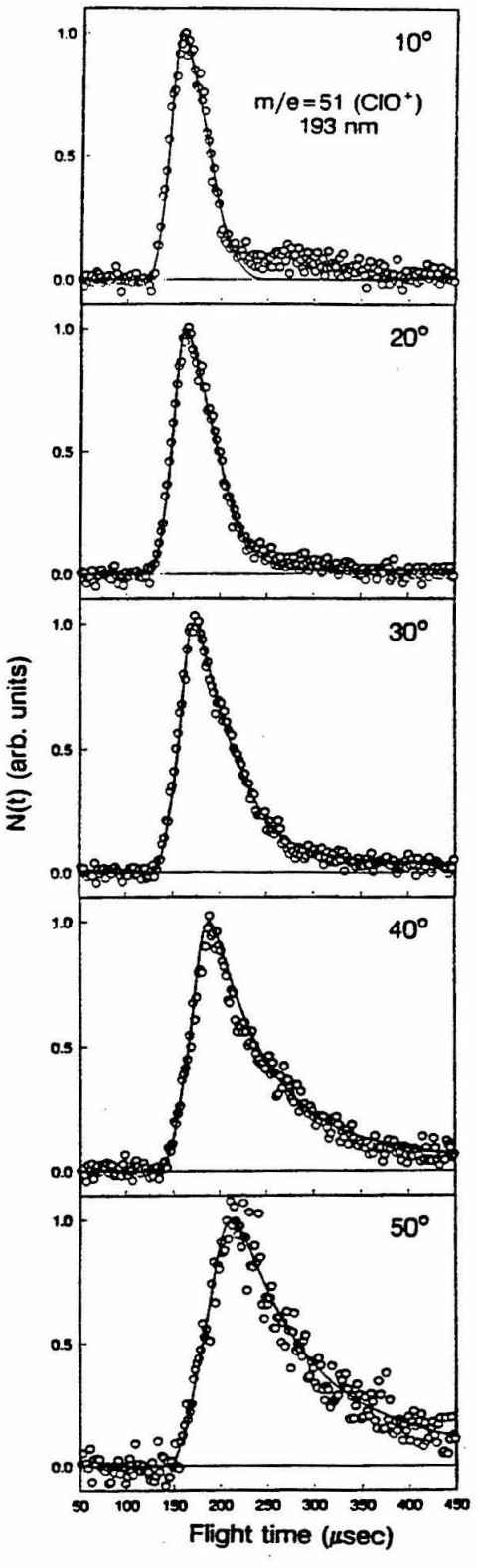
10°
m/e=51 (ClO+)
193 nm
20°
30°
40°
50°
N(t) (arb. units)
1.0
0.5
0.0
50
100
150
200
250
300
350
400
450
Flight time (μsec)

Figure 10

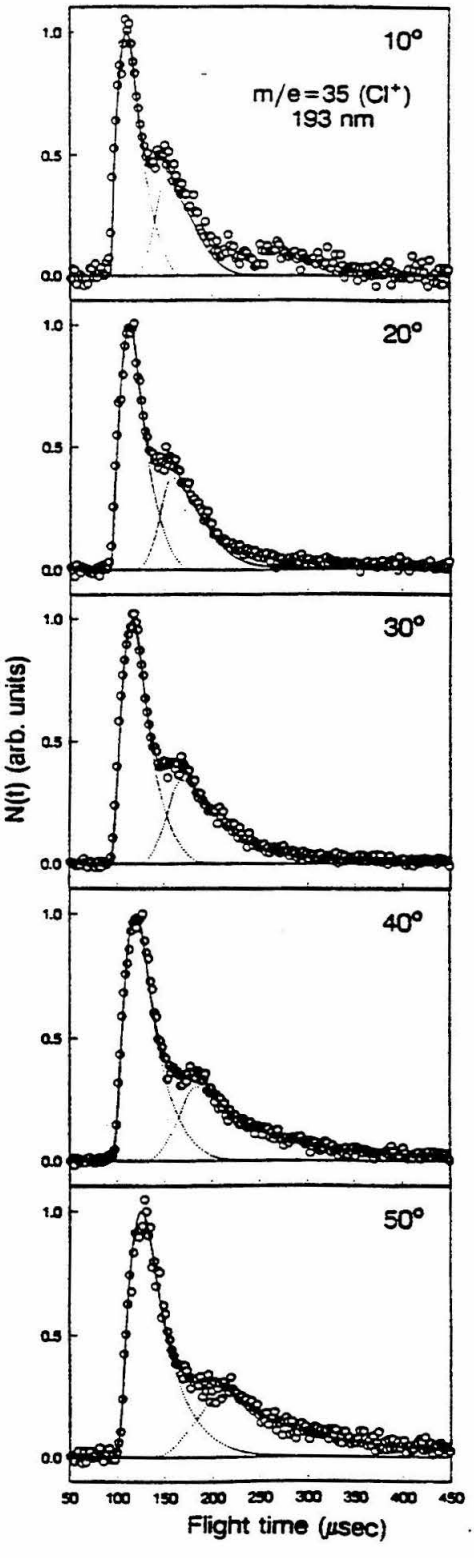

Figure 11

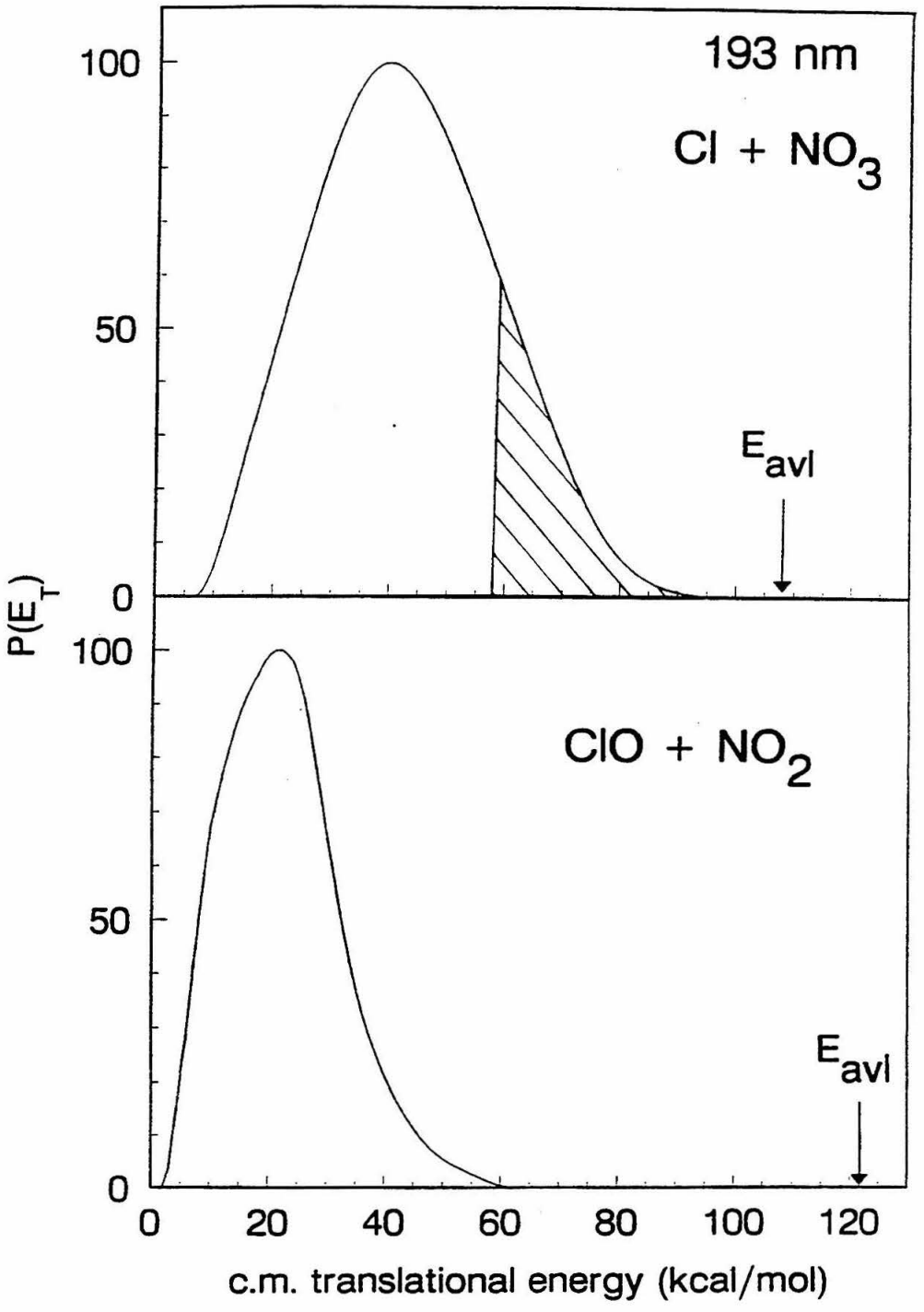
193 nm
Cl + NO3
Eavl
ClO + NO2
Eavl
P(ET)
100
50
0
100
50
0
0
20
40
60
80
100
120
c.m. translational energy (kcal/mol)

Figure 12

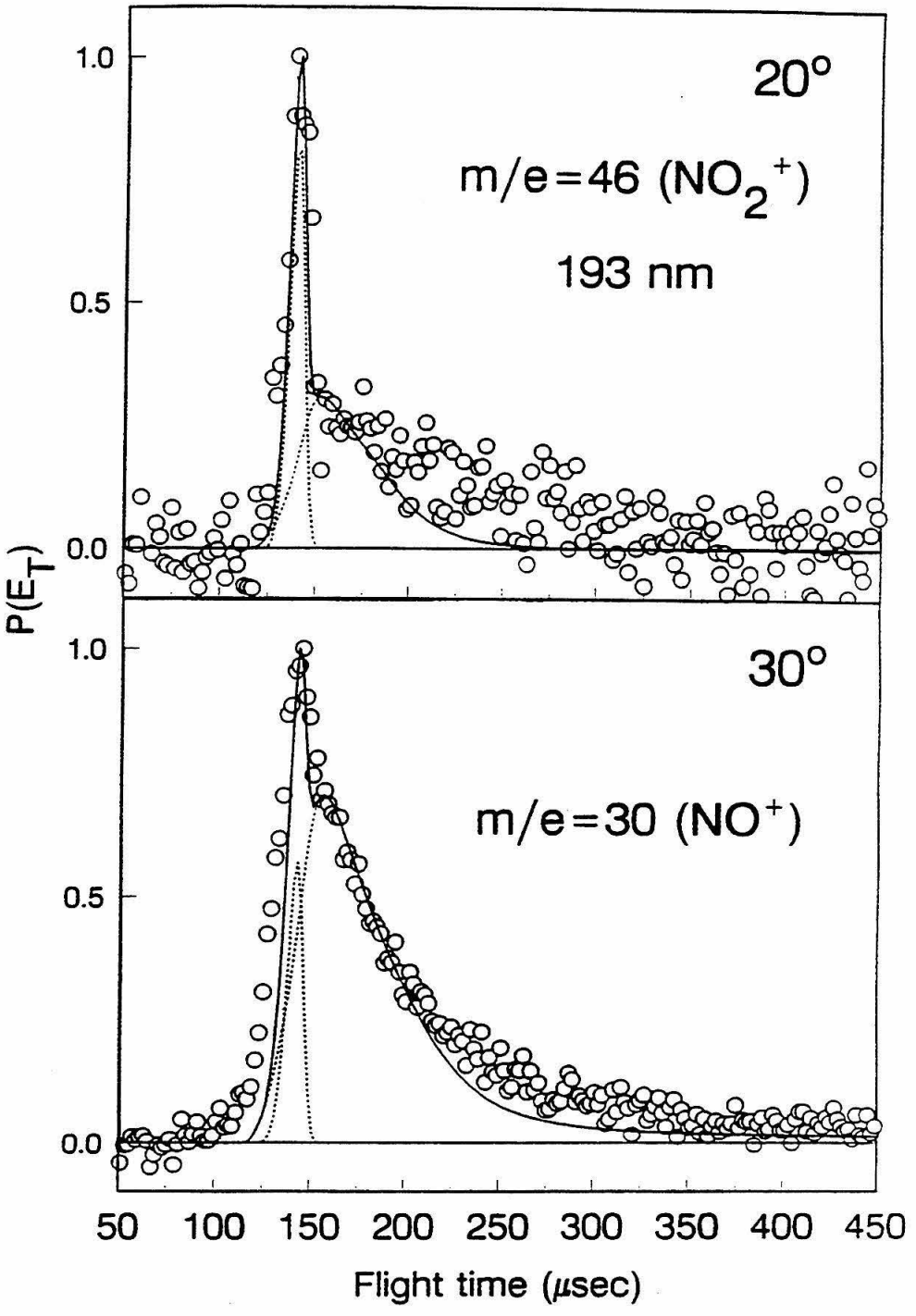
20°
m/e=46 (NO_2^+)
193 nm
30°
m/e=30 (NO^+)
1.0
0.5
0.0
$P(E_T)$
50
100
150
200
250
300
350
400
450
Flight time (μsec)

Figure 13

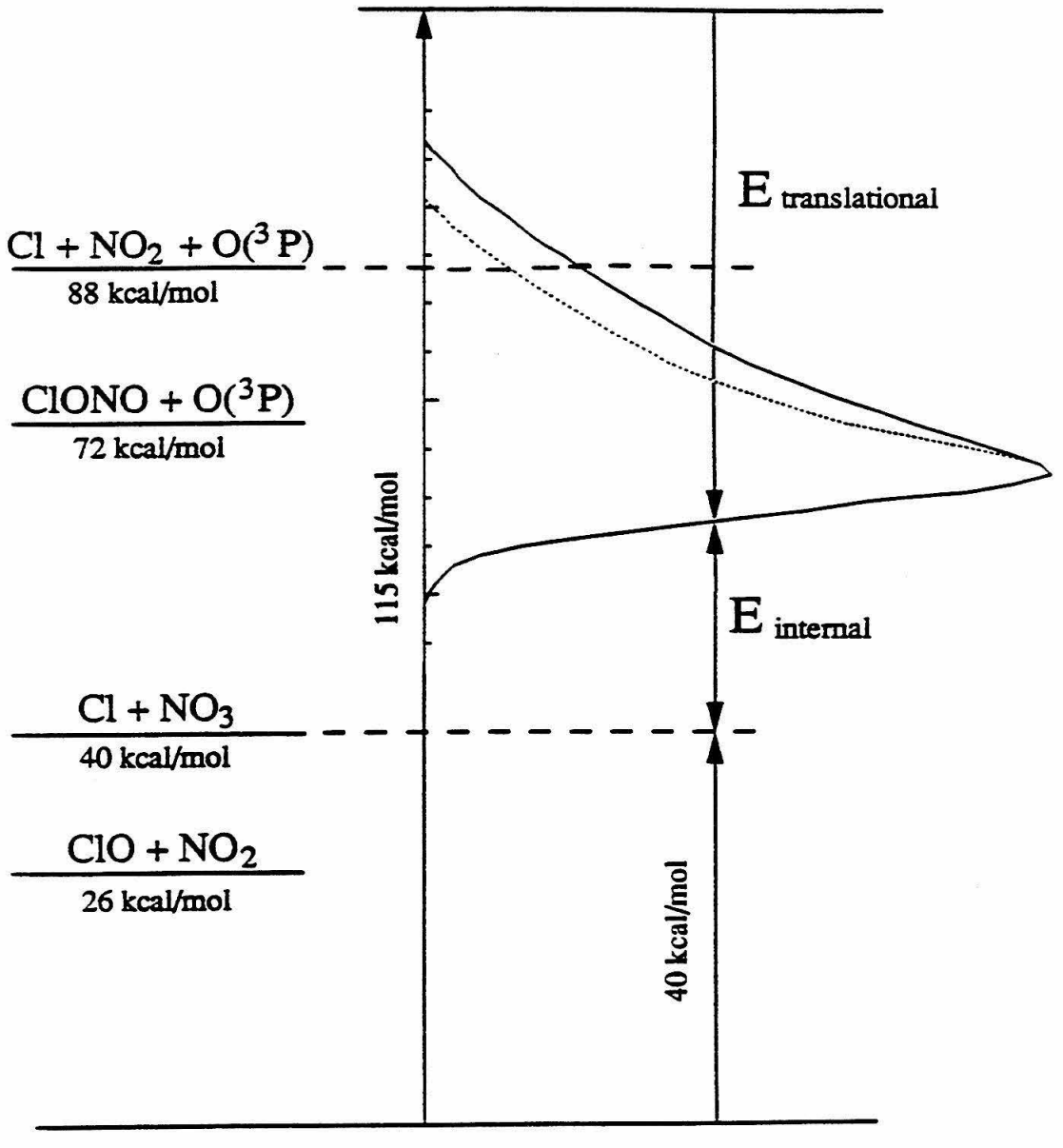
E translational
Cl + NO2 + O(3P)
88 kcal/mol
ClONO + O(3P)
72 kcal/mol
115 kcal/mol
E internal
Cl + NO3
40 kcal/mol
ClO + NO2
26 kcal/mol
40 kcal/mol

Figure 14

Chapter 3:

Photochemistry of Cl_2O at 193, 248 and 308 nm: Evidence of the Concerted Cl_2 + O Reaction

ABSTRACT

The photolytic properties of dichlorine monoxide (Cl_2O) were studied at 193, 248 and 308 nm using a molecular beam technique. At 193 nm, we observed the three-center elimination reaction channel, Cl_2 + O. This channel was confirmed by momentum matching the two product fragments. The ClO + Cl channel was also accessed, however, the majority of the ClO fragments were formed with sufficient internal energies to undergo spontaneous secondary dissociation. At 248 and 308 nm, we only observed the ClO + Cl channel. Some of the ClO formed at 248 nm, however, did have internal energies high enough for secondary dissociation to occur. Bimodal translational energy distributions for the ClO and Cl products indicate that two pathways lead to the same product.

I. INTRODUCTION

The discovery of chlorine catalyzed ozone degradation cycles in the stratosphere has spurred a large amount of interest in understanding the photolytic properties of chlorine containing species. Previous experiments studying the photolysis of dichlorine monoxide Cl_2O have focused primarily on solving the propagation mechanisms that occur after the molecule photodissociates in multicollisional environments. Finkelnberg *et al.*[1] investigated both the direct and chlorine-sensitized photochemical decomposition at 313, 365 and 436 nm and deduced that

$$Cl_2O + h\nu \longrightarrow ClO + Cl \qquad (1)$$

was the initial degradation step. Schumacher and Townend[2] later carried out the same experiment with radiation between 235 and 275 nm. They observed an increase in the quantum yield of atomic oxygen from 3.5 to 4.5 at the shorter wavelengths which they explained by activating a second initiation step

$$Cl_2O + h\nu \longrightarrow 2Cl + O. \qquad (2)$$

Their propagation mechanism predicted that this pathway was the only degradation channel and lead them to conclude that oxygen atoms do not react with Cl_2O. Subsequent experiments, however, have shown elsewise; the reaction between atomic oxygen and dichlorine monoxide

$$O + Cl_2O \longrightarrow 2ClO \qquad (3)$$

is in fact very fast. Edgecomb *et al.*[3] reinterpreted Schumacher and Townend's results in light of this fact and suggested that the observed increase in the chlorine quantum yield at shorter wavelengths was due to a limited occurrence of reaction 2 followed by reaction 3.

Basco and Dogra later flash-photolyzed Cl_2O with and without added Cl_2 and found an average quantum yield of 4.9 ± 1.0 for both cases.[4] They also observed the formation of vibrationally excited oxygen O_2^* when Cl_2O was photolyzed at shorter wavelengths ($\lambda < 310$ nm). Since none of the reactions following the primary process

$Cl_2O \rightarrow ClO + Cl$ can lead to O_2^* production, they concluded that at least one of the following reactions must be occurring

$$Cl_2O + h\nu \longrightarrow 2Cl + O \qquad (2)$$

$$\longrightarrow Cl_2 + O \qquad (4)$$

$$ClO + h\nu \longrightarrow Cl + O \qquad (5)$$

which can access two reactions that produce O_2^*,

$$O + Cl_2O \longrightarrow 2Cl + O_2^* \qquad (6)$$

$$O + ClO \longrightarrow Cl + O_2^*. \qquad (7)$$

Sander *et al.*[5] recently investigated the photolytic pathways of Cl_2O in conjunction with a study of the BrO + ClO reaction. In their experiment, Cl_2O was photolyzed in the presence of Br_2 using a broad-band light source (180 nm $\leq \lambda$) and saw the formation of BrO. The only known source of BrO is

$$O + Br_2 \longrightarrow BrO + Br \qquad (8)$$

which lead them to conclude that atomic oxygen must be formed directly from Cl_2O photolysis by either reaction 2 or 4. They derived a quantum yield of 0.25 ± 0.05 for the production of atomic oxygen but were unable to determine the relative importance of the two channels.

These previous experiments indicate that the dissociation dynamics of Cl_2O are highly dependent on the excitation wavelength. The absorption spectrum of Cl_2O lends credence to this observation (see Figure 1).[6] In the 185 to 360 nm region, at least three different transitions are apparent. The band peaked at 256 nm has been attributed to the $^1B_2$ state.[7] A shoulder on the lower energy side of this peak indicates the presence of a second state. At wavelengths shorter than 220 nm, a third band appears which peaks around 171 nm.[8]

We photolyzed Cl_2O at three wavelengths, 193, 248 and 308 nm, which were each localized on a different transition. Of interest was the variance in the dissociation

dynamics of these excited states. At 308 nm, only the ClO + Cl and Cl_2 +O(^3P) channels are energetically accessible (see Figure 2). However, at 193 and 248 nm, the 2Cl + O(^3P) channel also becomes available.

Using the technique of photofragmentation translational energy spectroscopy, we were able to discern not only what channels are accessed at each wavelength but also how the excess energy was partitioned in the photoproducts. We demonstrated that the three-center elimination reaction Cl_2 + O was indeed accessed at shorter wavelengths. However, a significant amount of the Cl_2 was formed with internal energies greater than the Cl-Cl bond strength and thus dissociated and contributed to the 2Cl + O channel. At the longer wavelengths, the only observed primary channel was ClO + Cl. At 248 nm, though, some of the ClO was formed with internal energies sufficiently large for spontaneous secondary dissociation to occur.

II. EXPERIMENTAL

The experimental apparatus and technique are described in detail in previous papers so only a brief outline is presented here.[9,10] A continuous molecular beam of Cl_2O was formed by flowing helium over liquid Cl_2O (-74°C; vapor pressure = 6.9 torr) to a total stagnation pressure of 200 torr and expanding the mixture through a 0.1 mm diameter water-cooled glass nozzle (4.9°C). A skimmer then confined the beam to an angular divergence of 3.4°. A rectangular slit aperture further defined the beam to a 2.3 mm x 3.0 mm spot in the interaction region. The molecular beam traveled a total of 4.8 cm from the nozzle to the interaction region where it intersected a pulsed excimer laser beam.

Laser power dependence measurements were taken to determine the optimum conditions for recording TOF spectra. Laser powers were attenuated using quartz slides, and power levels were chosen which corresponded to sufficient signal with the minimum amount of stimulated secondary dissociation of the ClO product. Excitation wavelengths

were 193, 248 and 308 nm and had pulse energies of 13-25 mJ, 48-60 mJ and 9-22 mJ and spot sizes of 2.3 x 3.5, 4.7 x 2.4 and 3.3 x 1.4 mm, respectively. At 193 nm, pump oil on the optics rapidly photolyzed to form a film which could reduce the pulse energy in the interaction region by as much as 75%.

The resultant photoproducts scattered out of the interaction region and were detected off-axis with an in-plane mass spectrometer. The distance from the interaction region to the ionizer of the mass spectrometer was 34.1 cm. Time-of-flight (TOF) spectra of the photoproducts were recorded with a multichannel scaler set at 2 μs dwell time.

Cl_2O was synthesized using techniques present in the literature.[11] The main impurity, Cl_2, was removed by pumping on the sample at .118°C (ethanol slush bath). Excess chlorine was further removed by pumping on the sample until the molecular beam stabilized.

At all wavelengths, TOF spectra were recorded at m/e=35 (Cl^+), 51 (ClO^+), 70 (Cl_2^+) and 16 (O^+) and at detector angles raging from 10° to 60° with each spectrum averaged over 100,000 to 500,000 laser pulses. The correction for the flight time of ions from the ionizer to the detector was determined to be $3.54(m/e)^{1/2}$ μs.

At 248 and 308 nm, angular distributions were recorded at m/e=51 over the range 10° to 50°. The 248 nm distribution was made in 10° increments with four scans of 10,000 laser pulses each for a total of 40,000 laser pulses at each angle. The 308 nm distribution was recorded in 5° increments with 6 scans for a total of 60,000 laser pulses at each angle.

At 193 nm, an angular distribution was taken at m/e=16 over the range 10° to 60°. At each angle, two scans were recorded for a total of 20,000 scans.

III. RESULTS

248 and 308 nm

The *m/e*=51 (ClO^+) TOF spectra recorded at 308 nm for various angles are shown in Figure 3. We observed a sharp peak with a slow tail which we assigned to ClO recoiling from Cl (reaction 1). The $P(E_T)$ used to fit the spectra with β=0.5 is displayed in Figure 4. To confirm our assignment of the channel, we used this $P(E_T)$ and β to fit the counterfragment Cl. In the *m/e*=35 TOF spectra that are shown in Figure 5, two peaks are apparent. The slower peak is identical to the *m/e*=51 peak, with a small correction for the difference between the *m/e*=35 and *m/e*=51 ion flight times. Thus, this slower peak is attributed to ClO cracking in the ionizer to form Cl^+. The faster, sharper peak was assigned to the Cl counterfragment. Since the Cl is formed in the same dissociation event as the ClO, the $P(E_T)$ and β obtained from the *m/e*=51 spectra should also fit the fast peak.

The results at 248 nm were analogous to those obtained at 308 nm and were analyzed using the same approach. Again, a $P(E_T)$ and β were obtained by fitting the *m/e*=51 data which was then used to fit the *m/e*=35 data (see Figure 6). However, at 248 nm, we could not obtain an accurate fit for the *m/e*=35 spectra because some of the ClO was formed with sufficient internal energies to undergo spontaneous secondary dissociation. This is evident when one examines the $P(E_T)$ obtained from the *m/e*=51 data (see Figure 7). The total available energy is 84 kcal/mol. Conservation of energy mandates that this must be partitioned between internal energy in the ClO fragment and translational energy. For products with translational energies less than 20 kcal/mol, the internal energy in the ClO fragment will exceed the Cl-O bond dissociation ($D°_0$ = 63.4 kcal/mol) and the ClO fragment will spontaneously dissociate. However, the $P(E_T)$ truncates at 16 kcal/mol; 4 kcal/mol lower than predicted. Uncertainty in the fit and heats of reaction could account for 2 kcal/mol difference which leaves 2 kcal/mol unexplained.

At both 248 and 308 nm, we found no evidence to support the existence of the Cl_2 + $O(^3P)$ channel.

193 nm

The TOF spectra and best fits at various angles of the *m/e*=16 data are shown in Figure 8. We observed a prominent peak arriving at fast times which we attribute to O atoms arising from the concerted reaction, $Cl_2O \rightarrow Cl_2 + O(^3P)$. The solid lines represent the fits which were obtained using the center-of-mass (c.m.) translational energy distribution $P(E_T)$ shown in Figure 9 with an anisotropy parameter of $\beta = 0.4$. The total energy available for translation for the channel was determined using the expression $h\nu$ - $\Delta H°_0(Cl_2O \rightarrow Cl_2 + O(^3P))$=148 - 39.2 =109 kcal/mol.[12,13] The signal observed at longer times in the 20° spectrum could be due to a variety of sources; secondary dissociation of the ClO fragments (see below), clusters in the beam, higher order chlorine oxides or possibly the $Cl_2 + O(^1D)$ channel.

To confirm the channel assignment, we momentum matched the oxygen atom to its counterfragment, Cl_2. In the c.m. frame of reference, both fragments from a two body primary dissociation channel will recoil with equal and opposite momenta, and therefore both will be described by the same c.m. translational energy distribution $P(E_T)$ and angular distribution. Thus, the TOF distribution for the Cl_2 counterfragment should be completely determined from the $P(E_T)$ and β obtained from fitting the oxygen signal at *m/e*=16 (see Figure 10). The dashed line shows the fit obtained using the full $P(E_T)$ and does not predict an acceptable fit. Note though that conservation of energy mandates that excess energy which is not partitioned into translation must remain in the photofragments as internal energy (see Figure 11). If the $P(E_T)$ is truncated at translational energies which correspond to internal energies in the Cl_2 fragment which are greater than the dissociation energy of Cl_2 ($D°_0$ = 57.2 kcal/mol), the fit is greatly improved (solid line). The *m/e*=70

signal which we observed at slower times is most likely due to clusters in the beam or higher order chlorine oxides. Albeit, if some of the atomic oxygen is formed in the spin-orbit excited ^1D state then the corresponding Cl_2 would be formed sufficiently cold to survive at these lower translational energies.

As for the ClO + Cl channel, the *m/e*=35 and *m/e*=51 TOF spectra recorded at 40° are shown in Figure 12. At *m/e*=51, a low intensity peak with an arrival time of 150 μs was apparent. Energetically, however, any ClO fragments which are formed with translational energies that correspond to arrival times greater than 152 μs, will have internal energies greater than the dissociation energy of the Cl-O bond ($D°_0$ = 63.4 kcal/mol). Thus, the majority of the ClO formed initially undergoes spontaneous secondary dissociation before reaching the detector and only a sliver of the primary ClO product survives.

At *m/e*=35, the signal is much stronger and appears to be a group of peaks super-imposed over each other. The sources of these peaks include Cl_2 and ClO cracking in the ionizer to form Cl^+, neutral Cl formed in the Cl + ClO channel and any products from the spontaneous secondary dissociation of ClO or Cl_2. This complexity prevents any attempt to fit the data.

IV. DISCUSSION

248 and 308 nm

A possible explanation for the unexplained 2 kcal/mol difference at the truncation point is that the Cl or ClO photofragment is formed in a spin-orbit excited state. This would decrease the total available energy which in turn would lower the truncation point. The spin-orbit splitting for Cl is 2 kcal/mol which would accurately explain the disagreement. ClO's spin-orbit splitting though is only 1 kcal/mol which leaves 1 kcal/mol unexplained. However, ClO with translational energies near the truncation point would be

vibrationally hot which could cause the of spin-orbit splitting to increase and thus could account for the 2 kcal/mol difference. An alternative explanation is a centrifugal barrier on the exit channel of the Cl-O dissociation potential. Using a model analogous to that presented in Appendix B, we predicted a centrifugal barrier of 6.8 kcal/mol from the rigid radical model and ground state geometry of Cl_2O. Though this is much larger that the unexplained 2 kcal/mol, it does show that enough rotational energy can be imparted to the ClO fragment to create a centrifugal barrier.

Our results at 248 and 308 nm are consistent with results from previous photolysis experiments. Finkelnberg *et al.* measured a chlorine quantum yield form the photolysis of Cl_2O at 313, 365 and 436 nm of $\Phi_{Cl} = 3.5$. Schumacher and Townend observed that the quantum yield increased to 4.5 when radiation between 235-275 nm was used. They attributed the increase in Cl formation to the process

$$Cl_2O + h\nu \longrightarrow 2Cl + O(^3P) \qquad (2)$$

being accessed at the shorter wavelengths.

Our results show that at 308 nm, the only photolytic pathway is ClO + Cl as Finkelnberg *et al.* observed and that at shorter wavelengths secondary dissociation of the ClO fragment becomes important. At 248 nm, which is in the wavelength range of Schumacher and Townend's experiment, we observed that the $2Cl + O(^3P)$ is accessed but not with 100% yield as they had concluded. Rather, we see that a significant amount of the ClO fragments are formed with translational energies large enough for the ClO fragment to survive. This supports Edgecomb's *et al.* interpretation of Schumacher and Townend's results which state that both ClO + Cl and 2Cl + O are the initiation steps in the 235-275 nm experiment.

An anomalous feature in our results is the bimodal distribution in the $P(E_T)$ for the ClO + Cl channel at both 248 and 308 nm. The occurrence of which could be caused by a variety sources. The first is simply that two different states of Cl_2O are excited, both of

which lead to ClO + Cl formation. This is consistent with the absorption spectrum of Cl_2O. The irregular shape of the 220 and 380 nm region alludes to the presence of at least two different electronic states. Recent theoretical calculations predict two states in the region, a $^1B_2$ state around 284 nm and a $^3A_1$ state around 287 nm.

A second possibility is that a single electronic state of Cl_2O is initially prepared. As the system evolves, some of the molecules may undergo a curve crossing to a second potential energy surface. Again both surfaces must lead to ClO and Cl formation but may partition the available energy differently. In both cases, different excited state must still lead to ClO + Cl products, but may correlate to different spin-orbit states of either Cl or ClO. Our resolution precludes us from distinguishing between the possible spin states.

Another explanation is the formation of electronically excited ClO. This is unlikely though in light of our current knowledge of ClO. The lowest observed excited state of ClO is the *A* state which lies ~90 kcal/mol above the ground state so $\Delta H^\circ_0(Cl_2O \rightarrow ClO(A) + Cl) = 122$ kcal/mol. Energetically this state is not accessible at 248 or 308 nm, since the photons energies are only 115 or 93 kcal/mol, respectively. However, a lower excited state of ClO corresponding to a quartet state ($^4\Sigma^-$) is predicted. Theoretical calculations predict that this state lies 51 kcal/mol above the ground state. If the theoretical calculations are correct, this cannot explain the bimodality in the 308 nm distribution since accessing the quartet state would leave only 7 kcal/mol available for translation. At 248 nm, it is possible though that the slower peak could have contributions from the formation of the *A* state. However, any ClO formed in the *A* state must have translational energies less than 30 kcal/mol. This would leave a discontinuity on the slow side of the fast peak and would not explain the irregular shape of the distributions. Thus, it is unlikely that the formation of the $^4\Sigma^-$ state is the root of the bimodal distributions.

193 nm

We present here the first direct evidence of the concerted reaction $Cl_2 + O(^3P)$. Other experiments have alluded to the existence of the channel but have been unable to confirm it. Sander *et al.* measured a large yield of atomic oxygen ($\Phi_O = 0.25 \pm 0.05$) when Cl_2O was irradiated with broad-band ultraviolet radiation (180 nm $\leq \lambda$), which they attributed to the reactions 2 and 4. Since they only measured the atomic oxygen yield, they were unable to discern from which channel the oxygen originated. Our results unequivocally show that the concerted reaction channel is accessed. However, probably the majority of the atomic oxygen observed by Sander *et al.* is due to reaction 2. We found that the majority (87%) of the Cl_2 produced at 193 nm is formed internally hot and undergoes spontaneous secondary dissociation; thus, contributing to the $2Cl + O(^3P)$ yield. Any events leading to ClO + Cl also contribute to reaction 2 since almost all of the ClO is formed sufficiently hot and undergoes spontaneous secondary dissociation. Additionally, we will show later in this paper that the $2Cl + O(^3P)$ channel is also accessed at longer wavelengths where reaction 2 is not occurring.

We are unable to calculate an exact branching ratio between reactions 2 and 4 because we lack the translational energy distribution for the $2Cl + O(^3P)$ channel. The complexity of the *m/e*=35 spectra and the variety of channels leading the $2Cl + O(^3P)$ reaction prohibit us from determining the ratio.

V. CONCLUSION

We demonstrated that the dissociation dynamics of Cl_2O are highly wavelength dependent. At 193 nm, we observed only the $Cl_2 + O$ and $2Cl + O$ channels. Momentum matching the $Cl_2 + O$ products allowed us to confirm that the channel is a single photon event. The ClO + Cl channel was also accessed; however, most of the ClO was formed vibrationally hot and dissociated thus contributing to the $2Cl + O$ channel. At 308 nm, we

only observed products from the ClO + Cl channel. We saw a similar result at 248 nm, but some of the ClO products were formed sufficiently hot to undergo spontaneous secondary dissociation accessing the 2Cl + O channel.

VI. REFERENCES

1. W. Finkelnburg, H.J. Schumacher, G. Stieger, *Z. Phys. Chem, Abt. B* **15**, 127 (1931).

2. H.J. Schumacher, R.V. Townend, *Z. Phys. Chem, Abt. B* **20**, 375 (1933).

3. F.H.C. Edgecomb, R.G.W. Norrish, F.R.S. Thrush, and B.A. Thrush, *Proc. Roy. Soc. Lond. A* **243**, 24 (1957).

4. N. Basco, S.K. Dogra, *Proc. Roy. Soc. Lond. A* **323**, 401 (1971).

5. S.P. Sander, R.R. Friedl, *J. Phys. Chem.* **93**, 4764 (1989).

6. C.L. Lin, *J. Chem. & Eng. Data* **21**, 411 (1976).

7. S. Langhoff, personal communication.

8. J.B. Nee, *J. Quant. Spectrosc. Radiat. Transfer* **46**, 55 (1991).

9. C.M. Nelson, T.A. Moore, M. Okumura, T.K. Minton, *J. Phys. Chem*, (1993), in press.

10. Y.T. Lee, J.D. McDonald, P.R. LeBreton, D.R. Herschbach, *Rev. Sci. Instrum.* **40**, 1402 (1969).

11. G.H. Cady, *Inorg. Synth.* **5**, 156 (1957).

12. M.W. Chase, Jr., C.A. Davies, J.R. Downey, Jr., D.J. Frurip, R.A. McDonald, A.N. Syverud, *JANAF Thermochemical Tables, 3rd Ed.* **14**, (1985).

13. S. Abramowitz, M.W. Chase, Jr., *Pure & Appl. Chem.* **63**, 1449 (1991).

VII. FIGURE CAPTIONS

Figure 1. Absorption spectrum of Cl_2O.

Figure 2. Energy level diagram showing the possible dissociation channels and relative photon energies.

Figure 3. Laboratory TOF distributions of *m/e*=51 at 308 nm for three detector angles. The solid lines are the calculated fits using the $P(E_T)$ shown in Figure 4.

Figure 4. $P(E_T)$s for the ClO + Cl channel at 248 and 308 nm. The $P(E_T)$s were determined by fitting the *m/e*=51 data.

Figure 5. Laboratory TOF distributions of *m/e*=35 at 308 nm for two detector angles. The solid lines are the calculated fits using the $P(E_T)$ shown in Figure 4. The dashed lines are the individual contribution from each product.

Figure 6. Laboratory TOF distributions of *m/e*=51 and *m/e*=35 at 248 nm for a 40° detector angle. The solid lines are the calculated fits using the $P(E_T)$ shown in Figure 4. The dashed lines are the individual contribution from each product.

Figure 7. Energy level diagram for the photodissociation of Cl_2O at 248 nm. The $P(E_T)$ for the ClO + Cl is shown to illustrate how the available energy is partitioned.

Figure 8. Laboratory TOF distributions of *m/e*=16 at 193 nm for two detector angles. Circles are experimental points and the solid lines are the calculated fits using the $P(E_T)$ for the Cl_2 + O channel shown in the Figure 9.

Figure 9. $P(E_T)$ for the Cl_2 + O channel at 193 nm. The shaded area shows the translational energies which correspond to internal energies less than the Cl-Cl bond strength.

Figure 10. Laboratory TOF distributions of *m/e*=70 at 193 nm for two detector angles. The solid lines are the calculated fits using the truncated $P(E_T)$ for the Cl_2 + O channel determined from the *m/e*=16 signal. The $P(E_T)$ is truncated at translational energies which correspond to internal energies in the Cl_2 fragment greater than the Cl-Cl bond strength. The dashed line shows the fit obtained using the full $P(E_T)$.

Figure 11. Energy level diagram for the photodissociation of Cl_2O at 193 nm. The $P(E_T)$ for the Cl_2 + O is shown to illustrate how the available energy is partitioned.

Figure 12. Laboratory TOF distributions of *m/e*=51 and *m/e*=35 at 193 nm recorded at 40° detector angle. The dotted line in the *m/e*=51 spectrum corresponds to 152 μs - see text for details.

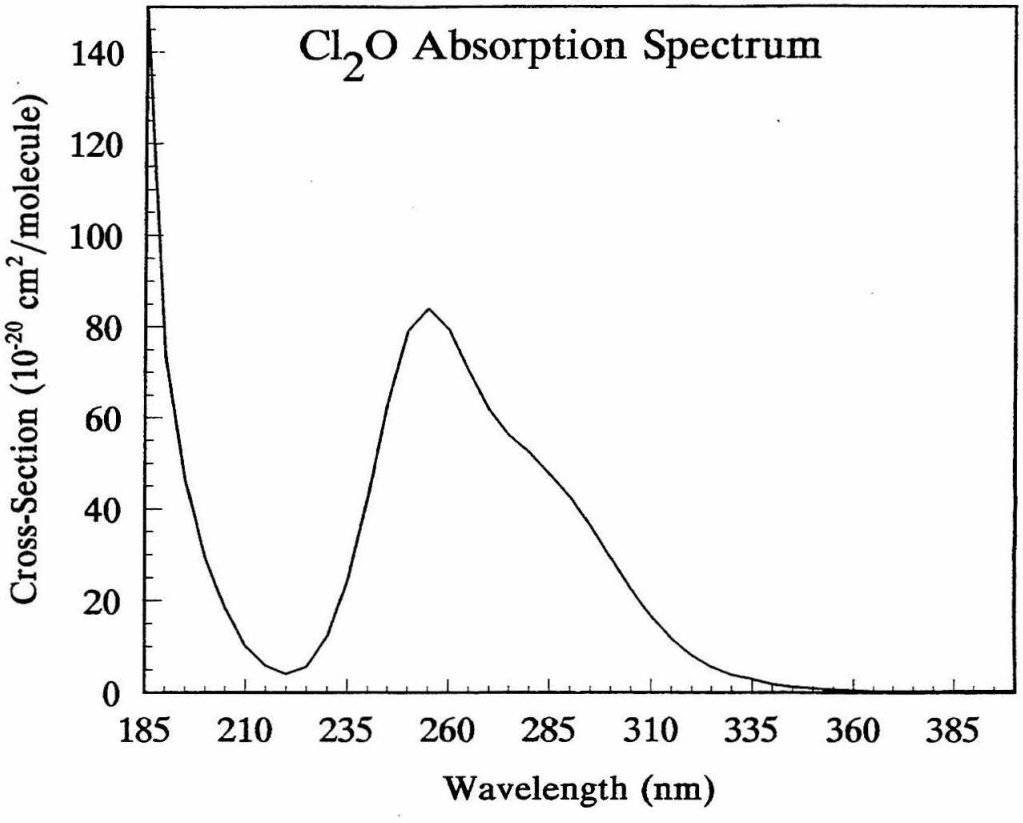
Cl2O Absorption Spectrum
Cross-Section (10-20 cm2/molecule)
140
120
100
80
60
40
20
0
185
210
235
260
285
310
335
360
385
Wavelength (nm)

Figure 1

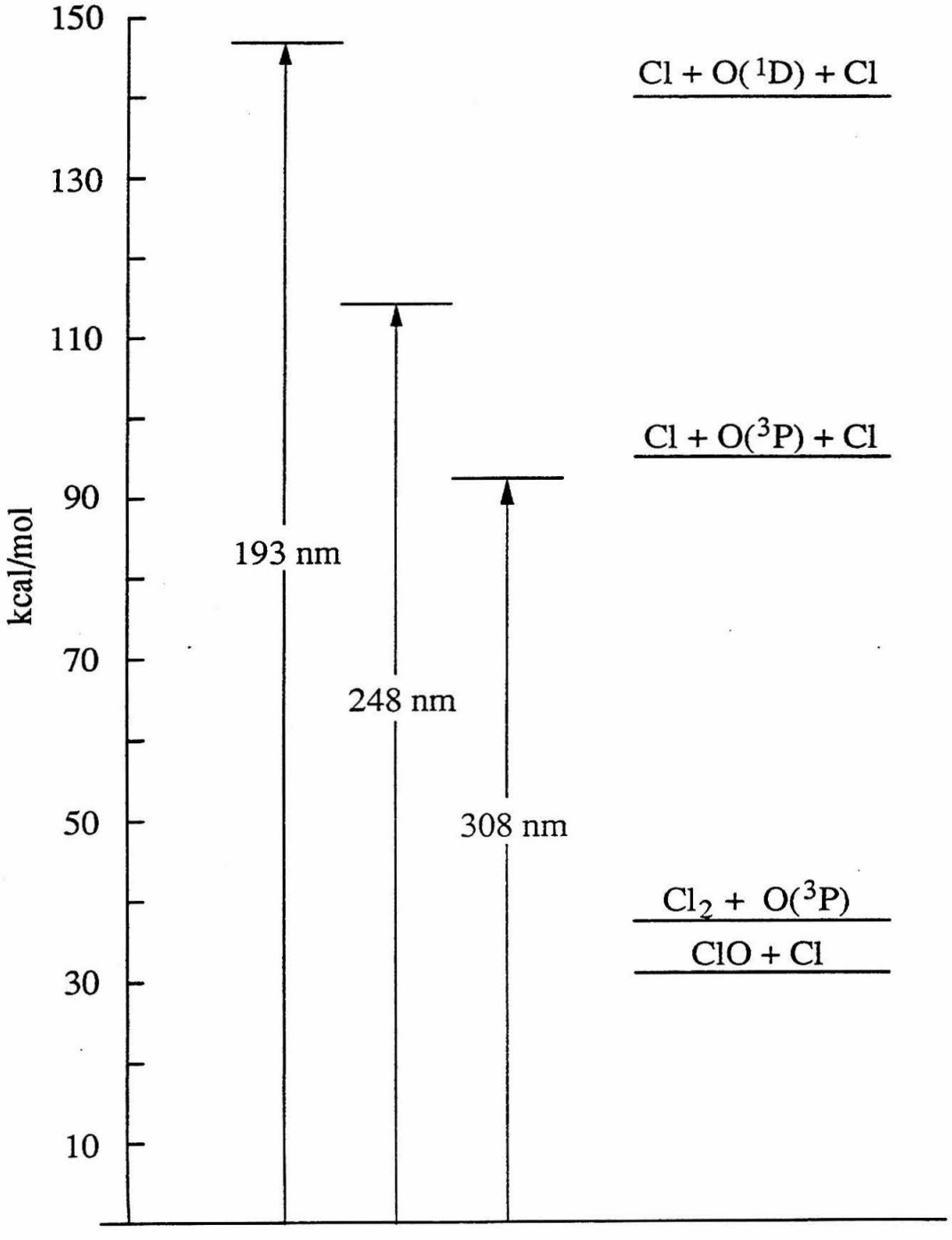
150
130
110
90
70
50
30
10
kcal/mol
193 nm
248 nm
308 nm
Cl + O(1D) + Cl
Cl + O(3P) + Cl
Cl2 + O(3P)
ClO + Cl

Figure 2

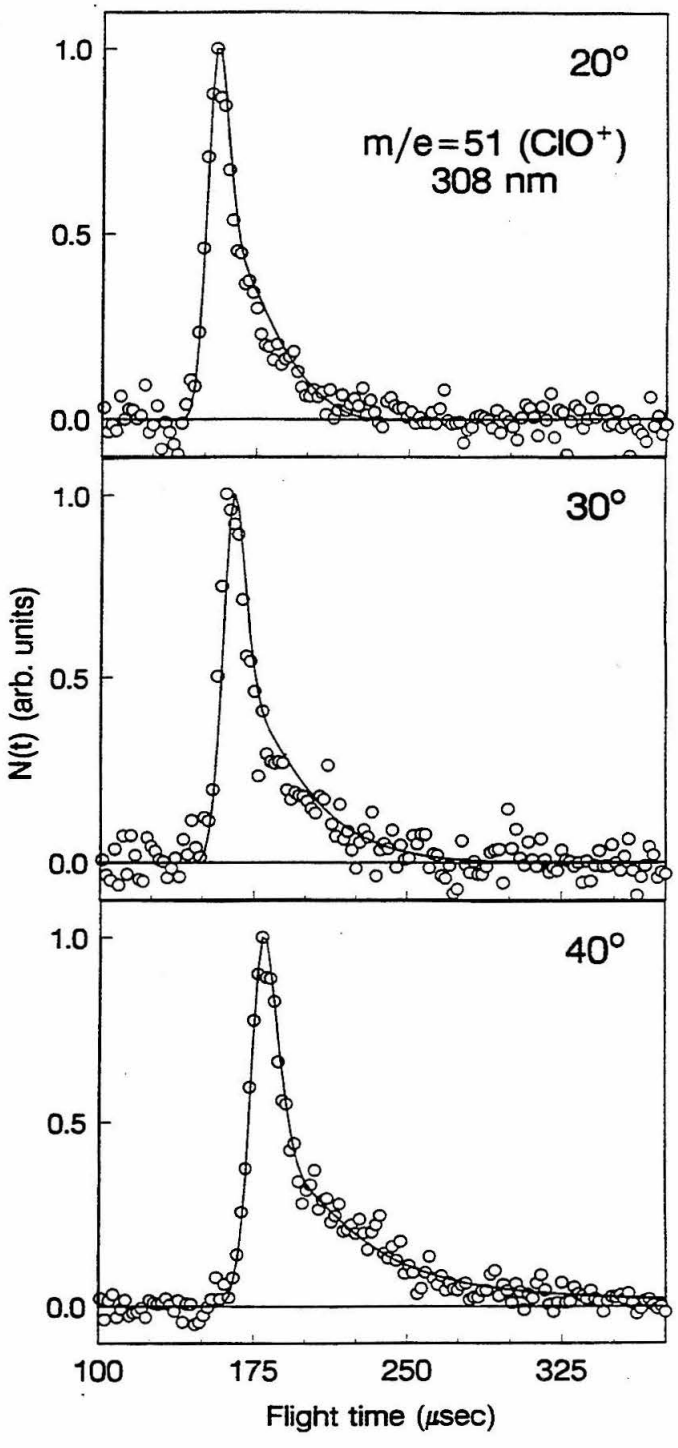
20°
m/e=51 (ClO+)
308 nm
30°
40°
1.0
0.5
0.0
N(t) (arb. units)
100
175
250
325
Flight time (μsec)

Figure 3

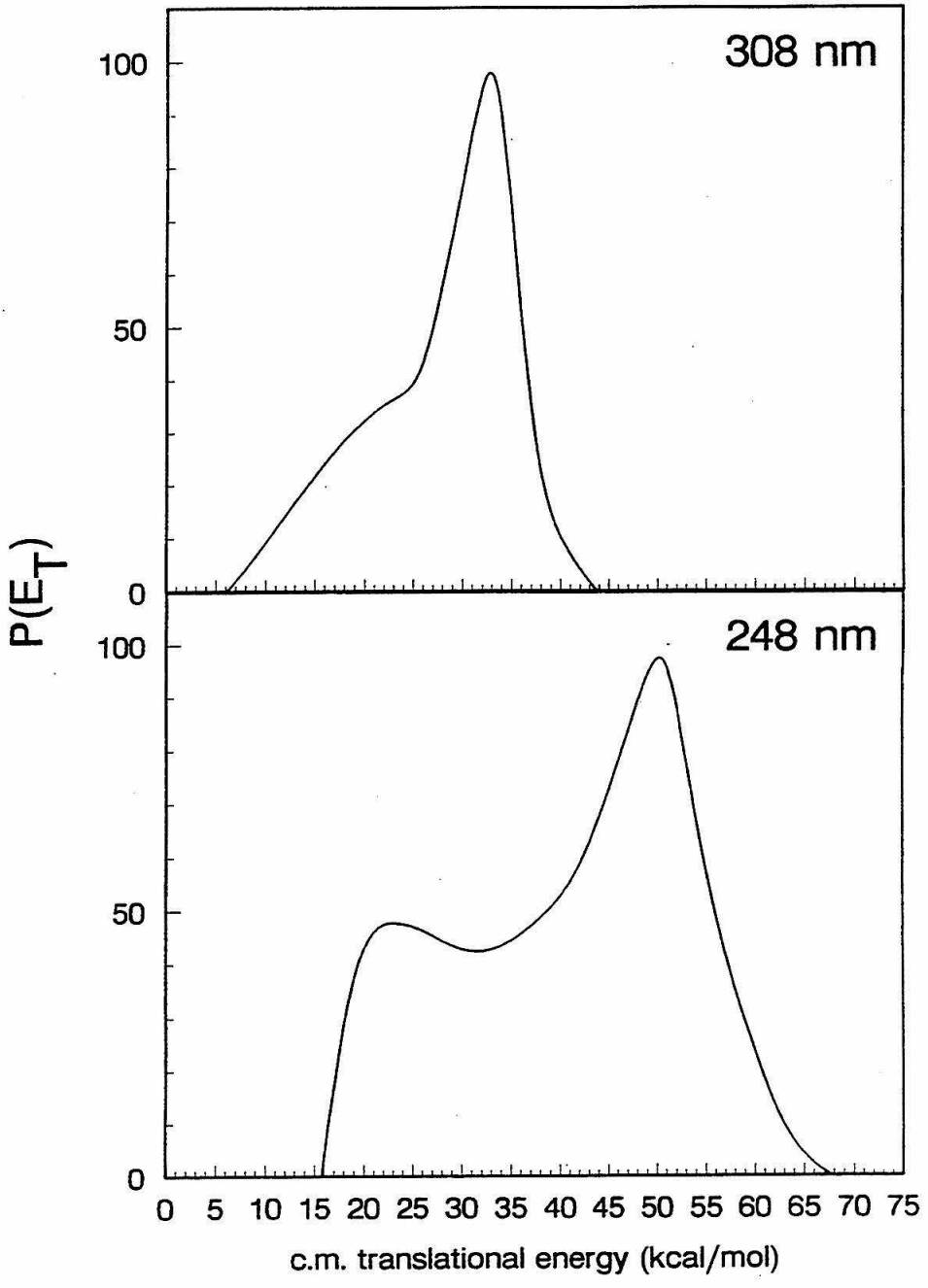
308 nm
248 nm
100
50
0
100
50
0
P(E_T)
0 5 10 15 20 25 30 35 40 45 50 55 60 65 70 75
c.m. translational energy (kcal/mol)

Figure 4

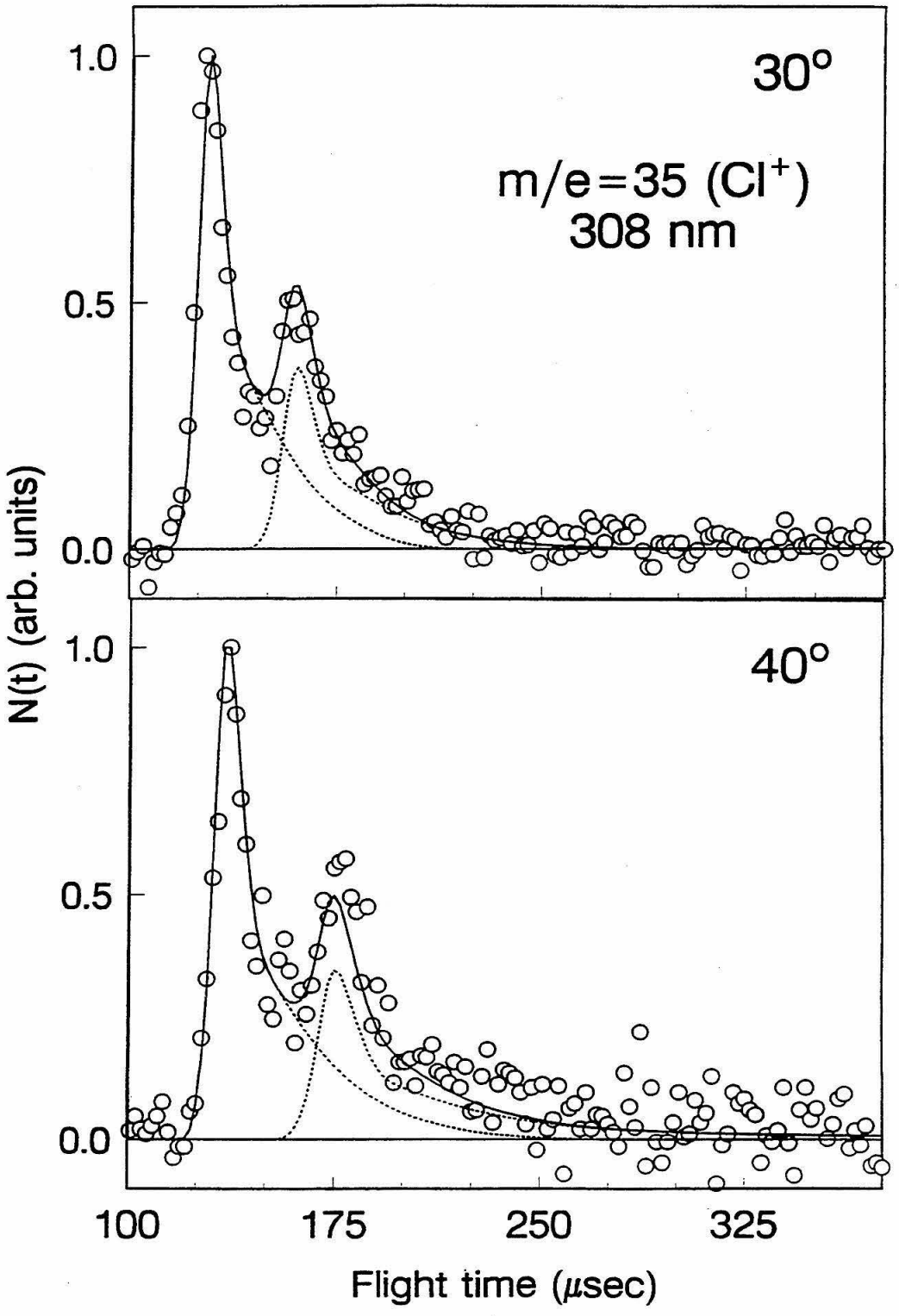
30°
m/e=35 (Cl+)
308 nm
40°
1.0
0.5
0.0
N(t) (arb. units)
100
175
250
325
Flight time (μsec)

Figure 5

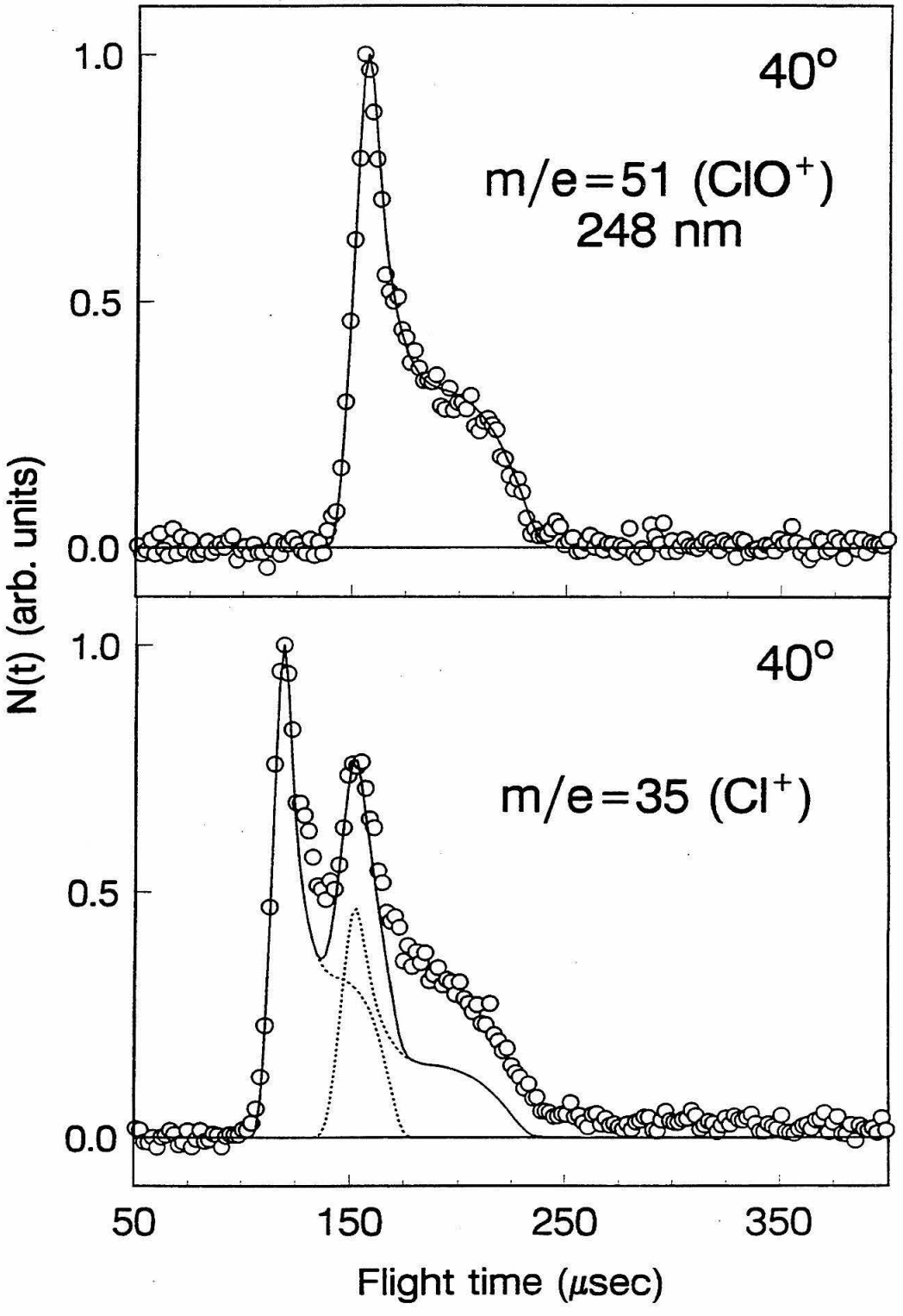
40°
m/e=51 (ClO+)
248 nm
40°
m/e=35 (Cl+)
N(t) (arb. units)
1.0
0.5
0.0
50
150
250
350
Flight time (μsec)

Figure 6

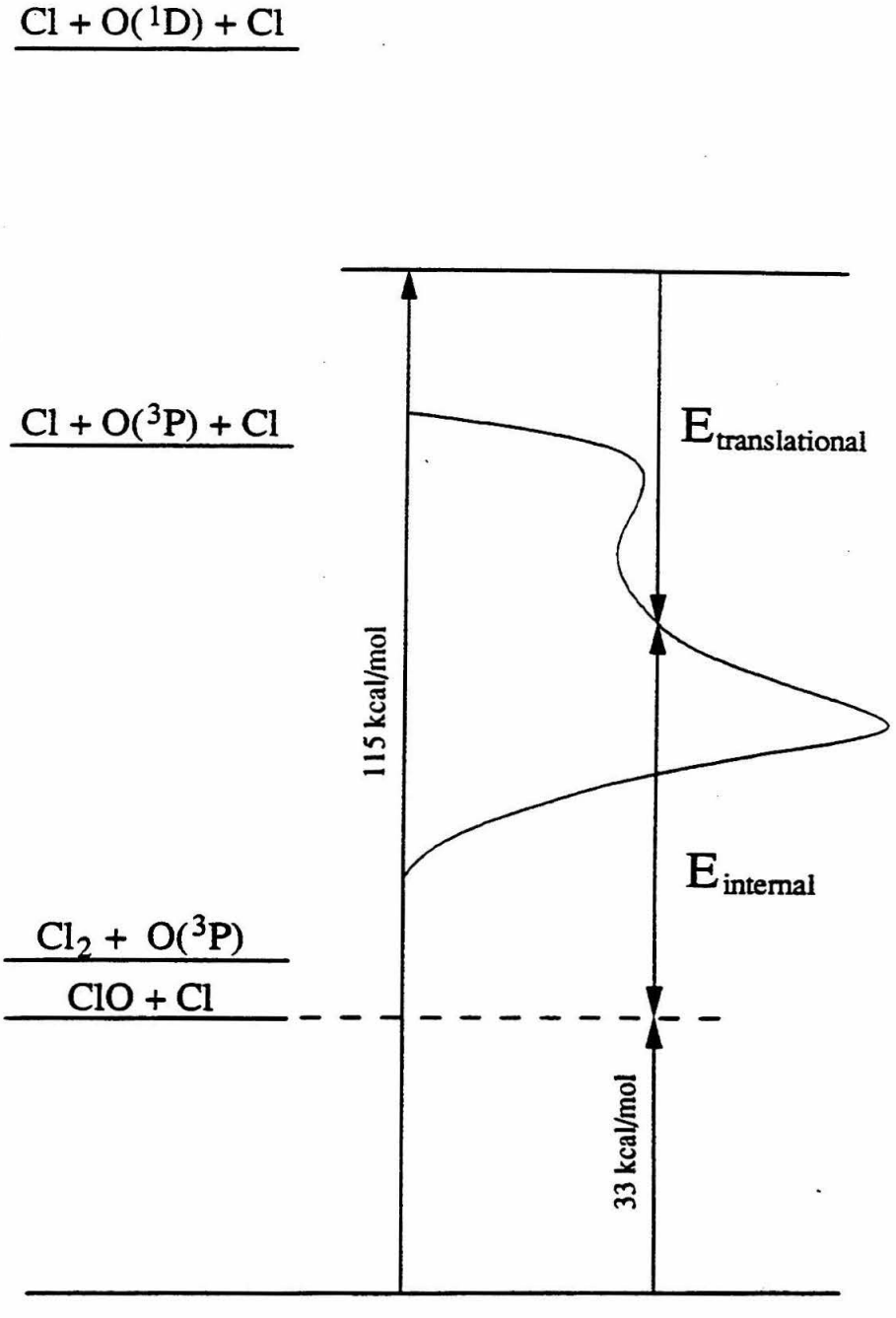
Cl + O(1D) + Cl
Cl + O(3P) + Cl
Etranslational
115 kcal/mol
Einternal
Cl2 + O(3P)
ClO + Cl
33 kcal/mol

Figure 7

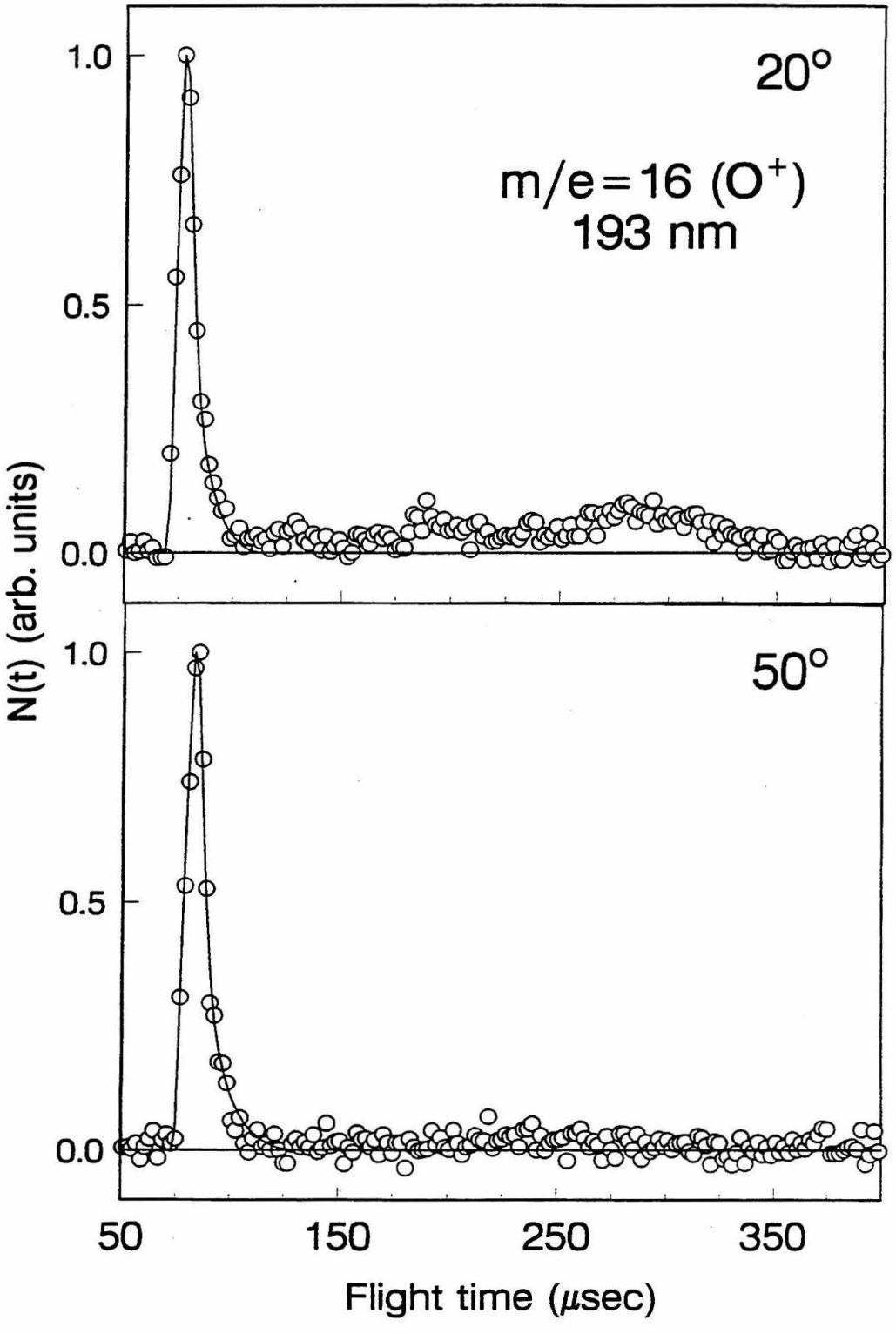
20°
m/e=16 (O+)
193 nm
50°
1.0
0.5
0.0
N(t) (arb. units)
50
150
250
350
Flight time (μsec)

Figure 8

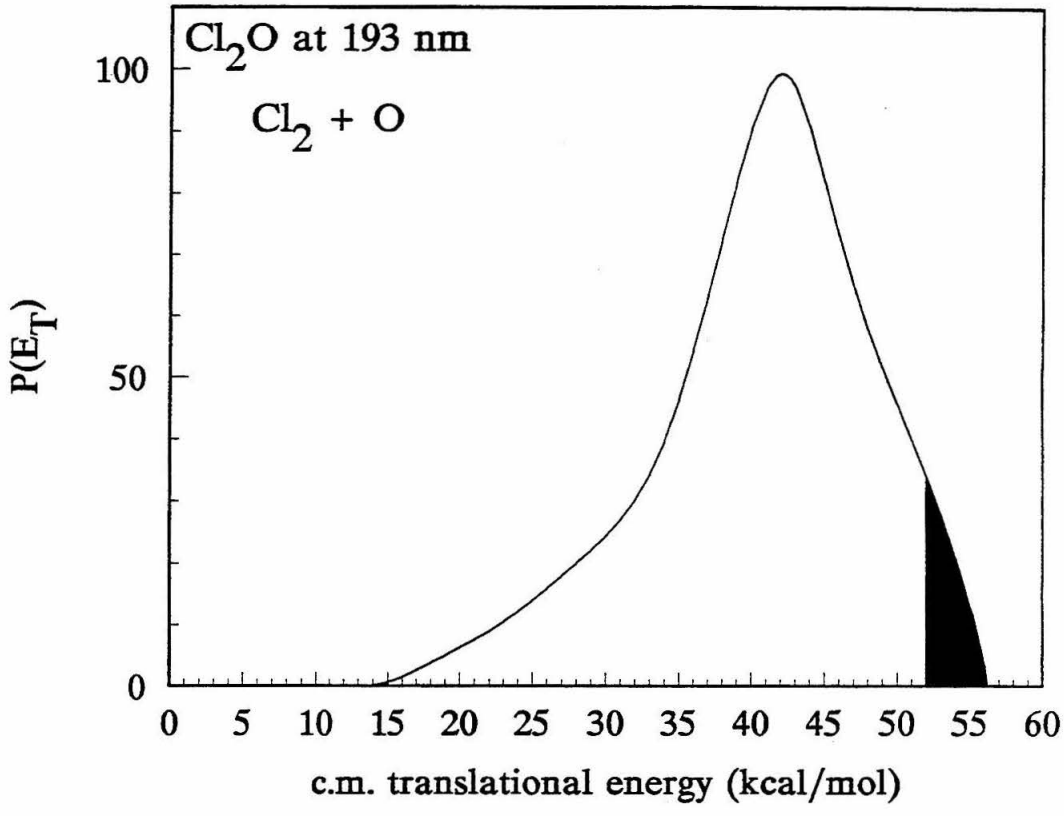
Cl2O at 193 nm
Cl2 + O
100
50
0
P(ET)
0 5 10 15 20 25 30 35 40 45 50 55 60
c.m. translational energy (kcal/mol)

Figure 9

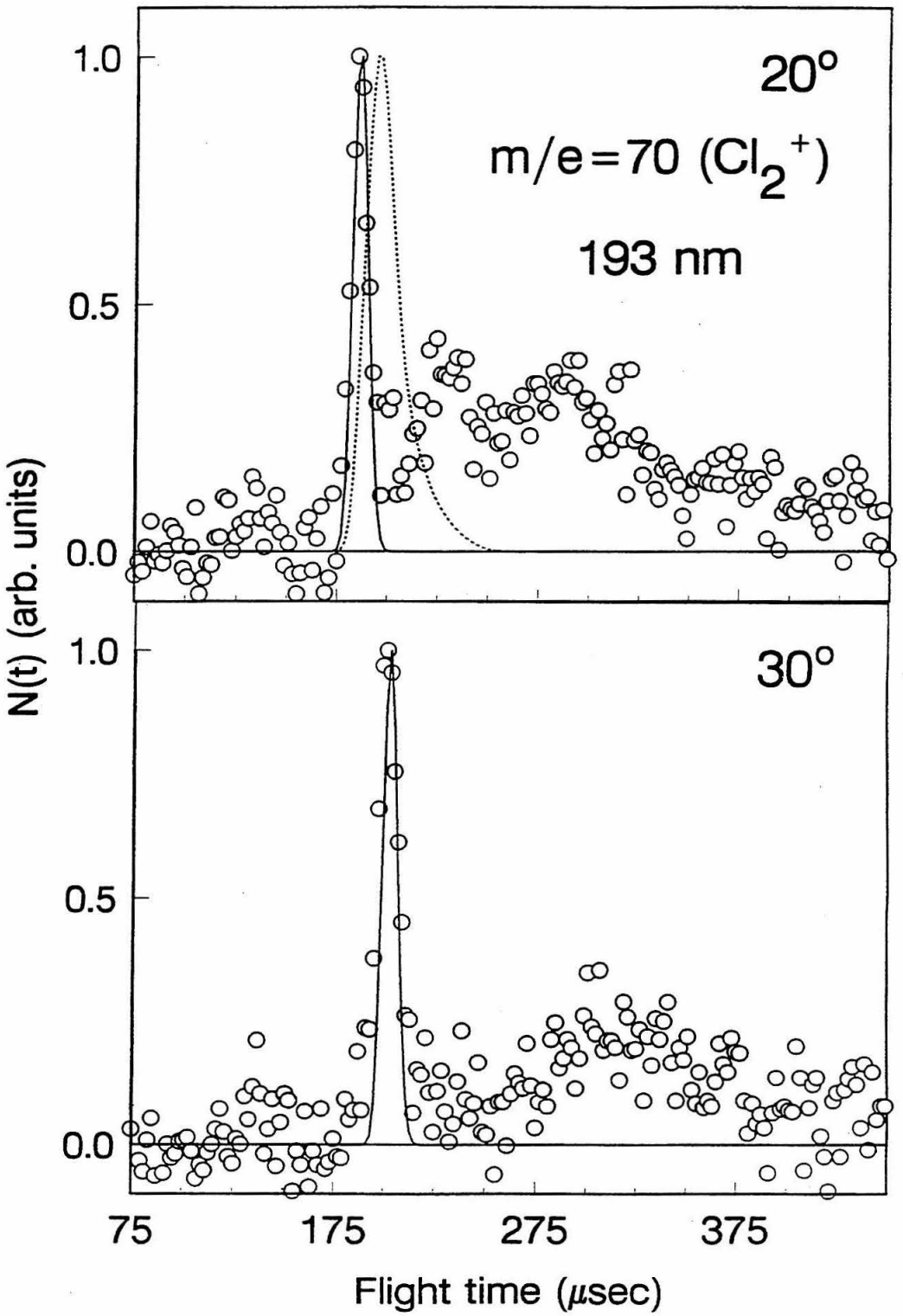
20°
m/e=70 (Cl_2^+)
193 nm
30°
1.0
0.5
0.0
N(t) (arb. units)
75
175
275
375
Flight time (μsec)

Figure 10

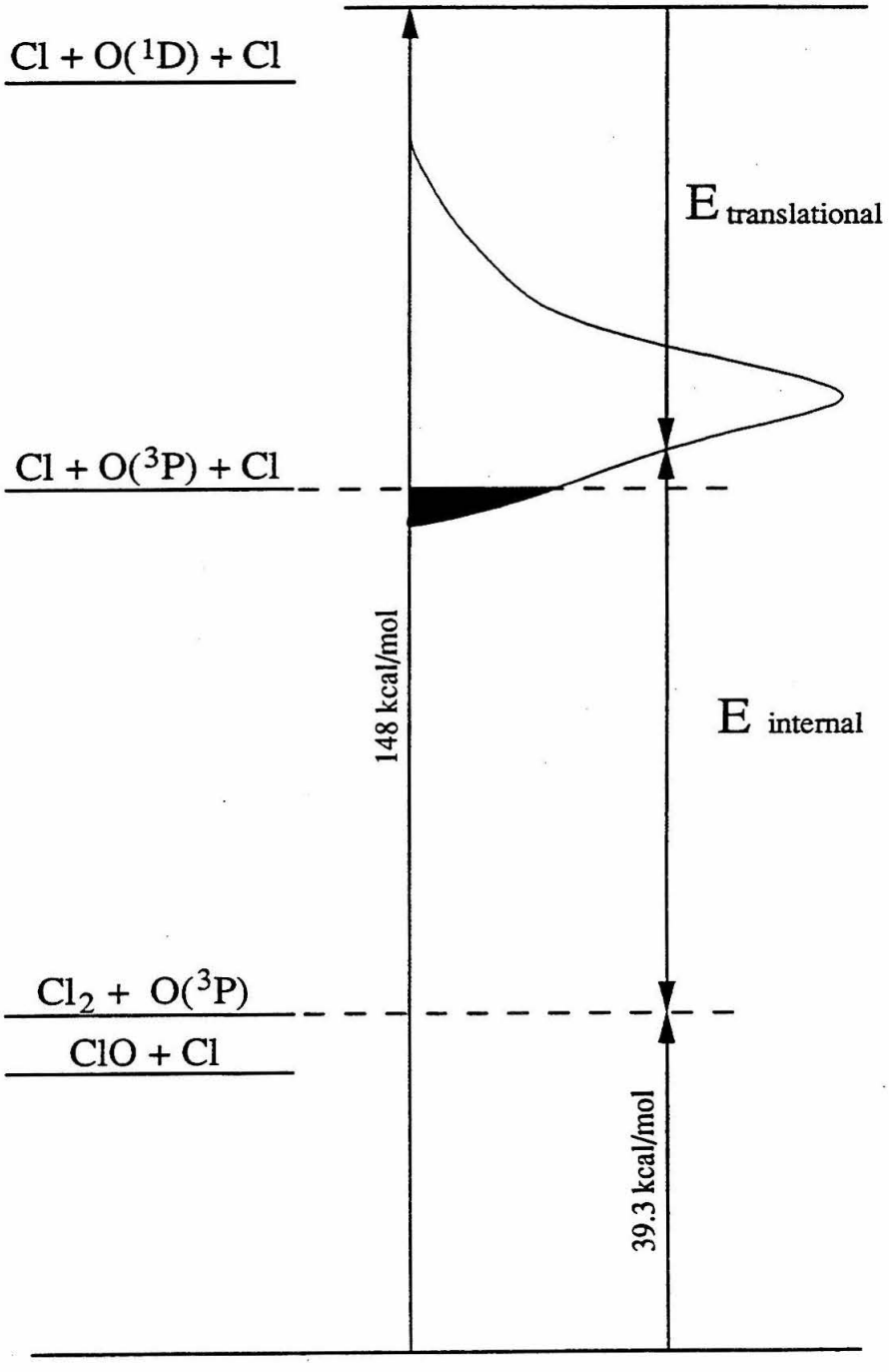
Cl + O(1D) + Cl
E translational
Cl + O(3P) + Cl
148 kcal/mol
E internal
Cl2 + O(3P)
ClO + Cl
39.3 kcal/mol

Figure 11

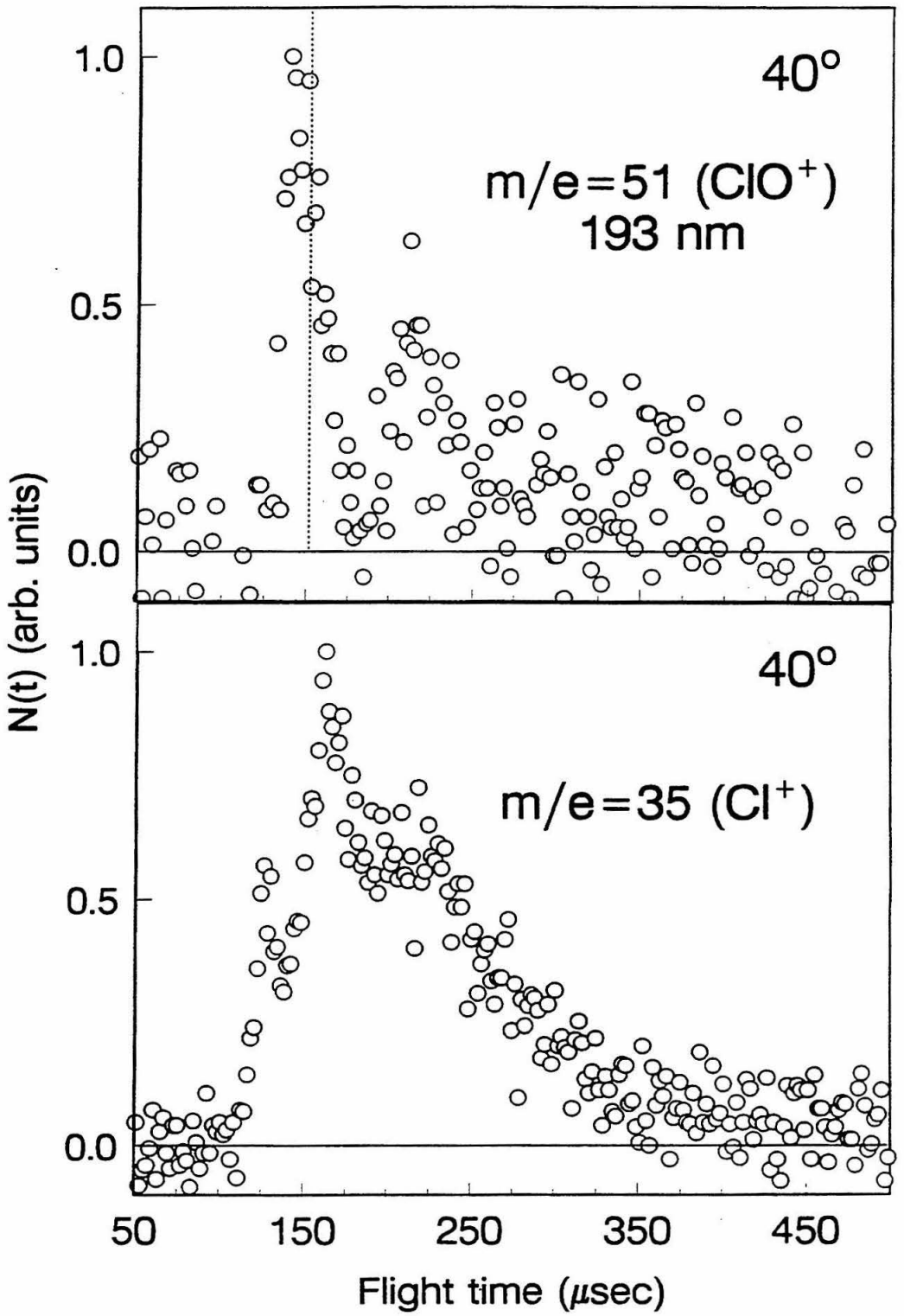
40°
m/e=51 (ClO+)
193 nm
40°
m/e=35 (Cl+)
N(t) (arb. units)
1.0
0.5
0.0
1.0
0.5
0.0
50
150
250
350
450
Flight time (μsec)

Figure 12

Chapter 4

ClOOCl Molecular Beam Source

ABSTRACT

Our group plans to study the photodissociation dynamics of ClOOCl using the molecular beam technique of photofragmentation translational energy spectroscopy. The most difficult aspect of this experiment is generating a molecular beam of ClOOCl. This chapter discusses the development of a pulsed ClOOCl source and presents two possible chemical mechanisms for generating the species. The construction of a testing chamber for the source is also presented.

I. INTRODUCTION

Current models predict that the ClO dimer mechanism accounts for 70% of the ozone loss over the polar regions.

$$2\,(Cl + O_3 \longrightarrow ClO + O_2) \quad (1)$$

$$2ClO + M \longrightarrow ClOOCl + M \quad (2)$$

$$ClOOCl + h\nu \longrightarrow Cl + OOCl \quad (3)$$

$$ClOO + M \longrightarrow Cl + O_2 \quad (4)$$

$$\text{Net:} \quad 2\,O_3 \longrightarrow 3\,O_2 \quad (5)$$

The pivotal step in this mechanism is the photolytic reaction which releases atomic chlorine from the ClO dimer. If ClOOCl dissociated to form two ClO instead, a null cycle would result, and ClOOCl dimer formation would not lead to ozone destruction. Therefore, the branching ratio of ClOOCl photolysis into Cl and ClO products is critical in determining the importance of this mechanism.

Possible dissociation channels are

$$ClOOCl \longrightarrow ClO + ClO \quad \Delta H(0\text{ K}) = 16\text{ kcal/mol} \quad (6)$$

$$\longrightarrow Cl + ClOO \quad 20\text{ kcal/mol} \quad (7)$$

$$\longrightarrow 2Cl + O_2 \quad 25\text{ kcal/mol} \quad (8)$$

$$\longrightarrow Cl_2 + O_3 \quad -32.5\text{ kcal/mol.} \quad (9)$$

Current studies hold that ClOOCl photolysis in the ultraviolet range leads solely to Cl + OOCl which mandates that the stronger Cl-O bond break preferentially over the weaker ClO-OCl bond. When Molina and Molina first proposed this mechanism they rationalized the bond selective nature of ClOOCl photolysis by arguing that ultraviolet absorption excited a $n\rightarrow\sigma^*$ transition localized on the Cl-O chromophore, as in $ClONO_2$.[1] Studies at that time held that $ClONO_2$ photodissociated almost exclusively to $Cl + NO_3$. Our new branching ratio for $ClONO_2$, however, shows that the photodissociation dynamics of

$ClONO_2$ are not a simple Cl-O bond selective picture. The photolysis of ClOOCl is also likely to be equally complex.

Two experiments on ClOOCl photolysis have found that the quantum yield for production of Cl + ClOO is unity or greater, but large uncertainties remain in both measurements. Cox and Hayman photolyzed a Cl_2O-N_2 mixture at 254 nm in a static photolysis cell and monitored the ClO, Cl_2O and ClOOCl concentrations by UV absorption spectroscopy.[2] Acceleration of Cl_2O loss was attributed to reactions with atomic chlorine formed from ClOOCl photolysis. Fitting their results to a multi-step kinetic mechanism, they determined a chlorine quantum yield of 1.98 ± 0.8. Because their quantum yield is inferred from the secondary reactions, any uncertainty in the kinetic mechanism would introduce error into the calculated value. Additionally, Cox and Hayman failed to mention any attempt to account for atomic chlorine release from ClO photolysis. At 254 nm, ClO has a strong absorption cross section, 4.5×10^{-18} cm^2, and photodissociates to Cl and $O(^1D)$. Some of the atomic chlorine attributed to ClOOCl dissociation could result from ClO photolysis which would lower the atomic chlorine quantum yield for ClOOCl.

Alternatively, Molina *et al.* directly detected the production of Cl atoms using a pulsed photolysis technique in a flow cell.[3] ClOOCl was produced using the following sequence of reactions:

$$F + HCl \longrightarrow HF + Cl \qquad (10)$$

$$Cl + O_3 \longrightarrow ClO + O_2 \qquad (1)$$

$$2ClO + M \longrightarrow ClOOCl + M. \qquad (2)$$

ClOOCl concentrations were determined by measuring the absorbance in the 200-260 nm region. Atomic chlorine production was monitored using resonance fluorescence, and they reported a quantum yield of 1.03 ± 0.12. They detected no ClO using NO titration; however, the accuracy of this technique has been brought into question with its inability to detect significant amounts of ClO formation in the $ClONO_2$ photolysis experiments.

Additionally, their quantum yield is based on the absorption cross section ratio $\sigma_{245}/\sigma_{308}$ for ClOOCl at 245 and 308 nm. Large discrepancies exist for this value. The value used by Molina *et al.* is larger than currently accepted values. If one uses the currently recommended values,[4] the quantum yield drops to 0.6.

Our $ClONO_2$ experiment presented in Chapter 2 demonstrates how molecular beam techniques can complement existing kinetics experiments by allowing direct detection of primary photoproducts and furnishing insights into the photodissociation process itself. Given the uncertainties in the previous experiments on ClOOCl photolysis and the extreme importance of ClOOCl photolysis in understanding polar stratospheric ozone depletion, our group plans to investigate the photolysis of the ClO dimer using photofragmentation translational energy spectroscopy. The principal objective of the experiment is to determine the branching ratio between the Cl + OOCl and ClO + ClO channels.

The experimental details will be similar to those used in Chapters 2 and 3. A molecular beam of ClOOCl will be photolyzed at 308 nm in the Crossed Molecular Beams Apparatus (CMBA) located at the Jet Propulsion Laboratory. The primary products will be directly detected off-axis and their nascent translational energy and angular distributions recorded. The most challenging aspect of this experiment is generating a molecular beam of ClOOCl. This chapter discusses the development of a pulsed ClOOCl source and presents two possible chemical mechanisms for generating the species. Since the CMBA is in high demand, a testing chamber for the source was constructed at Caltech and is also discussed.

II. SOURCE

Molecular Beam. The molecular beam source consists of a 1.25" quartz tube with 1 mm inner diameter attached to the front of a cooled piezoelectric pulsed valve. Gas flows out of the pulsed valve through the channel. Near the entrance of the quartz channel,

a pulsed laser is focused so that photolysis occurs in the first few mm. The photolyzed gas reacts as it flows through the channel; as the gas exits, it undergoes a free jet expansion. The center of the free jet passed through a skimmer (1 mm diam. orifice) and enters the second differential region. The beam is further collimated through a square aperture before entering the main chamber where the interaction region is located.

Pulsed Valve. The pulsed valve has a piezo-driven plunger which can operate up to 1 kHz. The stagnation pressure behind the pulsed valve is 300 to 1000 torr.[5] The pulsed valve exit and quartz channel must be cooled to 247 K to minimize ClO self reactions that yield products other than ClOOCl

An extended nozzle design is used because the piezoelectric plate located in the valve cannot operate at low temperatures (see Figure 1). The extended nozzle consists of a 3 in. long thin walled (0.30" I.D. x .038" wall) stainless steel tube welded to mounts on both ends. The rear mount keys into the pulsed valve and ensures that the nozzle is centered. On the front mount, a stainless steel nozzle plate is seated on the front of which a quartz nozzle attaches. The quartz nozzle is held in place by a Kel-F clamp. This design allows us to interchange various quartz nozzles without having to readjust the poppet each time. To ensure a reliable operating seal at the low temperatures, a special Delrin poppet tip was incorporated. The Delrin poppet tip screws onto the end of the aluminum plunger and is seated in a cone on the back of the stainless steel nozzle plate.

The front mount is cooled by four thermoelectric (Peltier) coolers (Marlow Industries, MI1025T; $\Delta T_{max}(27°C) = 64°C$; $\Delta Q_{max}(27°C) = 5.0$ W; $I_{max}=1.8$ amps) hooked up in series. Thermoelectric coolers are solid-state electric heat pumps; by varying the current flowing through the coolers, the amount of cooling can be adjusted. The hot surfaces of the Peltier coolers are cooled by a jacketed aluminum heat sink with isopropanol circulating through the jacket. When installing the Peltier coolers, great care must be taken to tighten the modules evenly; uneven stress on the devices can destroy the

coolers by causing minute cracks in the semiconductor couples. The temperature of the nozzle is monitored by a programmable temperature/process controller (Burling Instruments, 6509-RAY0-40) which in turn regulates the current to the thermoelectric coolers. Temperatures around 248 K have been achieved using this set-up.

Laser. Laser light will be coupled into the machine through fiber optics (3M, 400μ m core diam., FG-400-UAT). Either an excimer laser operating at 308 nm or a tripled pulsed YAG (355 nm) will be focused into the fiber optic using a +100 mm focal length plano-convex lens (Herasil). The amount of light focused into the fiber optic is regulated by an iris located in front of the lens. The fiber optic is placed in a fiber chuck which is mounted on an XYZ translator. Fine positioning of the fiber optic into the focal point of the lens is critical to maximizing the amount of power that the fiber transmits. Preliminary tests run at 308 nm show that over 4 mJ/pulse of light can be transmitted through a single fiber. In order to photolyzed sufficient amounts of the Cl_2 or Cl_2O, powers larger than 4 mJ/pulse may be required in which case two fibers may be used. Upon exiting the fiber optic the light diverges with a 19° angle. Thus, the end of the fiber optic should be located approximately 5 mm from the channel.

III. TESTING CHAMBER

A schematic of the testing system is shown in Figure 2. The first differential chamber containing the source is the same one that is used on the CMBA. It consists of the ten inch tee attached to a reducer pumped by a ten inch diffusion pump (Varian HS10; pumping speed (He) - 4800 l/s). The second differential region is a ten inch can which is pumped by a baffled six inch diffusion pump (Varian VHS6; p.s.(He) - 1350 l/s). The second differential region is separated from the detection region by a 0.065" hole. As the beam enters the detection region, the molecules in the beam are ionized by an Extranuclear Electron Impact Ionizer (model 041-1), and the resultant ions are focused using three einzel

lenses into an Extranuclear quadrupole mass filter equipped with 3/4 inch rods. Ions that pass through the quadrupole are detected using a Galileo 4816 channeltron (10^8 electron gain at 3 kV). This final detection region is pumped by a Balzers TPU050 turbomolecular pump (p.s.(He) - 55 l/s). When the beam is on, typical pressures in the final region are 4 x 10^{-6} torr.

IV. CHEMISTRY

The unstable nature of ClOOCl mandates that the dimer must be formed in situ, prior to or immediately after the expansion through the nozzle. Two different chemical approaches to generate ClOOCl are presented here. In the first, pure Cl_2O is seeded in helium at a stagnation pressure that can be varied (300-1000 torr) to adjust the amount of flow through the nozzle. At the entrance to the quartz channel, the Cl_2O is photolyzed at 308 nm to produce ClO and Cl. The atomic chlorine quickly reacts with residual Cl_2O to form ClO.

$$Cl_2O + h\nu \longrightarrow Cl + ClO \qquad (11)$$

$$Cl + Cl_2O \longrightarrow Cl_2 + ClO. \qquad (12)$$

Thus, from one photodissociation event two ClO molecules are created. The ClO then dimerizes while flowing through the channel or during the supersonic expansion at the exit of the channel.

$$ClO + ClO + M \longrightarrow ClOOCl + M \qquad (2)$$

In the second approach, Cl_2 is added to the Cl_2O/He gas mixture and photolyzed at 355 nm. In this scenario, the Cl_2 photolyzes to form two atomic chlorines which react with Cl_2O via reaction 12 to produce ClO. Thus, here again two ClO molecules are created for each photolytic event.

We modeled the chemistry for these two scenarios by solving rate equations for the gas packet as it flowed through the channel. The hydrodynamics in the channel were

treated by the theory of one-dimensional adiabatic flow of a compressible fluid through a constant pipe with friction. Assuming ideal gas behavior, which is reasonable for He at 200 K seeded with a few percent Cl_2, this theory gives the pressure, temperature and flow velocity analytically as functions of the Mach number, and implicitly as functions of position along the channel. Pressure and temperature drop and the velocity increases with distance down the channel. In the channel, the flow velocity is subsonic but increases to the speed of sound at the channel exit where a free expansion ensues. The calculation also incorporated variations in density and reaction rates as the pressure and temperature of the gas packet evolved. When calculating the changes in temperature and density of the photolysis packet, the excess energy after photolysis, the thermicity of the subsequent reactions and the rapid cooling by adiabatic expansion of the photolyzed volume were taken into account. Heat removed by conduction to the walls, however, was ignored. Flow conditions for the source are presented in Table I.

Using the model, we determined the relative abundance of product species for various initial densities using both scenarios. The results are presented in Tables II and III, and Figures 3 and 4.

Figure 3 shows the results of a run starting with 2% pure Cl_2O in helium. The calculation assumes that 5 mm from the entrance of the channel 40% of the Cl_2O is photolyzed at 308 nm. With a Cl_2O absorption cross section of 4.64×10^{-19} cm^2 at 308 nm, 5.5 mJ/mm^2 per pulse are required. Mole fractions for a number of key species in the channel are plotted as functions of time. 73.5 μs represents the exit of the channel. The model shows that within 2 μs after photolysis, most of the atomic chlorine formed has reacted to form ClO and that very little ClOOCl is formed. However, as the gas packet travels through the channel, the ClOOCl density increases to a final value of 9.3×10^{15} mol/cm^3 at the exit of the channel. Large amounts of Cl_2O, Cl_2 and ClO are also present at

the exit. Densities of other chlorine oxide species, such as ClOO, OClO and Cl_2O_3, are two to three orders of magnitude lower than the ClOOCl density.

The large concentrations of the diatomics, Cl_2 (2.8×10^{16} mol/cm^3) and ClO (2.6×10^{16} mol/cm^3), should pose no problem in the photodissociation experiment. Their photoproducts are readily identified as single sharp peaks in the time-of-flight spectra with arrival times easily calculated from known energetics and kinematics. Also, some of the unreacted ClO at the exit of the channel may dimerize in the supersonic expansion after the channel exit and contribute to the ClOOCl concentration in the interaction region. In supersonic expansions, weakly bound van der Waals dimers with binding energies of 1-3 kcal/mol can form even under mild expansion conditions, so the ClOOCl, bound by 16 kcal/mol, should easily form. The large binding energy of ClOOCl should allow us to create ClO dimers in the expansion without forming significant amounts of more weakly bound clusters.

The large density of Cl_2O (9.6×10^{15} mol/cm^3), however, may cause a more formidable problem. When Cl_2O photolyzes, the ClO fragment can possess internal energy. Thus, the contributions in the time-of-flight spectra from Cl_2O photoproducts are not so easily identified as those from diatomics. Our Cl_2O photolysis experiment at 308 nm, however, does provide us with the translational energy distributions for the Cl_2O photoproducts which should help us identify peaks resulting from Cl_2O and not ClOOCl.

Figure 4 shows the results for a starting mixture of 1.75% Cl_2O / 4% Cl_2 in helium and photolyzing with 355 nm radiation. The absorption cross section of Cl_2 at 355 nm is 1.6×10^{-19} cm^2, so 7 mJ/mm^2 per pulse are required in order to dissociate 20% of the Cl_2. The initial number of ClO molecules produced should be the same in this case as in the pure Cl_2O scenario presented above. Lower concentrations of Cl_2 require higher laser fluences to obtain the same yield of atomic chlorine. The fiber optics may not be able to handle the higher powers which is why the Cl_2 concentration was increased to 4%. At 7

mJ/mm^2 per pulse, 1.5% of the Cl_2O will also dissociate. As in the pure Cl_2O experiment, the majority of the atomic chlorine formed reacts within the first few microseconds after photolysis. At the exit of the channel, the ClOOCl density is 7.7 x 10^{15} mol/cm^3 which is almost seven time larger than the Cl_2O density (1.3 x 10^{15} mol/cm^3). The ClO density at the exit is 2.6 x 10^{16} mol/cm^3. Again ClO may dimerize in the ensuing supersonic expansion and contribute to the final ClOOCl concentration in the interaction region. The Cl_2 density is quite high but as mentioned earlier this should provide a minimal problem. All multi-atomic compounds other than Cl_2O have densities that are two to three orders of magnitude smaller than the ClOOCl density.

We also tried varying the Cl_2O/Cl_2 ratio and found that if the initial Cl_2O density was too low, ≤1%, very little ClO dimer formed. As the initial Cl_2O density increased the exit ClOOCl and Cl_2O densities also increased. The exit ClOOCl density increased faster than the Cl_2O density. Thus, by varying the initial amount of Cl_2O, we should be able to optimize the relative ratio of ClOOCl to Cl_2O at the channel exit to form sufficient amounts of ClOOCl with negligible residual Cl_2O.

The question now arises as to whether these channel densities are sufficient to produce reasonable signal in photodissociation experiment using the CMBA. The photodissociation signal will depend on the density in the interaction region and absorption cross section of ClOOCl. By comparing our results to the experimental conditions of the $ClONO_2$ experiment, we should be able to obtain some sense of the signal-to-noise ratio. The absorption cross section of ClOOCl at 308 nm (4.9 x 10^{-19}) is comparable to the cross section for $ClONO_2$ at 248 nm (4.6 x 10^{-19}). The center-line beam density n at a distance l from the source is

$$n(l) = \frac{n_o a\sqrt{2kT/m}}{\pi V_{term} l^2}$$

where n_0 is the stagnation density, a is the nozzle area, and V_{term} is the terminal beam velocity.[7] The $ClONO_2$ experimental conditions predict a $ClONO_2$ density in the interaction region of 2×10^{11} /cm^3 (see Table IV). Using the parameters for the ClOOCl source, a density of 4×10^{11} /cm^3 in the interaction region is predicted. This value is twice as high as the $ClONO_2$ density. Though the density of ClOOCl at the nozzle is an order of magnitude small less than the stagnation density of $ClONO_2$, the larger aperture of the pulsed valve compensates. The larger nozzle aperture is feasible because of the duty cycle advantage of the pulsed valve compared to the continuous source used in the $ClONO_2$ experiment. This calculation ignores any ClOOCl that may form in the supersonic expansion that occurs after the channel exit, and thus is a lower limit. If all of the remaining ClO dimerizes in the supersonic expansion, the ClOOCl beam density could be as high as 1.0×10^{12} /cm^3.

V. CONCLUSION

At this point, the majority of the construction for the ClOOCl source is completed. The testing chamber is assembled. All the chambers pump down to reasonable pressures and the quadrupole mass spectrometer has been revived. The extended nozzle has been designed and fabricated, and time-resolved gas pulses have been detected using the quadrupole mass spectrometer. Using the Peltier coolers, the nozzle can be cooled to 248 K which should be sufficient to create ClOOCl.

In order to complete testing on the ClOOCl source, an excimer laser or YAG laser with a tripling crystal must be acquired and coupled to the source. Additionally, a high-Q head that allows the mass spectrometer to detect out to m/e=102 must be procured so that the ClOOCl parent ion can be detected and ClOOCl densities determined.

The model calculations show that it is feasible to generate a molecular beam of ClOOCl by photolyzing Cl_2O/Cl_2/He mixtures in a channel. Thus, once the necessary components are appropriated, generating a molecular beam of ClO dimer should be trivial.

VI. REFERENCES

1. L.T. Molina, M.J. Molina, *J. Phys. Chem.* **91**, 433 (1987).

2. R.A. Cox, G.D. Hayman, *Nature* **332**, 796 (1988).

3. M.J. Molina, A.J. Colussi, L.T. Molina, R.N. Schindler, T.L. Tso, *Chem. Phys. Lett.* **173**, 310 (1990).

4. W.B. DeMore, S.P. Sander, D.M. Golden, R.F. Hampson, M.J. Kurylo, C.J. Howard, A.R. Ravishankara, C.E. Kolb, M.J. Molina, *Chemical Kinetics and Photochemical Data for Use in Stratospheric Modeling; Evaluation Number 10,* JPL Publication 92-10, Jet Propulsion Laboratory (1992).

5. D. Proch, T. Trickl, *Rev. Sci. Instrum.* **60**, 713 (1989).

6. S.P. Sander, R.R. Friedl, Y.L. Yung, *Science* **245**, 1095 (1989).

7. D. R. Miller, "Free Jet Sources," *Atomic and Molecular Beam Methods*, ed. G. Scoles, Oxford Univ. Press, New York (1988); 14-53.

TABLE I: Flow Conditions Used for Modeling the ClOOCl Source.

Channel Geometry:	Length	3.0 cm	
	Diameter	0.1 cm	
Vacuum Region Pumping:	Throughput	1×10^5 torr cm^3/s	
	Pressure	3×10^{-4} torr	
Stagnation Region:	Temperature	240 K	
	Pressure	385 torr	
Flow Parameters:	Reynolds Number	1500	
	Friction Coeff.	0.011	
	Entry Length	5 mm	
Channel Conditions:		Entrance	Exit
	Mach Number	0.25	1
	Pressure	355 torr	78 torr
	Temperature	236 K	181 K
	Flow Velocity	3×10^4 cm/s	1×10^5 cm/s
	He density	1.5×10^{19} /cm^3	4×10^{18} /cm^3

TABLE II: Calculated Number Densities for Various Initial Concentrations of Cl_2 and Cl_2O.

Cl_2O	1.00%	2.00%	1.00%	2.00%	1.00%	1.50%	1.75%	2.00%
Cl_2	0.00%	0.00%	2.00%	2.00%	4.00%	4.00%	4.00%	4.00%
wavelength	308 nm	308 nm	355 nm	355 nm	355 nm	355 nm	355 nm	355 nm
% dissociation	40% (Cl_2O)	40% (Cl_2O)	40% (Cl_2)	40% (Cl_2)	20% (Cl_2)	20% (Cl_2)	20% (Cl_2)	20% (Cl_2)
Number Densities at Channel Entrance (molecules/cm^3)								
He (356 Torr)	1.4E+19	1.4E+19	1.4E+19	1.4E+19	1.4E+19	1.4E+19	1.4E+19	1.4E+19
Cl_2	0.00	0.00	2.9E+17	2.9E+17	5.8E+17	5.8E+17	5.8E+17	5.8E+17
Cl_2O	1.5E+17	2.9E+17	1.5E+17	2.9E+17	1.5E+17	2.2E+17	2.6E+17	2.9E+17
ClOOCl	0.00	0.00	0.00	0.00	0.00	0.00	0.00	0.00
ClO	0.00	0.00	0.00	0.00	0.00	0.00	0.00	0.00
Cl	0.00	0.00	0.00	0.00	0.00	0.00	0.00	0.00
ClOO	0.00	0.00	0.00	0.00	0.00	0.00	0.00	0.00
OClO	0.00	0.00	0.00	0.00	0.00	0.00	0.00	0.00
Cl_2O_3	0.00	0.00	0.00	0.00	0.00	0.00	0.00	0.00
Number Densities at Channel Exit (molecules/cm^3)								
He (73.5 Torr)	3.4E+18	3.0E+18	3.0E+18	3.0E+18	3.0E+18	3.0E+18	3.0E+18	2.9E+18
Cl_2	1.4E+16	2.8E+16	8.0E+16	9.4E+16	1.4E+17	1.6E+17	1.6E+17	1.6E+17
Cl_2O	6.4E+15	9.6E+15	1.3E-69	6.6E+15	6.4E-66	9.3E-01	1.3E+15	8.6E+15
ClOOCl	5.8E+15	9.3E+15	2.0E+13	1.2E+16	2.1E+13	3.9E+14	7.7E+15	1.1E+16
ClO	1.5E+16	2.6E+16	1.9E+16	2.6E+16	1.9E+16	2.4E+16	2.6E+16	2.6E+16
Cl	1.1E+12	4.5E+12	9.8E+15	5.0E+12	9.3E+15	7.9E+14	2.3E+13	3.8E+12
ClOO	4.3E+12	1.0E+13	7.5E+12	1.8E+13	7.7E+12	5.5E+13	4.9E+13	1.4E+13
OClO	1.1E+13	4.0E+13	1.9E+11	3.3E+13	2.0E+11	3.6E+12	2.9E+13	3.4E+13
Cl_2O_3	1.8E+13	1.2E+14	1.2E+12	1.1E+14	1.3E+12	1.4E+13	9.4E+13	1.1E+14

TABLE III: Calculated Mole Fractions for Various Initial Concentrations of Cl_2 and Cl_2O.

Cl_2O	1.00%	2.00%	1.00%	2.00%	1.00%	1.50%	1.75%	2.00%
Cl_2	0.00%	0.00%	2.00%	2.00%	4.00%	4.00%	4.00%	4.00%
wavelength	308 nm	308 nm	355 nm	355 nm	355 nm	355 nm	355 nm	355 nm
% dissociation	40% (Cl_2O)	40% (Cl_2O)	40% (Cl_2)	40% (Cl_2)	20% (Cl_2)	20% (Cl_2)	20% (Cl_2)	20% (Cl_2)
Mole Fractions at Channel Exit (molecules/cm^3)								
Cl_2	0.0042	0.0094	0.025	0.030	0.045	0.051	0.050	0.049
Cl_2O	0.0019	0.0032	4.1E-88	0.0021	2.1E-84	3.0E-19	4.1E-04	0.0027
ClOOCl	0.0017	0.0031	6.3E-06	0.0037	6.6E-06	1.2E-04	0.0024	0.0036
ClO	0.0044	0.0087	0.0061	0.0083	0.0061	0.0076	0.0081	0.0082
Cl	3.2E-07	1.5E-06	0.0031	1.6E-06	0.0030	2.5E-04	7.4E-06	1.2E-06
ClOO	1.3E-06	3.4E-06	2.4E-06	5.7E-06	2.5E-06	1.7E-05	1.6E-05	4.6E-06
OClO	3.2E-06	1.3E-05	6.0E-08	1.1E-05	6.4E-08	1.1E-06	9.2E-06	1.1E-05
Cl_2O_3	5.4E-06	3.9E-05	3.9E-07	3.6E-05	4.0E-07	4.4E-06	3.0E-05	3.4E-05

TABLE IV: Molecular Beam Conditions for the Continuous $ClONO_2$ Source and the Pulsed ClOOCl Source.

	$ClONO_2$	ClOOCl
n_0 (He stagnation density)	6.8×10^{18} /cm^3 (193 torr)	3.0×10^{18} /cm^3
n_0 ($ClONO_2$ or ClOOCl)	2.3×10^{17} /cm^3 (6.7 torr)	7.7×10^{15} /cm^3
a, aperture area	8×10^{-5} cm^2	8×10^{-3} cm^2
T_0, stagnation temperature	278 K	248 K
l, distance from nozzle	4.8 cm	6 cm
$n(l)$, beam density	2×10^{11} /cm^3	4×10^{11} /cm^3
V_{term}	10^5 cm/s	10^5 cm/s

VII. FIGURE CAPTIONS

Figure 1. Schematic of the extended nozzle for the ClOOCl dimer source.

Figure 2. Schematic of the testing chamber for the ClOOCl dimer source constructed at Caltech.

Figure 3. Mole fractions of some key species for 2.00% Cl2O seeded in helium. Photolysis occurs at 17.5 μs which corresponds to a travel distance of 5 mm down the channel. The end of the curves (73.5 μs) correspond to the end of the channel. Flow conditions are listed in Table I.

Figure 4. Mole fractions of some key species for 1.75% Cl2O / 4.00% Cl2 mixture seeded in helium. Photolysis occurs at 17.5 μs which corresponds to a travel distance of 5 mm down the channel. The end of the curves (73.5 μs) correspond to the end of the channel. Flow conditions are listed in Table I.

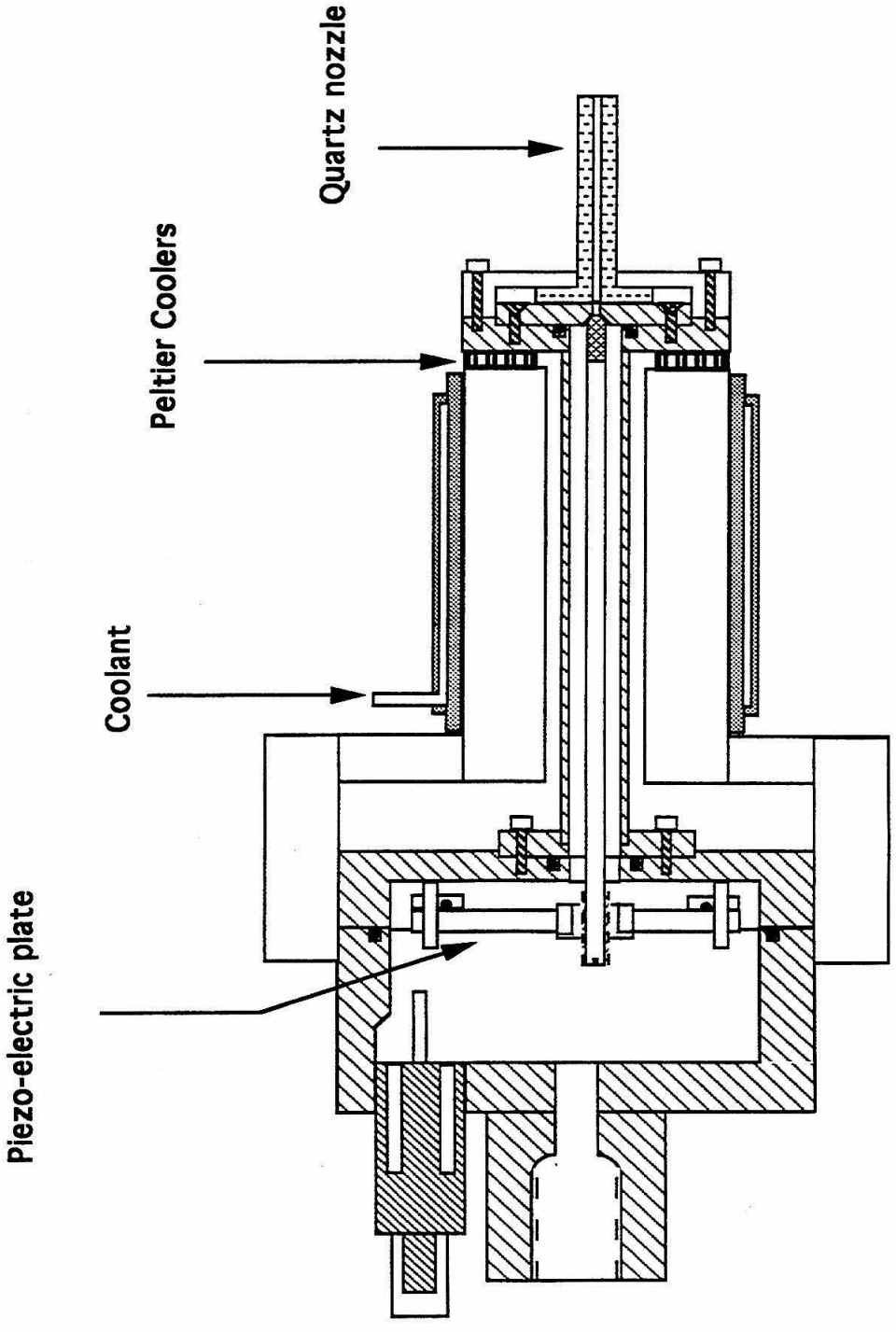
Quartz nozzle
Peltier Coolers
Coolant
Piezo-electric plate

Figure 1

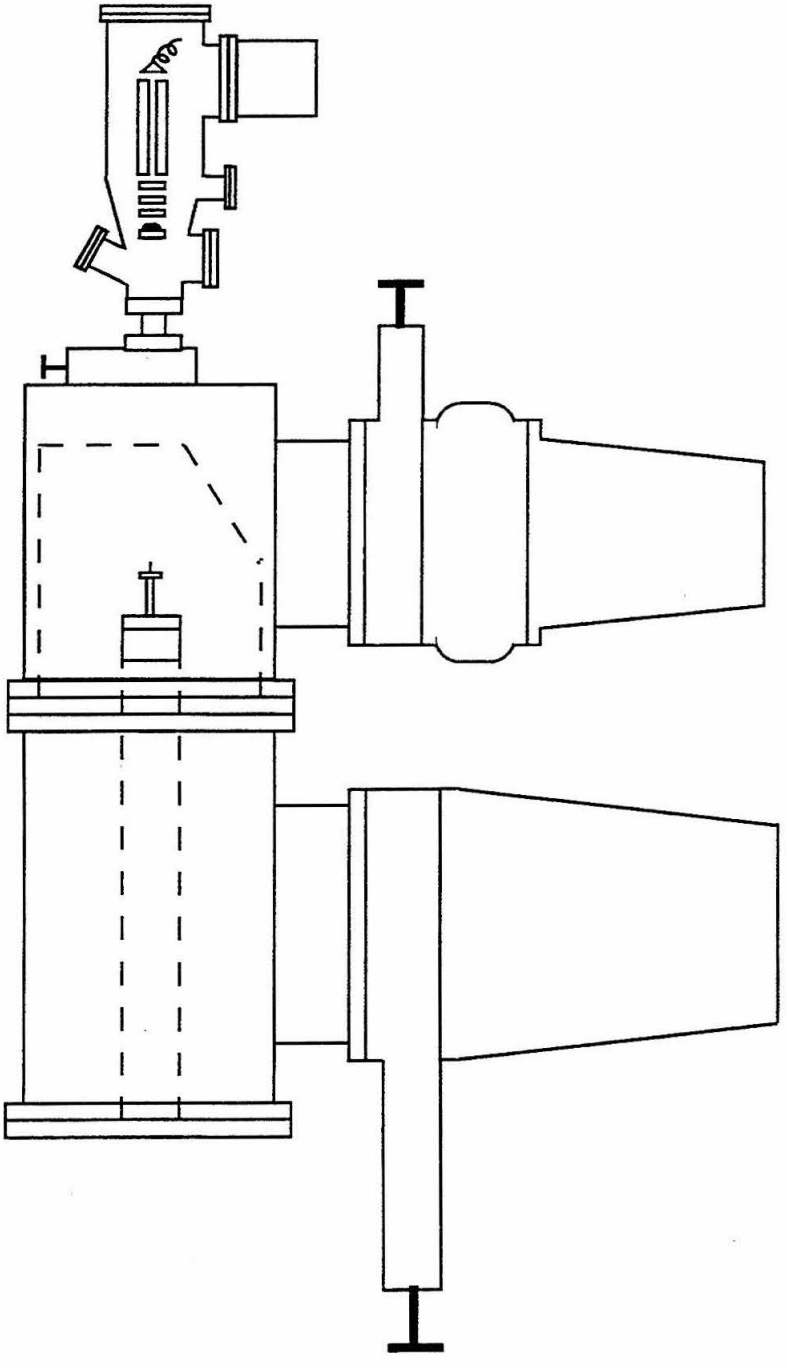

Figure 2

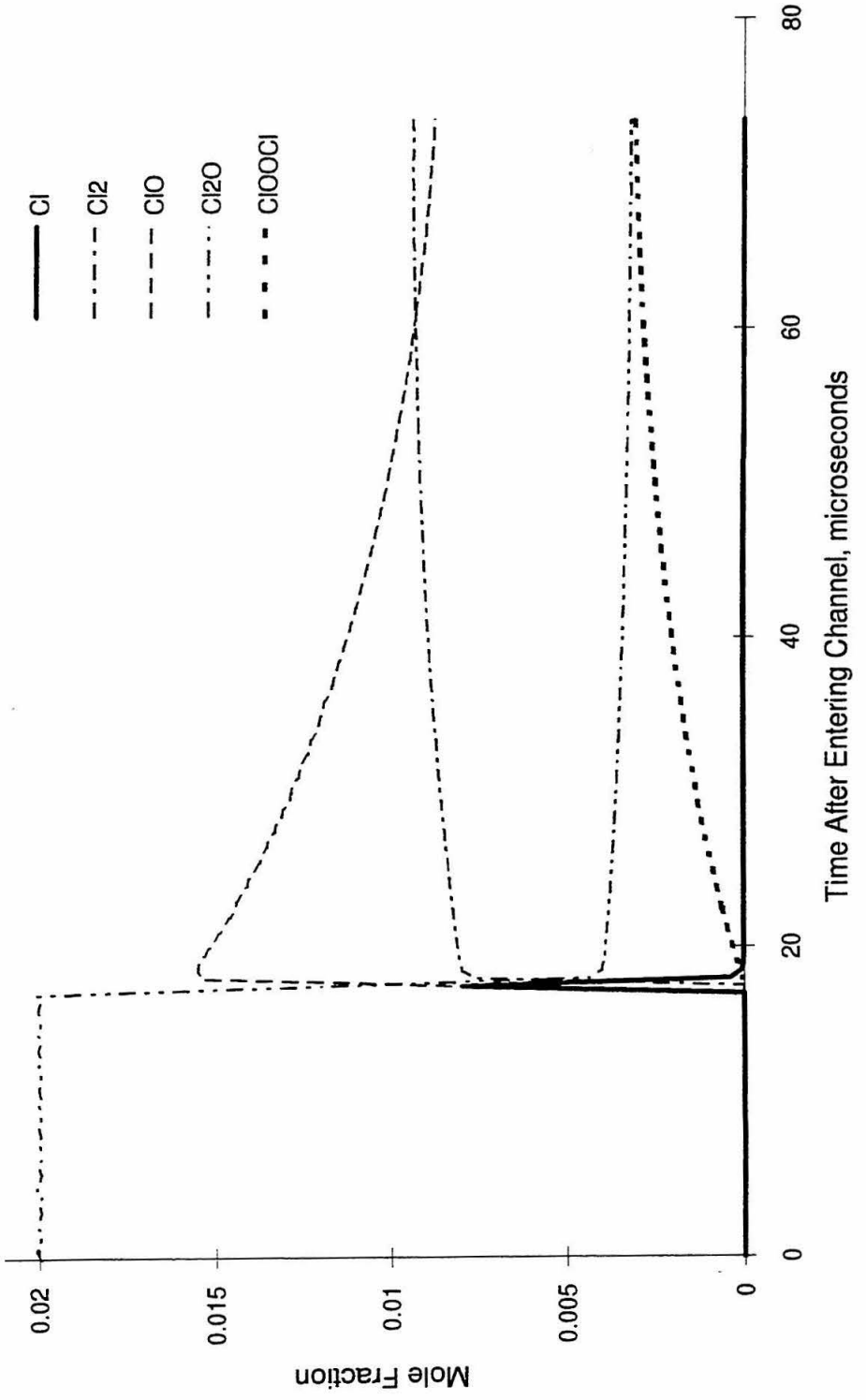
Cl
Cl2
ClO
Cl2O
ClOOCl
Mole Fraction
0.02
0.015
0.01
0.005
0
0
20
40
60
80
Time After Entering Channel, microseconds

Figure 3

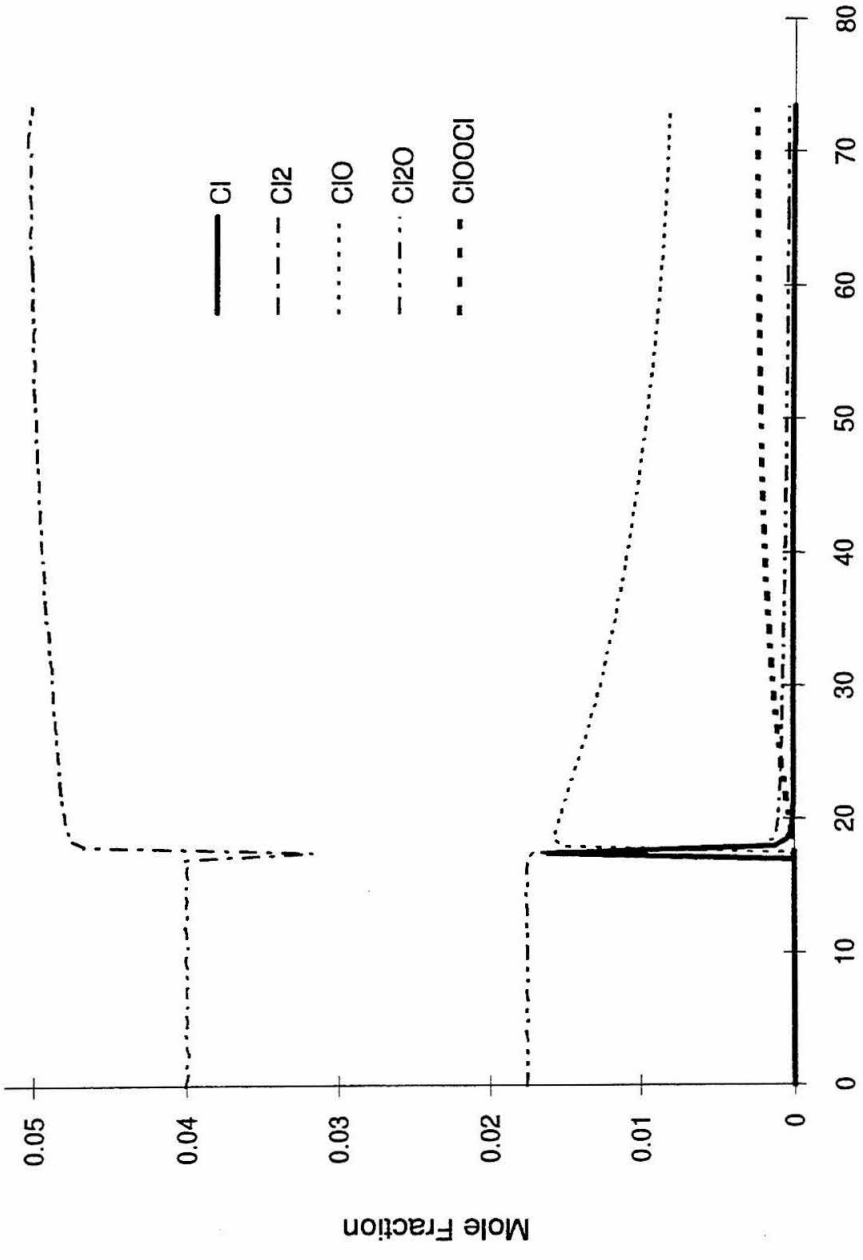
Cl
Cl2
ClO
Cl2O
ClOOCl
Mole Fraction
0.05
0.04
0.03
0.02
0.01
0
0
10
20
30
40
50
60
70
80
Time After Entering Channel, microseconds

Figure 4

APPENDIX A

I. Fitting Routine for the Water Cluster/$ClONO_2$ Experiment

When a protonated water cluster collides with a chlorine nitrate molecule two processes are possible; either the $ClONO_2$ can react with a water molecule in the ion cluster to form $NO_2^+(H_2O)_m$ or the water cluster can absorb the collisional energy and dissociate to form $H_3O^+(H_2O)_{n-1}$,

$$ClONO_2 + H_3O^+(H_2O)_n \longrightarrow NO_2^+(H_2O)_m + ClOH + (n\text{-}m)H_2O$$
$$\longrightarrow H_2O^+(H_2O)_{n-1} + ClONO_2 + H_2O$$

To better quantify the relative contributions from these two processes, the appearance rates for various products were investigated. Integrated peak intensities were normalized by dividing by the total ion count and then plotted versus the $ClONO_2$ pressure in the reaction region. Compiled data and plots are presented in Table I and Figures 1-11. These curves were then fit using the equation

$$[C^+] = [C^+]_0 e^{-k_c P_{ClONO_2}} + \frac{[A^+]_0 k_a k_b}{(k_c - k_a)(k_b - k_a)}\left(e^{-k_a P_{ClONO_2}} - e^{-k_c P_{ClONO_2}}\right)$$
$$+ \left[\frac{[B^+]_0 k_b}{k_c - k_b} - \frac{[A^+]_0 k_a k_b}{(k_c - k_b)(k_b - k_a)}\right]\left(e^{-k_b P_{ClONO_2}} - e^{-k_c P_{ClONO_2}}\right) \quad (1)$$

which is derived by assuming a cascading reaction $A^+ \xrightarrow{k_a} B^+ \xrightarrow{k_b} C^+ \xrightarrow{k_c} D^+$; a description of the derivation is presented here.

The initial reaction is assumed to be $A^+ + ClONO_2 \xrightarrow{k_1} B^+ + N$, where A^+ is a parent water cluster [$H_3O^+(H_2O)_n$], B^+ is a product ion [either $H_3O^+(H_2O)_{n-1}$ or $NO_2^+(H_2O)_m$], and N is a neutral product. The loss rate of A^+ in the reaction cell is given

by

$$\frac{d[A^+]}{dz} = -k_1 P_{ClONO_2}[A^+] \tag{2}$$

where $[A^+]$ is the concentration of A^+, P_{ClONO_2} is the pressure of $ClONO_2$ in the reaction region, z is the distance traveled through the reaction chamber and k_1 is the reaction rate coefficient.[1] Integrating equation 1 yields

$$[A] = [A]_0 e^{-k_a P_{ClONO_2}} \tag{3}$$

where $k_a = k_1 z$ and $[A^+]_0$ is the concentration of A^+ at the entrance to the reaction chamber. If B^+ then goes on to collide with a second $ClONO_2$ molecule, its concentration gradient is described by the equation

$$\frac{d[B^+]}{dz} = k_1 P_{ClONO_2}[A^+] - k_2 P_{ClONO_2}[B^+], \tag{4}$$

where $[B^+]$ is the concentration of B^+, and k_2 is the rate coefficient for the reaction $B^+ + ClONO_2 \xrightarrow{k_2} C^+ + N$. Replacing $[A^+]$ with equation 3 and rearranging the equation leads to the expression

$$\frac{d[B^+]}{dz} + k_2 P_{ClONO_2}[B^+] = k_1 P_{ClONO_2}[A]_0 e^{-k_1 z P_{ClONO_2}} \tag{5}$$

which when solved gives an expression for $[B^+]$

$$[B^+] = \left[[B^+]_0 - \frac{k_a[A^+]}{k_b - k_a}\right] e^{-k_b P_{ClONO_2}} + \left[\frac{k_a[A^+]_0}{k_b - k_a}\right] e^{-k_a P_{ClONO_2}}, \tag{6}$$

where $k_b = k_2 z$. A similar expression describes the concentration gradient of $[C^+]$ in the cell

$$\frac{d[C^+]}{dz} = k_b P_{ClONO_2}[B^+] - k_c P_{ClONO_2}[C^+] \tag{7}$$

which rearranges to give

$$\frac{d[C^+]}{dz} + k_c P_{ClONO_2}[C^+] = k_b\left[[B^+]_o - \frac{k_a[A^+]}{k_b - k_a}\right]e^{-k_b P_{ClONO_2}} + k_b\left[\frac{k_a[A^+]_o}{k_b - k_a}\right]e^{-k_a P_{ClONO_2}} \quad (8)$$

and is solved to yield equation 1.

The curves for various products were fit using equation 1. If at a specific mass no peak was present at $P_{ClONO_2} = 0$ torr, $[C^+]_o$ was set to zero, and for small clusters, $H_3O^+(H_2O)_n$ $n = 2,3$ or 4 and $NO_2^+(H_2O)_m$ $m = 0,1$ or 2, $[B^+]_o$ was also set at zero. The rest of the parameters were allowed to float until χ^2 reached a minimum at which point the fit was terminated and values reported (see Table II). The resultant values were highly dependent on what input parameters were used as initial guesses (compare Runs C and D for Mass 55). For the $NO_2^+(H_2O)_m$ curves, two sets of starting parameters were used; one for the three A runs and another for the three B runs.

Since a variety of fitting parameters could provide equally good fits, the quantitative information that could be obtained from our fits was ignored and we decided to only look at the qualitative value of our results. If quantitative values are wanted, the experiment should be repeated in a more controlled environment, ideally a selected ion flow tube. If one wishes to repeat the experiment using our current set-up, a deceleration region prior to the reaction chamber is suggested, in order to decrease and more accurately define the collision energy. The experiment would also benefit from a more stable protonated water cluster source which has subsequently been developed in our group.

II. Determining the Pressure in Reaction Region

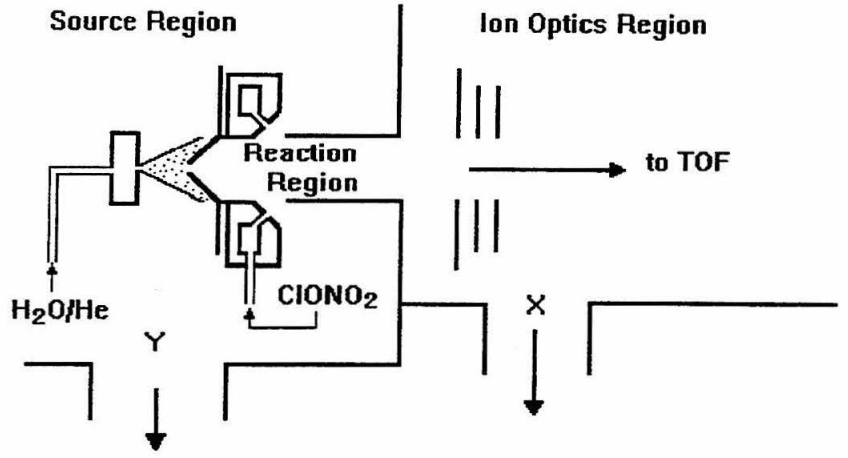

We did not measure the $ClONO_2$ pressure in the reaction region directly but rather determined it from the increase in pressure in the source region. The gas load on the source region was from both the effusion out of the higher pressured reaction region and from gas exiting the injection nozzle which did not enter the reaction region, Z.

$$\frac{P_{reac}A_{source}}{(2\pi mkT)^{1/2}} + Z = Y[P_{source} - P^{o}_{source}] \qquad (9)$$

Y = pumping speed in the source region.

P_{source} = pressure in the source region.

P^{o}_{source} = pressure in the source region with $ClONO_2$ off.

P_{reac} = pressure in the reaction region.

A_{source} = total area of the apertures between the reaction and source region.

m = mass of $ClONO_2$ (97.46 amu).

k = Boltzman's constant.

T = temperature (293 K).

This equation has two unknowns, Z and P_{reac}. Thus, in order to determine P_{reac}, the pressure difference in the ion optics region must be measured. Here the only gas-load on the region is the result of gas effusion from the reaction region and can be described using the following equation,

$$\frac{P_{reac}A_{optics}}{(2\pi mkT)^{1/2}} = X[P_{optics} - P^{o}_{optics}]. \quad (10)$$

X = pumping speed in the ion optics region (1200 l/s).

P_{optics} = pressure in the ion optics region.

P^{o}_{optics} = pressure in the ion optics region with $ClONO_2$ off.

A_{optics} = aperature area between the reaction and ion optics region ($1.27cm^2$).

In this equation, only P_{reac} is unknown. Thus, the pressure in the reaction region could be determined by knowing only the pressure in the ion optics region.

Unfortunately, when the data was recorded the pressure in the ion optics region was not recorded. Thus, in order to determine the pressure in the reaction chamber from the pressure increase in the source region, a series of pressure measurements were taken subsequent to the experiment which recorded the pressure increase in the source region and the ion optics region for various pressures of $ClONO_2$ in the reaction region (see Table III). The following expression describes the relationship between the pressures in the three regions,

$$[P_{optics} - P^{o}_{optics}] = \frac{YA_{optics}}{XA_{source}}[P_{source} - P^{o}_{source}] + \frac{ZA_{optics}}{XA_{source}} = \frac{P_{reac}A_{optics}}{X(2\pi mkT)^{1/2}}. \quad (11)$$

Since X, Y, Z, A_{optics} and A_{source} are all constants, plotting the pressure increase in the source region versus the pressure increase in the optics region resulted in a straight line with a slope (j) of

$$j = \frac{YA_{optics}}{XA_{source}} \quad (12)$$

and a y-intercept (k) of

$$k = \frac{ZA_{optics}}{XA_{source}},$$

(13)

which was fit using a linear least squared regression. An expression relating the pressure in the source region to the pressure in the reaction region was then derived

$$P_{reac} = \frac{X(2\pi mkT)^{1/2}}{A_{optics}} \cdot (j[P_{source} - P^{o}_{source}] + k). \qquad (14)$$

P_{reac} values calculated from P_{source} values are presented in Table IV.

III. References

1. D. Smith, N.G. Adams, *In "Gas Phase Ion Chemistry, Vol. 1,"* Academic Press, Orlando, FL (1979); 1-44.

TABLE I: Integrated Peak Intensities

$ClONO_2$ Pressure in Reaction Region (mtorr)	Total Integrated Peak Intensity	Mass 55	Normalized Mass 55	Mass 73	Normalized Mass 73
0.000	121962	101	8.3×10^{-4}	148	0.001
0.000	121863	102	8.4×10^{-4}	149	0.001
0.161	491753	22	4.5×10^{-5}	18	3.7×10^{-5}
0.161	491035	23	4.7×10^{-5}	18	3.7×10^{-5}
0.161	491364	23	4.7×10^{-5}	17	3.5×10^{-5}
0.482	62093	178	0.003	365	0.006
1.446	83594	575	0.007	1680	0.020
2.409	83553	577	0.007	1672	0.020
3.373	229953	1426	6.2×10^{-3}	4268	0.019
3.855	55346	1843	0.033	3196	0.058
4.658	199632	3962	0.020	9844	0.049
4.819	28097	2622	0.093	5210	0.185
4.980	183884	6829	0.037	17190	0.093
5.943	125874	5077	0.040	19745	0.157
6.586	114530	6354	0.056	16394	0.143
7.228	28058	2739	0.098	5190	0.185
7.389	72226	4021	0.056	13841	0.192
8.031	36437	2205	0.061	6792	0.186
8.031	51195	4071	0.080	11959	0.234
8.031	52153	5083	0.097	13149	0.252
8.192	41752	2662	0.064	8783	0.210
8.513	17250	1702	0.099	2432	0.141
8.835	33092	2864	0.087	6886	0.208
9.959	6562	364	0.056	406	0.062

TABLE I (continued):

$ClONO_2$ Pressure (mtorr)	Mass 91	Normalized Mass 91	Mass 109	Normalized Mass 109	Mass 127	Normalized Mass 127
0.000	397	0.003	1003	0.008	1984	0.016
0.000	397	0.003	1002	0.008	1982	0.016
0.161	69	1.4×10^{-4}	407	8.3×10^{-4}	3192	0.006
0.161	69	1.4×10^{-4}	406	8.3×10^{-4}	3181	0.006
0.161	67	1.4×10^{-4}	403	8.2×10^{-4}	3185	0.006
0.482	447	0.007	630	0.010	1019	0.016
1.446	2122	0.025	2489	0.030	2482	0.030
2.409	2121	0.025	2475	0.030	2465	0.030
3.373	5304	0.023	6864	0.030	7325	0.032
3.855	1446	0.026	882	0.016	624	0.011
4.658	8172	0.041	8185	0.041	7922	0.040
4.819	1837	0.065	883	0.031	467	0.017
4.980	13510	0.073	10640	0.058	8555	0.047
5.943	12420	0.099	8112	0.064	5409	0.043
6.586	8729	0.076	5775	0.050	3717	0.032
7.228	1734	0.062	827	0.029	458	0.016
7.389	7159	0.099	3551	0.049	1809	0.025
8.031	3690	0.101	2111	0.058	1162	0.032
8.031	5769	0.113	2768	0.054	1265	0.025
8.031	5186	0.099	2192	0.042	930	0.018
8.192	4429	0.106	2298	0.055	1215	0.029
8.513	680	0.039	336	0.019	188	0.011
8.835	3021	0.091	1536	0.046	766	0.023
9.959	127	0.019	85	0.013	33	0.005

TABLE I (continued):

$ClONO_2$

Pressure (mtorr)	Mass 181	Normalized Mass 181	Mass 199	Normalized Mass 199	Mass 217	Normalized Mass 217
0.000	8549	0.070	10687	0.088	10926	0.090
0.000	8526	0.070	10654	0.087	10933	0.090
0.161	18438	0.037	27068	0.055	32624	0.066
0.161	18378	0.037	26973	0.055	32500	0.066
0.161	18365	0.037	26973	0.055	32520	0.066
0.482	4802	0.077	6194	0.100	5964	0.096
1.446	4969	0.059	6001	0.072	5530	0.066
2.409	4959	0.059	6148	0.074	5515	0.066
3.373	11385	0.057	13384	0.067	13124	0.066
3.855	513	0.009	483	0.009	421	0.008
4.658	10096	0.051	10580	0.053	8963	0.045
4.819	248	0.009	232	0.008	161	0.006
4.980	6914	0.038	6697	0.036	5288	0.029
5.943	4365	0.035	4161	0.033	3161	0.025
6.586	2842	0.025	2647	0.023	1986	0.017
7.228	253	0.009	234	0.008	163	0.006
7.389	1363	0.019	1213	0.017	961	0.013
8.031	682	0.019	622	0.017	456	0.013
8.031	629	0.012	518	0.010	363	0.007
8.031	450	0.009	404	0.008	264	0.005
8.192	598	0.014	472	0.011	331	0.008
8.513	90	0.005	80	0.005	63	0.004
8.835	366	0.011	318	0.010	221	0.007
9.959	21	0.003	26	0.004	13	0.002

TABLE I (continued):

$ClONO_2$ Pressure (mtorr)	Mass 46	Normalized Mass 46	Mass 64	Normalized Mass 64	Mass 82	Normalized Mass 82
0.000	0	0.000	0	0.000	0	0.000
0.000	0	0.000	0	0.000	0	0.000
0.161	0	0.000	0	0.000	0	0.000
0.161	0	0.000	0	0.000	0	0.000
0.161	0	0.000	0	0.000	0	0.000
0.482	77	0.001	0	0.000	0	0.000
1.446	178	0.002	59	7.1×10^{-4}	18	2.2×10^{-4}
2.409	147	0.002	63	7.5×10^{-4}	20	2.4×10^{-4}
3.373	369	0.002	191	8.3×10^{-4}	113	4.9×10^{-4}
3.855	1043	0.019	229	0.004	205	0.004
4.658	1424	0.007	538	0.003	210	0.001
4.819	1096	0.039	335	0.012	207	0.007
4.980	2370	0.013	374	0.002	385	0.002
5.943	1097	0.009	515	0.004	439	0.003
6.586	2331	0.020	799	0.007	476	0.004
7.228	1094	0.039	310	0.011	210	0.007
7.389	1063	0.015	425	0.006	363	0.005
8.031	524	0.014	252	0.007	37	0.001
8.031	883	0.017	316	0.006	271	0.005
8.031	1129	0.022	402	0.008	253	0.005
8.192	613	0.015	166	0.004	92	0.002
8.513	891	0.052	226	0.013	131	0.008
8.835	731	0.022	103	0.003	61	0.002
9.959	303	0.046	86	0.013	31	0.005

TABLE II: Fitting Parameters for Pressure versus Integrated Peak Intensity Plots

	k_a	k_b	k_c	A_o	B_o	C_o	χ^2
$H_3O^+(H_2O)_2$							
mass 55 - Run A	103	104	113	0.4853	0.0000	0.0000	0.0044669
- Run B	114	105	134	0.4744	0.0000	0.0000	0.0044390
- Run C	119	95	150	0.5205	0.0000	0.0000	0.0044389
- Run D	21	202	164	1.3983	0.0000	0.0000	0.0044859
- Run E	30	207	126	0.9041	0.0000	0.0000	0.0044816
- Run F	162	92	119	0.3652	0.0000	0.0000	0.0044681
$H_3O^+(H_2O)_3$							
mass 73 - Run A	175	149	172	0.7898	0.0000	0.0000	0.0383503
- Run B	174	185	186	0.7147	0.0000	0.0000	0.0380812
- Run C	156	227	160	0.6487	0.0000	0.0000	0.0381369
- Run D	195	140	225	0.8772	0.0000	0.0000	0.0381604
- Run E	226	135	190	0.7666	0.0000	0.0000	0.0381660
$H_3O^+(H_2O)_4$							
mass 91 - Run A	185	216	272	0.4072	0.0000	0.0000	0.0109037
- Run B	227	192	255	0.3788	0.0000	0.0000	0.0108823
- Run C	240	143	310	0.4898	0.0000	0.0000	0.0109535
- Run D	226	188	259	0.3882	0.0000	0.0000	0.0108860
- Run E	345	64	335	0.7809	0.0000	0.0000	0.0112404

TABLE II: (Continued)

$H_3O^+(H_2O)_5$							
mass 109 - Run A	343	322	460	0.2364	0.0836	0.0051	0.0024279
- Run B	342	361	404	0.2060	0.0000	0.0051	0.0024222
- Run C	411	255	411	0.2012	0.0196	0.0041	0.0024454
- Run D	357	328	414	0.2077	0.0049	0.0046	0.0024253
- Run E	355	345	408	0.2084	0.0000	0.0050	0.0024225
$H_3O^+(H_2O)_6$							
mass 127 - Run A	462	526	445	0.1320	0.0000	0.0119	0.0008589
- Run B	596	583	278	0.0707	0.0144	0.0102	0.0009197
- Run C	527	483	460	0.1446	0.0000	0.0125	0.0008545
- Run D	448	499	480	0.1438	0.0000	0.0118	0.0008584
- Run E	490	480	482	0.1453	0.0000	0.0122	0.0008542
- Run F	639	636	284	0.0859	0.0000	0.0114	0.0008896
$H_3O^+(H_2O)_9$							
mass 181 - Run A	0	1297	227	0	0.0415	0.0505	0.0027727
- Run B	0	0	146	0	0	0.0608	0.0037394
- Run C	0	1444	146	0	0.0136	0.0541	0.0034096
- Run D	0	420	407	0	0.0107	0.0516	0.0023968
$H_3O^+(H_2O)_{10}$							
mass 199 - Run A	0	211	1297	0	0.5422	0.0709	0.0033513
- Run B	0	0	182	0	0	0.0798	0.0042800
- Run C	0	1596	182	0	0.0174	0.0719	0.0038302
- Run D	0	471	446	0	0.1237	0.0695	0.0025917

TABLE II: (Continued)

	k_a	k_b	k_c	A_o	B_o	C_o	χ^2
$H_3O^+(H_2O)_{11}$							
mass 217 - Run A	0	0	220	0	0	0.0846	0.0024480
NO_2^+							
mass 46 - Run A	40	31	0	0.7565	0.0000	0.0000	0.0014705
- Run B	106	6	0	1.6574	0.0000	0.0000	0.0014842
$NO_2^+(H_2O)$							
mass 64 - Run A	42	33	0	0.2046	0.0000	0.0000	----
- Run B	106	4	0	0.7495	0.0000	0.0000	----
$NO_2^+(H_2O)_2$							
mass 82 - Run A	40	32	0	0.2046	0.0000	0.0000	0.0000617
- Run B	106	3	0	0.7495	0.0000	0.0000	0.0000608

TABLE III: Determining the Relationship Between the Pressure in the Ion Optics Region and the Pressure in the Source Region.

P_{source}	P_{optics}	P_{optics}-P^{o}_{optics}	P_{source}-P^{o}_{source}	Fit
1.7E-05	2.1E-06	5.0E-07	3.0E-06	2.7E-06
2.1E-05	4.1E-06	2.5E-06	7.0E-06	6.6E-06
4.3E-05	3.4E-05	3.2E-05	2.9E-05	2.8E-05
6.3E-05	4.1E-05	3.9E-05	4.9E-05	4.7E-05
7E-05	5.4E-05	5.2E-05	5.6E-05	5.4E-05
5.4E-05	3.9E-05	3.7E-05	4.0E-05	3.9E-05
4E-05	3.1E-05	2.9E-05	2.6E-05	2.5E-05
3.6E-05	2.8E-05	2.6E-05	2.2E-05	2.1E-05
3.0E-05	1.6E-05	1.4E-05	1.6E-05	1.5E-05
3.7E-05	2.3E-05	2.1E-05	2.3E-05	2.2E-05
4.8E-05	3.4E-05	3.2E-05	3.4E-05	3.3E-05
5.9E-05	4.9E-05	4.7E-05	4.5E-05	4.3E-05
2.7E-05	1.6E-05	1.4E-05	1.3E-05	1.2E-05
1.6E-05	3.6E-06	2.0E-06	2.0E-06	1.7E-06
2.4E-05	8.6E-06	7.0E-06	1.0E-05	9.5E-06
3E-05	1.5E-05	1.3E-05	1.6E-05	1.5E-05
4.7E-05	2.8E-05	2.6E-05	3.3E-05	3.2E-05
7.5E-05	6.5E-05	6.3E-05	6.1E-05	5.9E-05
1.4E-05	2.1E-06	5.0E-07	0.0	-2.1E-07
1.4E-05	2.1E-06	5.0E-07	0.0	-2.1E-07
1.4E-05	1.6E-06	0.0	0.0	-2.1E-07
1.4E-05	1.6E-06	0.0	0.0	-2.1E-07

P^{o}_{optics} = 1.6E-06

P^{o}_{source} = 1.4E-05

Regression Output:

Slope (j)	0.969915
Constant (k)	-2.1E-07
Std Err of Y Est	3.49E-06
R Squared	0.967889
No. of Observations	21
Degrees of Freedom	19
Std Err of Coef.	0.040529

TABLE IV. Calculation to Determine the Pressure in the Reaction Region from the Pressure in the Source Region.

P_{source} (torr)	P_{reac} (torr)
3.2E-05	0.000161
3.2E-05	0.000161
3.2E-05	0.000161
8.1E-05	0.008031
8.6E-05	0.008835
8.2E-05	0.008192
8.1E-05	0.008031
8.1E-05	0.008031
7.7E-05	0.007389
6.8E-05	0.005943
6.2E-05	0.004980
5.2E-05	0.003373
6.0E-05	0.004658
7.2E-05	0.006586
9.3E-05	0.009959
8.4E-05	0.008513
7.6E-05	0.007228
6.1E-05	0.004819
5.5E-05	0.003855
4.6E-05	0.002409
4.0E-05	0.001446
3.4E-05	0.000482
3.0E-05	0
2.8E-05	0

Equation: $P_{react} = 160.8(P_{source}\text{-}3.1\text{E-}5)$

$$\frac{X(2\pi mkT)^{1/2}}{A_{optics}} = \frac{(1200\,\text{l/s})(6.411 \times 10^{-23}\ \text{kg}\cdot\text{m/s})}{(1.27 \times 10^{-4}\ \text{m}^2)}$$

$$\otimes \frac{3.54 \times 10^{19}\ \text{molec}}{\text{torr}\cdot\text{l}} \cdot \frac{760\,\text{torr}}{1.01325 \times 10^{5}\ \text{N/m}^2} = 160.8$$

IV. Figure Captions

Figure 1. The normalized integrated peak intensities of the mass 55 data (•) plotted versus the $ClONO_2$ pressure in the reaction region. The lines correspond to fits calculated using equation 1 with the input parameters presented in Table II.

Figure 2. Mass 73 [$H_3O^+(H_2O)_3$] data and fits.

Figure 3. Mass 91 [$H_3O^+(H_2O)_4$] data and fits.

Figure 4. Mass 109 [$H_3O^+(H_2O)_5$] data and fits.

Figure 5. Mass 127 [$H_3O^+(H_2O)_6$] data and fits.

Figure 6. Mass 181 [$H_3O^+(H_2O)_9$] data and fits.

Figure 7. Mass 199 [$H_3O^+(H_2O)_{10}$] data and fits.

Figure 8. Mass 217 [$H_3O^+(H_2O)_{11}$] data and fits.

Figure 9. Mass 46 [NO_2^+] data and fits.

Figure 10. Mass 64 [$NO_2^+(H_2O)$] data and fits.

Figure 11. Mass 82 [$NO_2^+(H_2O)_2$] data and fits.

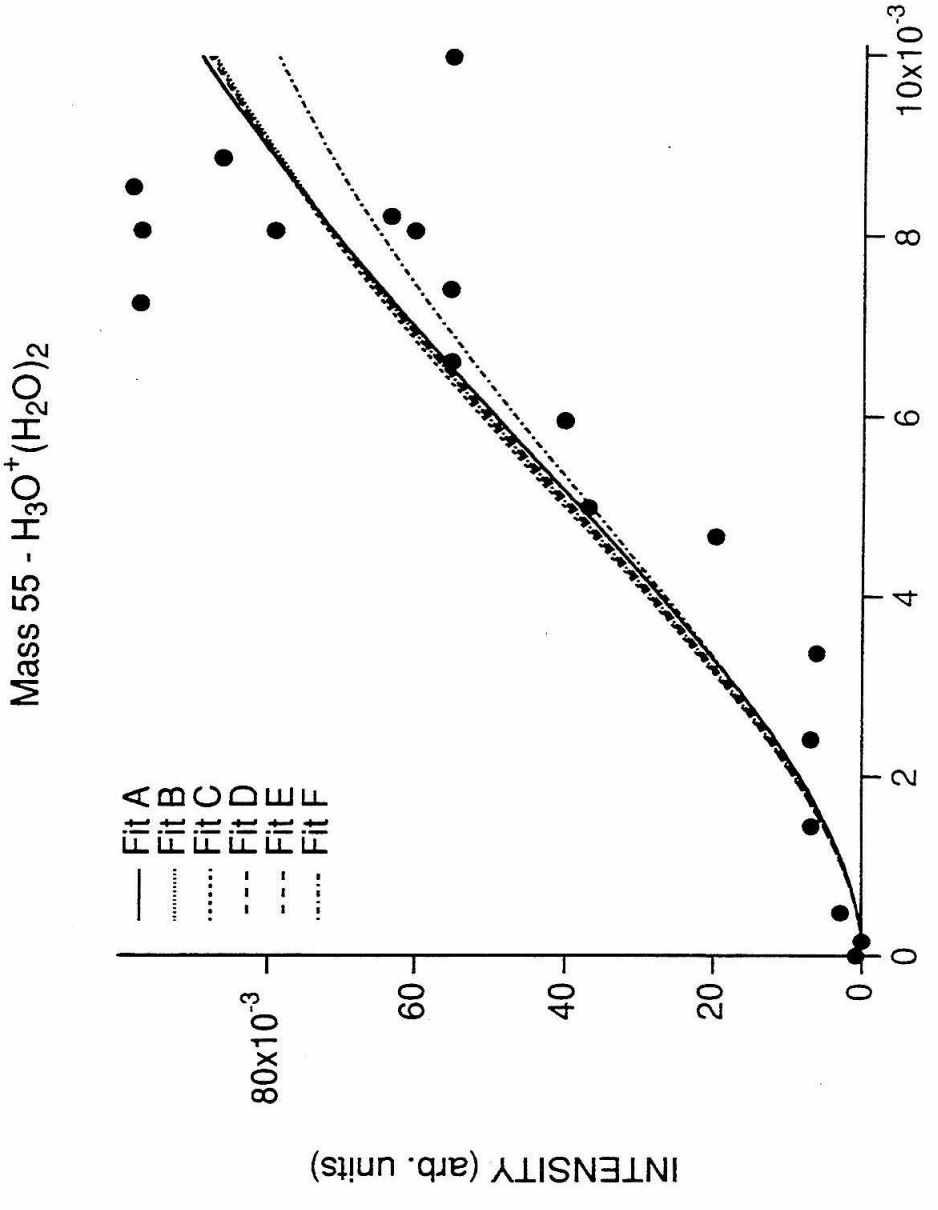
Mass 55 - $H_3O^+(H_2O)_2$
Fit A
Fit B
Fit C
Fit D
Fit E
Fit F
INTENSITY (arb. units)
80x10^{-3}
60
40
20
0
0
2
4
6
8
10x10^{-3}
Pressure (Torr)

Figure 1

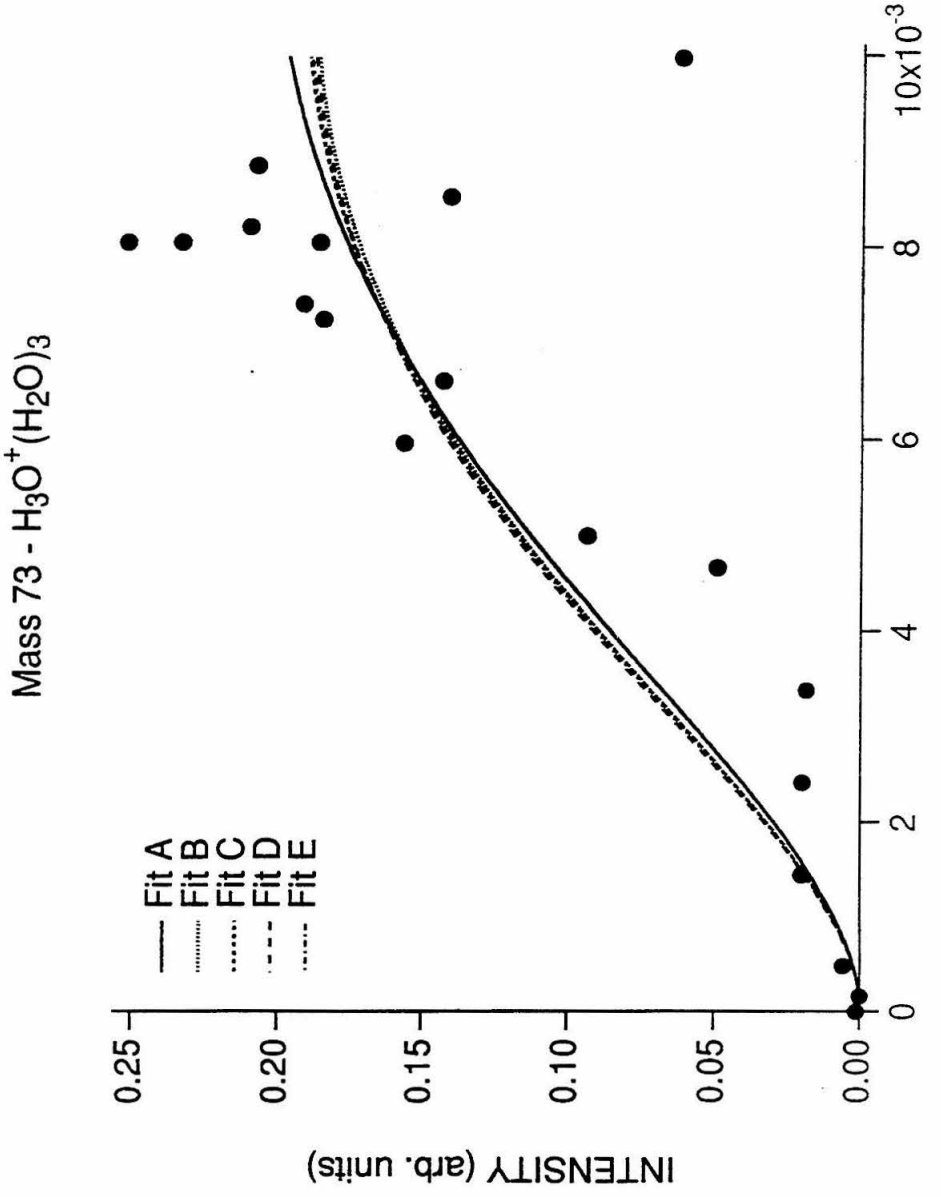
Mass 73 - $H_3O^+(H_2O)_3$
Fit A
Fit B
Fit C
Fit D
Fit E
INTENSITY (arb. units)
0.25
0.20
0.15
0.10
0.05
0.00
0
2
4
6
8
10x10^{-3}
Pressure (Torr)

Figure 2

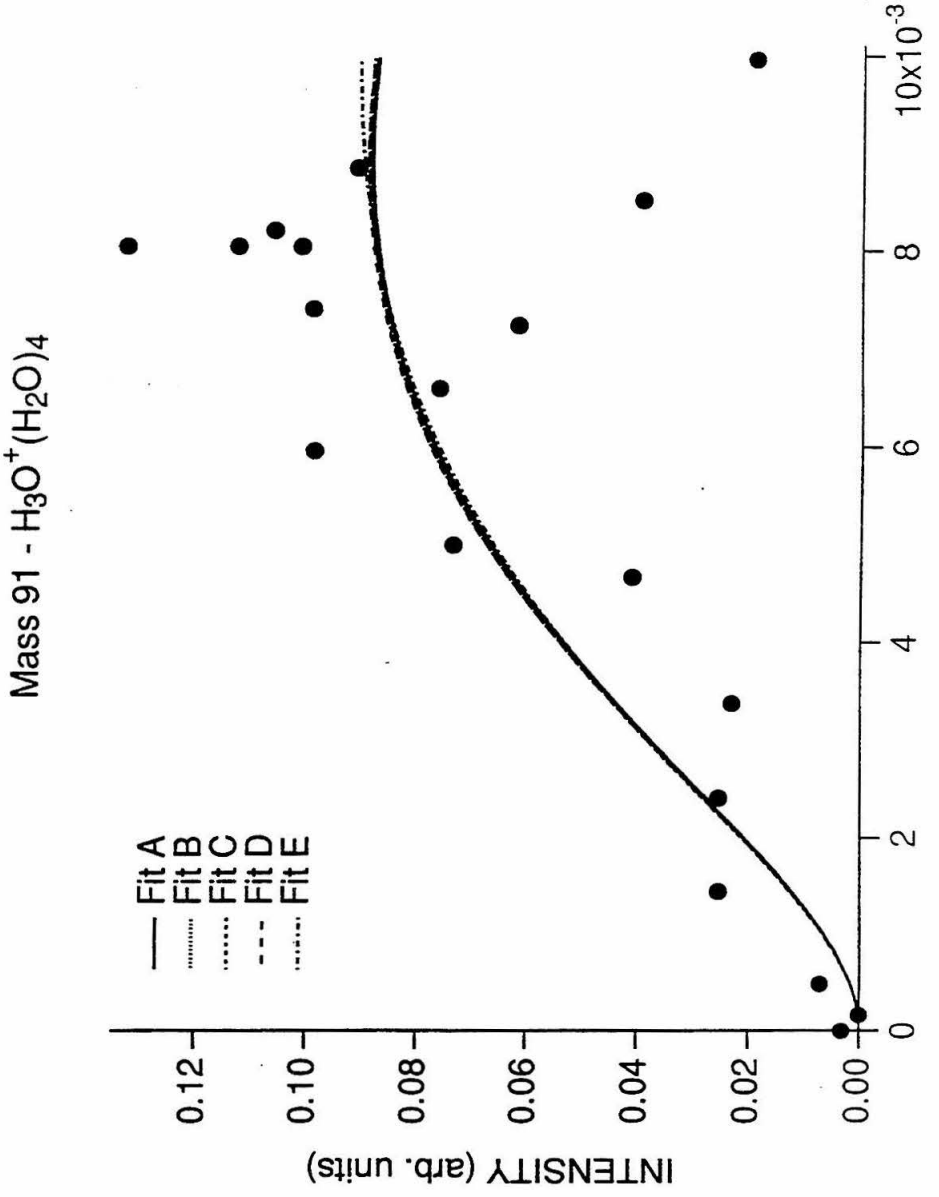
Mass 91 - $H_3O^+(H_2O)_4$
Fit A
Fit B
Fit C
Fit D
Fit E
INTENSITY (arb. units)
0.00
0.02
0.04
0.06
0.08
0.10
0.12
0
2
4
6
8
10x10^{-3}
Pressure (Torr)

Figure 3

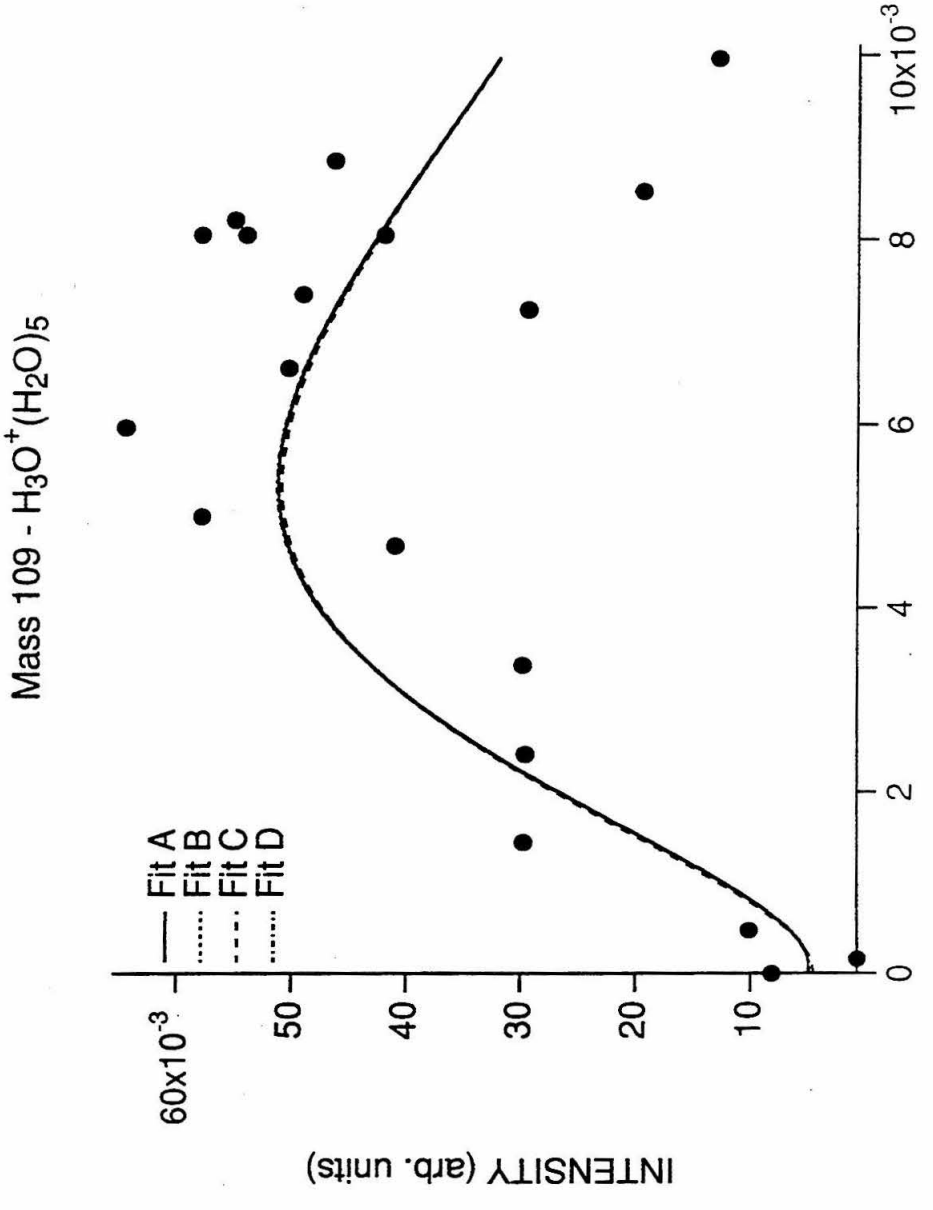
Mass 109 - $H_3O^+(H_2O)_5$
Fit A
Fit B
Fit C
Fit D
60x10^{-3}
50
40
30
20
10
INTENSITY (arb. units)
0
2
4
6
8
10x10^{-3}
Pressure (Torr)

Figure 4

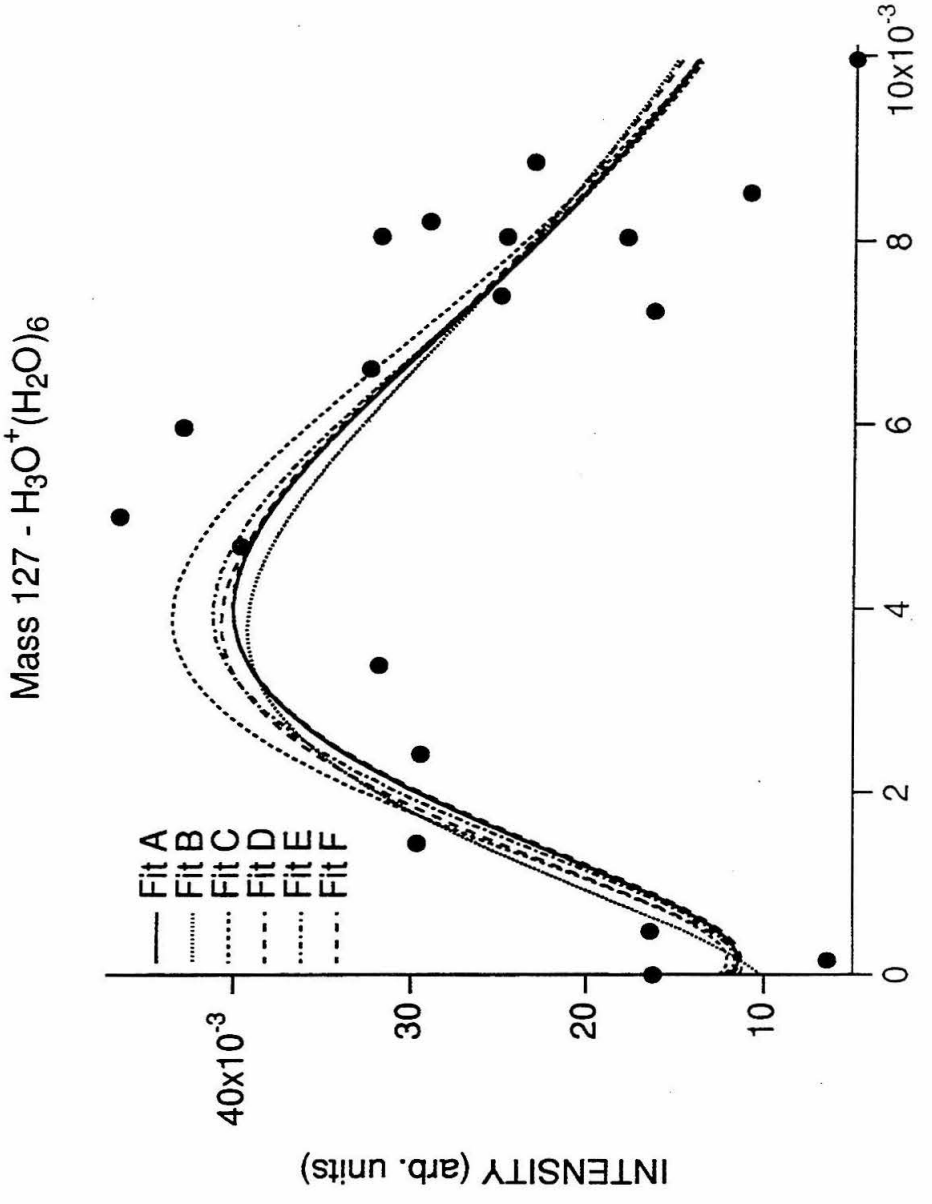
Mass 127 - $H_3O^+(H_2O)_6$
Fit A
Fit B
Fit C
Fit D
Fit E
Fit F
40x10^{-3}
30
20
10
INTENSITY (arb. units)
0
2
4
6
8
10x10^{-3}
Pressure (Torr)

Figure 5

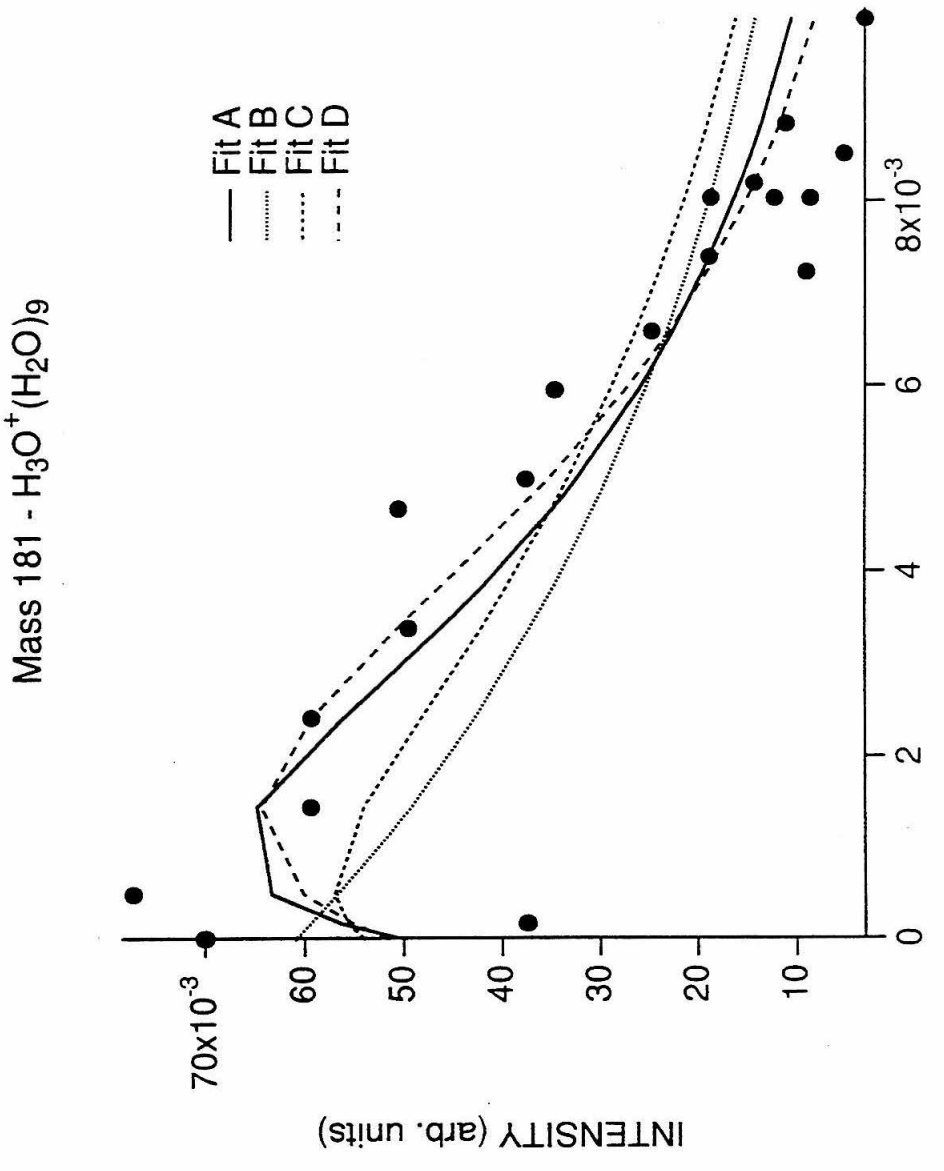
Mass 181 - $H_3O^+(H_2O)_9$
Fit A
Fit B
Fit C
Fit D
INTENSITY (arb. units)
70x10^{-3}
60
50
40
30
20
10
0
2
4
6
8x10^{-3}
Pressure (Torr)

Figure 6

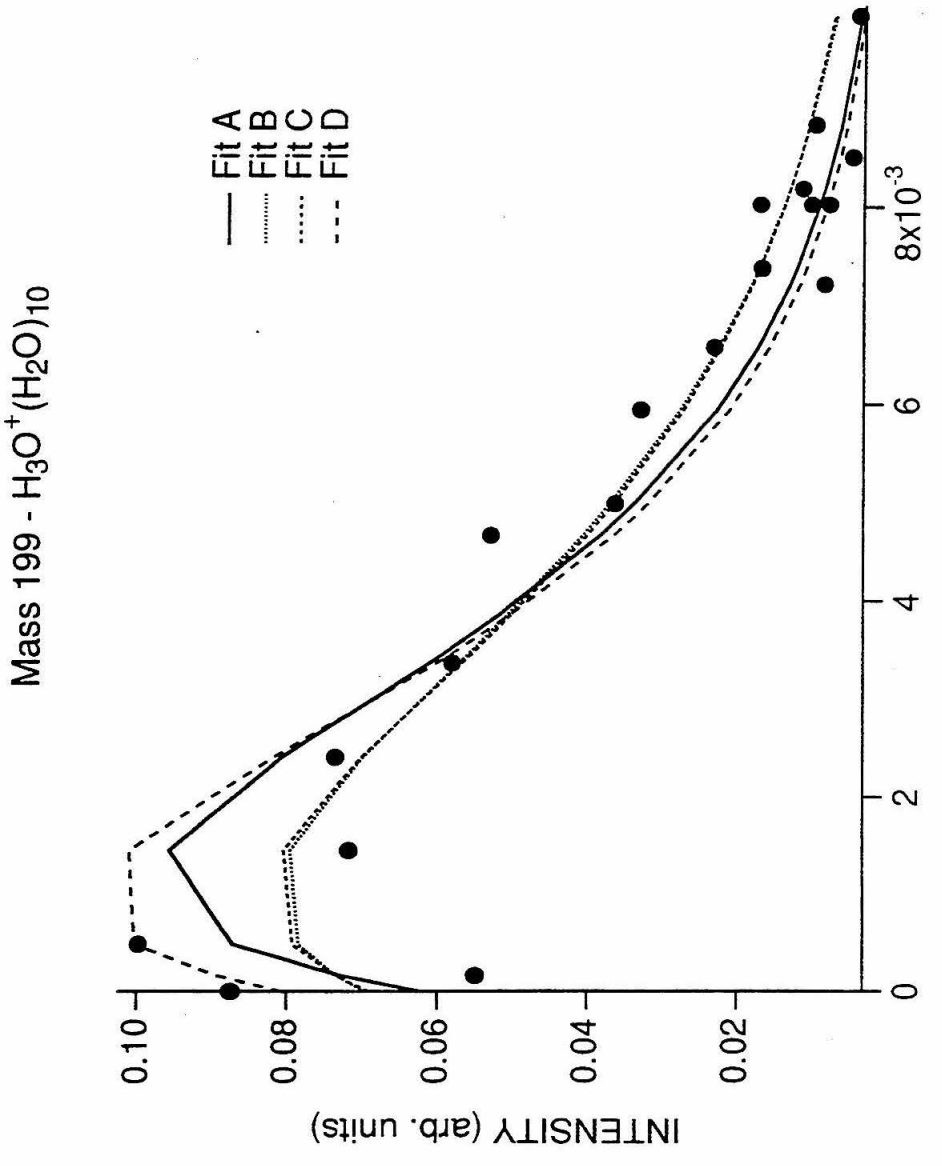
Mass 199 - $H_3O^+(H_2O)_{10}$
Fit A
Fit B
Fit C
Fit D
INTENSITY (arb. units)
0.10
0.08
0.06
0.04
0.02
0
2
4
6
8x10^{-3}
Pressure (Torr)

Figure 7

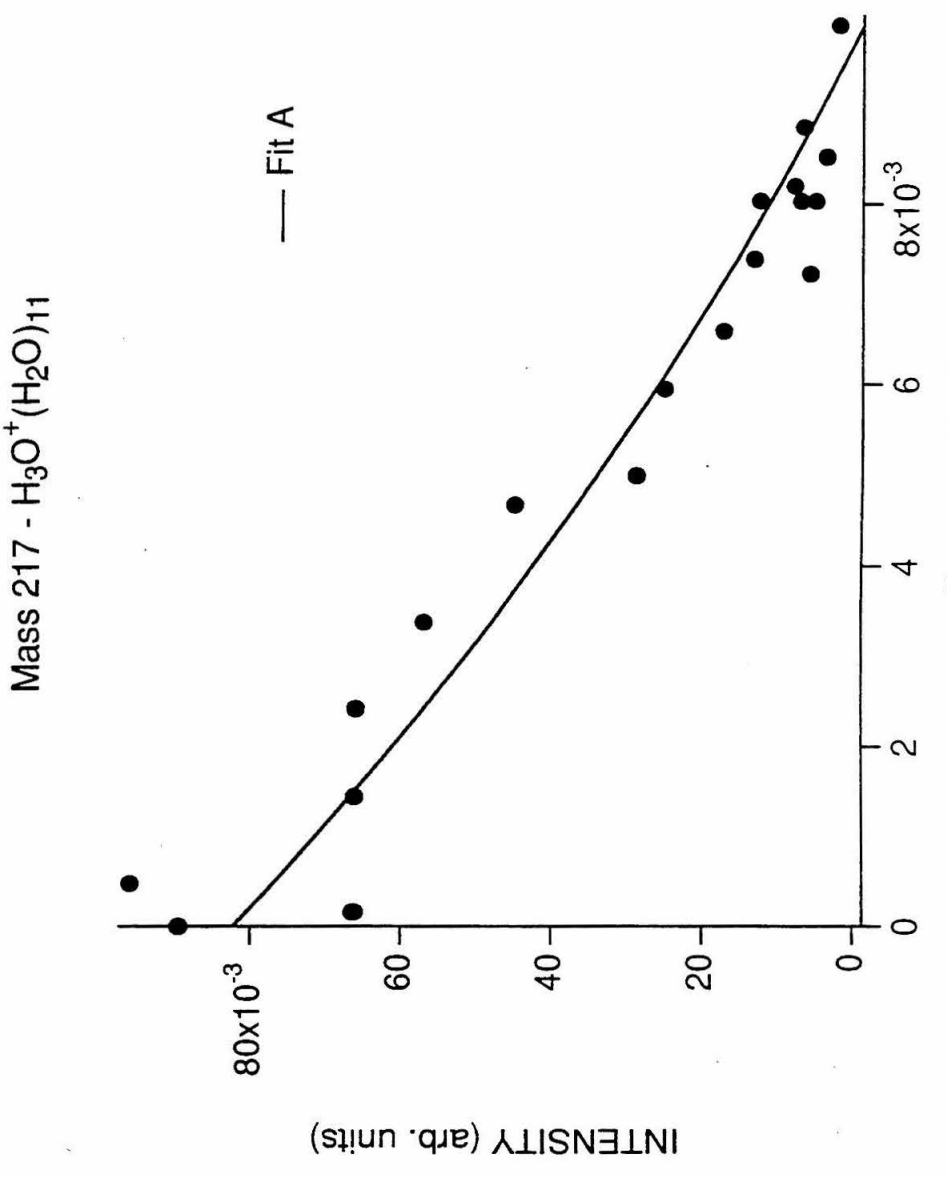
Mass 217 - $H_3O^+(H_2O)_{11}$
— Fit A
INTENSITY (arb. units)
80x10^{-3}
60
40
20
0
0
2
4
6
8x10^{-3}
Pressure (Torr)

Figure 8

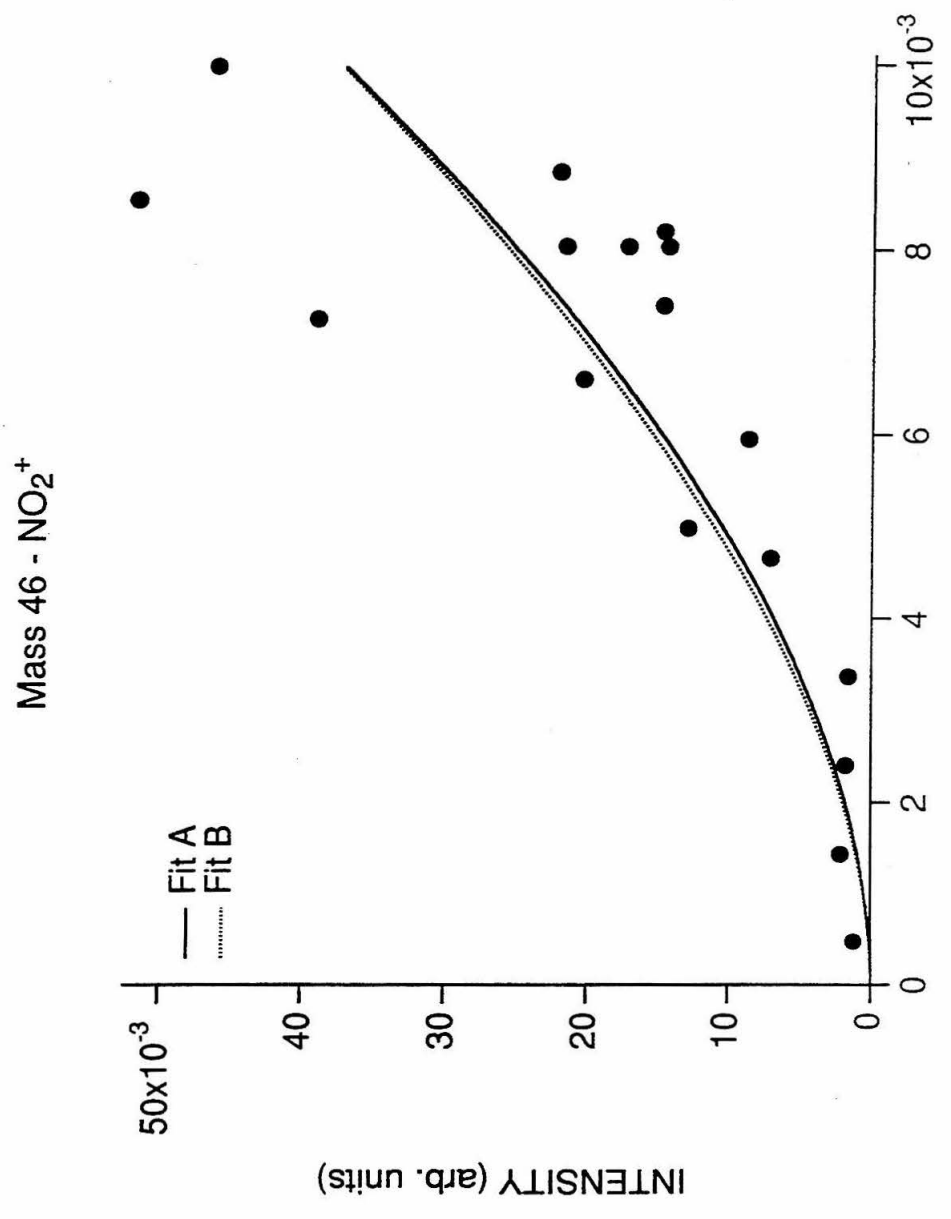
Mass 46 - NO_2^+
Fit A
Fit B
INTENSITY (arb. units)
50x10^{-3}
40
30
20
10
0
0
2
4
6
8
10x10^{-3}
Pressure (Torr)

Figure 9

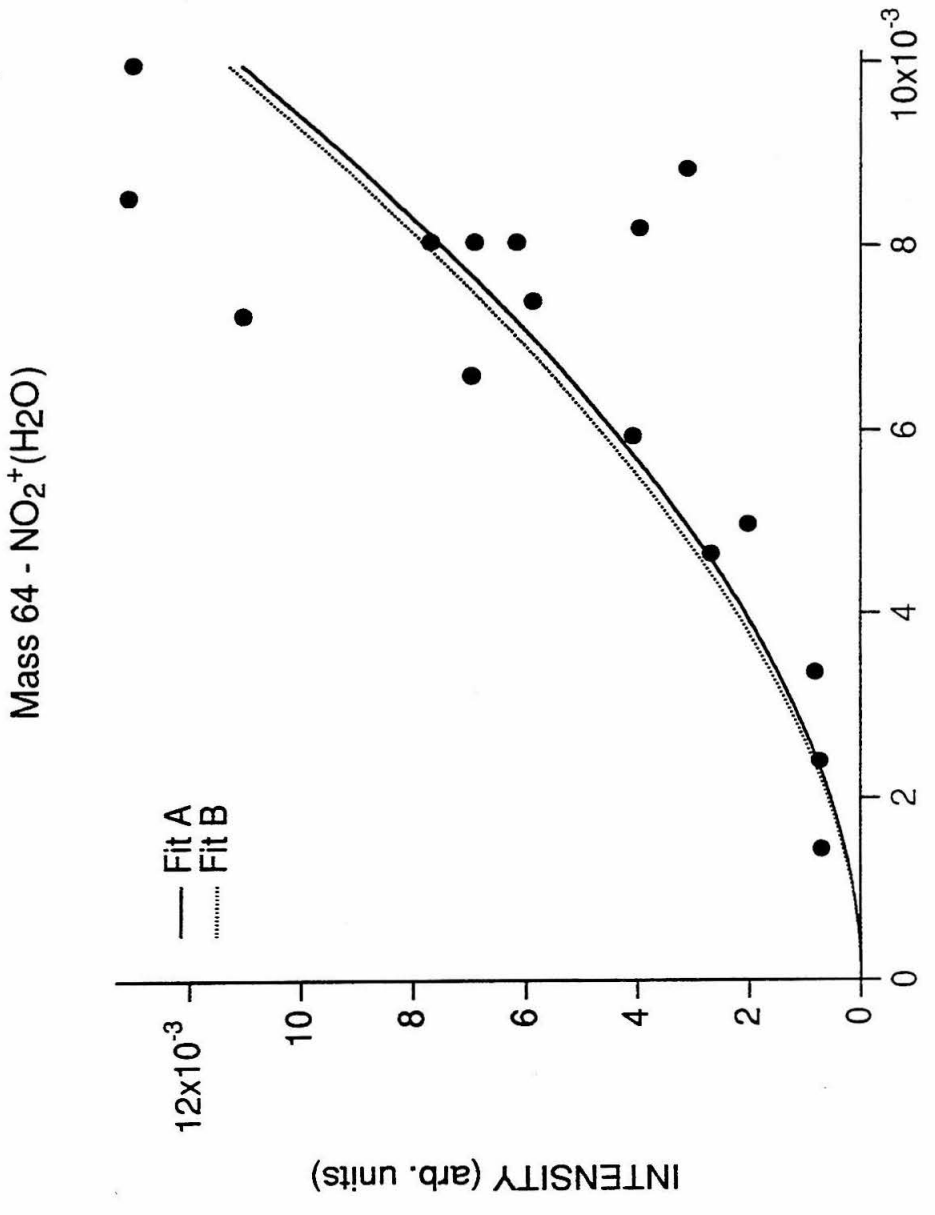
Mass 64 - $NO_2^+(H_2O)$
Fit A
Fit B
INTENSITY (arb. units)
12x10^{-3}
10
8
6
4
2
0
0
2
4
6
8
10x10^{-3}
Pressure (Torr)

Figure 10

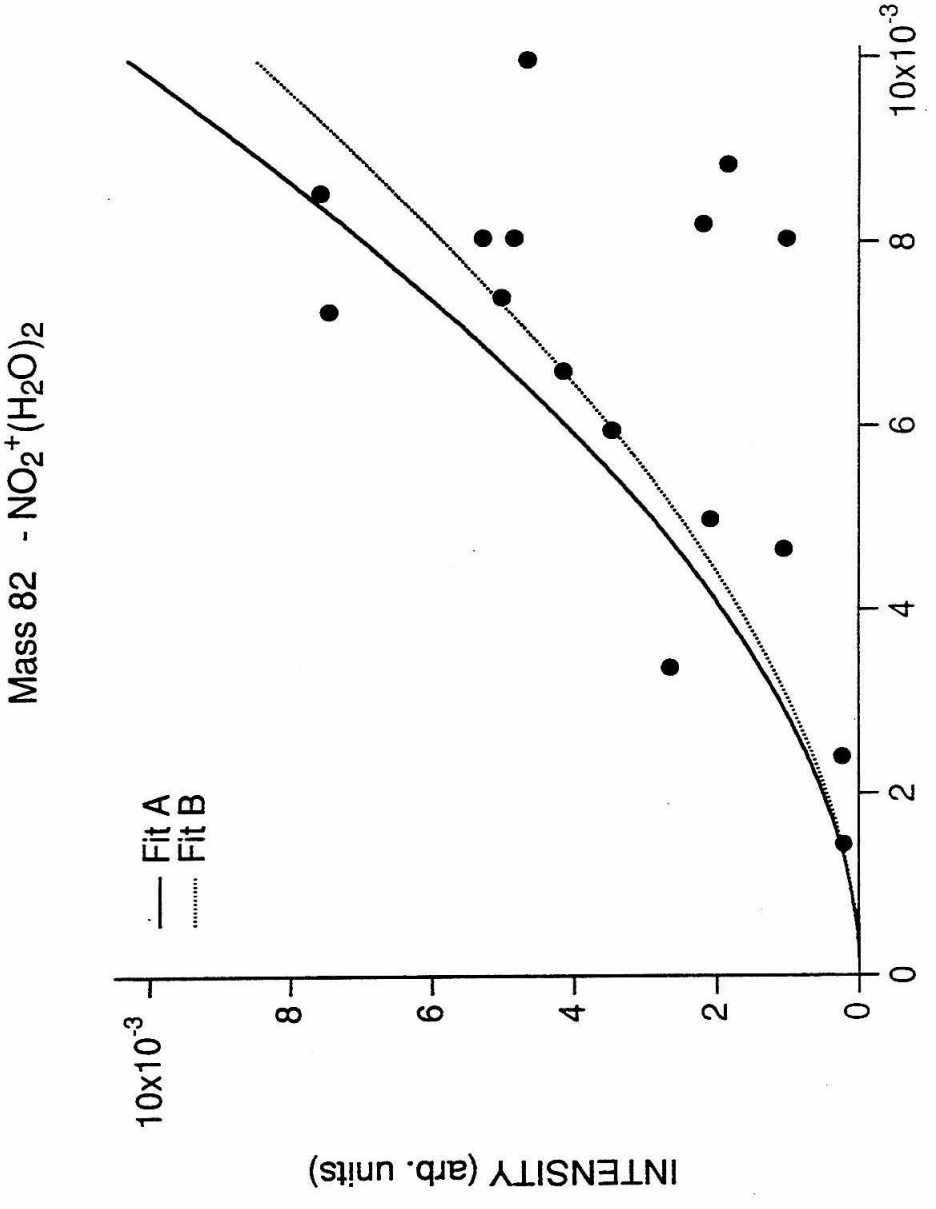
Mass 82 - $NO_2^+(H_2O)_2$
Fit A
Fit B
INTENSITY (arb. units)
10x10^{-3}
0
2
4
6
8
Pressure (Torr)
10x10^{-3}

Figure 11

APPENDIX B

I. Centrifugal Barrier Calculation for the NO_3 Fragment

When $ClONO_2$ dissociates via the Cl + NO_3 pathway some of the NO_3 fragments are formed with sufficient internal energies to undergo spontaneous secondary dissociation, $NO_3 \rightarrow NO_2 + O$. Our calculations predicted a dissociation limit which was 7 kcal/mol greater than the NO_2–O bond energy. Using the following calculation, we investigated whether a centrifugal barrier on the exit channel could account for our discrepancy with reported values of the NO_2–O bond energy.

An effective potential energy surface, $V_{eff}(R)$, for NO_3 arising from the photodissociation of $ClONO_2$ was estimated from the ground state geometry of chlorine nitrate. This effective potential surface was calculated by summing the ground state vibrational, $V(R)$, and the rotational energy, $T(R)$, surfaces of the NO_3 fragment.

$$V_{eff}(R) = V(R) + T(R)$$

The ground state vibrational surface of the O···NO_2 bond was approximated using a Morse potential

$$V(R) = D_e\left(1 - e^{-a(R-R_e)}\right)^2$$

where D_e is the bond strength, R is the distance between the oxygen atom and the center of mass of the NO_2 fragment determined by assuming the ground state geometry of NO_2 [$R_{N,O}$=1.19 Å; $\angle_{ONO}$=134.1°].[2], R_e is the distance between the centers of mass at the minimum of the curve, and $a = \left(\mu_{O\text{-}NO_2} / 2D_e\right)^{1/2}\omega$ in which $\mu_{O\text{-}NO_2}$ is the reduced mass of the oxygen and NO_2 fragment and ω is the fundamental vibrational frequency of NO_3. The values used in these calculations are given in Table I. The assigned fundamental frequencies for the D_{3h} and C_{2v} symmetries are both presented since the structure of NO_3 is not definitively known.

The rotational energy surface was then determined by assuming that all angular momentum in the NO_3 fragment was imparted as the Cl atom recoiled off the NO_3 fragment when the Cl–ONO_2 molecule dissociated. Using a Rigid Radical or Soft Radical Model, we estimated the amount of rotational energy (E_{Rot}) imparted to the NO_3 fragment.[1]

Soft Radical Model

$$\frac{E_{Rot}}{E_{avail}} = \frac{b^2 \mu_{Cl-O}}{I_{NO_3}}$$

Rigid Radical Model

$$\frac{E_{Rot}}{E_{avail}} = \left[\frac{I_{NO_3}}{\mu_{Cl-ONO_2} b^2} + 1 \right]^{-1}$$

E_{avail} is the total amount of available energy [$E_{avail} = h\nu$ - D°(Cl–ONO_2)], b is the impact parameter calculated from the ground state geometry of $ClONO_2$ (see Figure 1), μ_{Cl-O} is the reduced mass between the chlorine atom and oxygen atom, and μ_{Cl-ONO_2} is the reduced mass between the chlorine atom and NO_3 fragment.

The models differ in how the available energy is partitioned into the resultant fragments. The Rigid Radical Model assumes that the Cl atom recoils off a rigid NO_3 fragment so that available energy can be partitioned into only translation or rotation. Alternatively, the Soft Radical Model allows for some of the available energy to be partitioned into internal energy. The Soft Radical Model assumes that the Cl atom recoils off the adjacent oxygen atom which in turn collides with the remainder of the molecule imparting both rotational and vibrational energy in the NO_3 fragment. Complete derivations and explanations of these models are presented elsewhere.[1,3-5]

Using the initial amount of rotational energy in the NO_3 fragment, we calculated the total angular momentum

$$L^2 = 2 I_{NO_3} E_{Rot} .$$

Using the conservation of angular momentum and $I = \mu R^2$, we then determined a rotational energy surface for the dissociation of $O\text{-}NO_2$

$$T(R) = \frac{L^2}{2\mu_{O\text{-}NO_2} R^2}.$$

The vibrational and rotational potential energy surfaces were then summed together to produce effective potential energy surfaces. The calculated surfaces are shown in Figures 2-5.

II. References

1. L.J. Butler, UC Berkeley, Ph.D. Thesis (1985).
2. F.A. Cotton, G. Wilkinson, *Advanced Inorganic Chemistry,* J. Wiley & Sons, Inc., New York (1988); 321.
3. G.E. Busch, K.R. Wilson, *J. Chem. Phys.* **56**, 3626 (1972).
4. A.F. Tuck, *J. Chem. Soc., Fraday Trans II* **73**, 689 (1977).
5. C.S. Effenhauser, P. Felder, J.R. Huber, *J.Phys. Chem.* **94**, 296 (1990).
6. H.F. Davis, Y.T. Lee, *J. Phys. Chem.* **97,** 2172 (1993).
7. T. Ishiwata, I. Fugiwara, Y. Naruge, K. Obi, and I. Tanaka, *J. Phys. Chem.* **87**, 1349 (1983).
8. T. Ishiwata, I. Tanaka, K. Kawaguchi, and E. Hirota, *J. Chem. Phys.* **82**, 2196 (1985).
9. R.R. Friedl and S.P. Sander, *J. Phys. Chem.* **91**, 2721 (1987).
10. B. Kim, B.L. Hammond, W.A. Lester, Jr., and H.S. Johnston, *Chem. Phys. Lett.* **168**, 131 (1990).
11. B. Kim, P.L. Hunter, H.S. Johnston, *J. Chem. Phys.* **96**, 4057 (1992).

TABLE I: Calculation Parameters

D_e [a]	48.55 kcal/mol		
R_e [b]	1.24 Å		
$\mu_{O\text{-}NO_2} = \frac{m_O m_{NO_2}}{m_O + m_{NO_2}}$	11.87 amu		
$\mu_{Cl\text{-}ONO_2} = \frac{m_{Cl} m_{NO_3}}{m_{Cl} + m_{NO_3}}$	22.37 amu		
$\mu_{Cl\text{-}O} = \frac{m_{Cl} m_O}{m_{Cl} + m_O}$	10.98 amu		
I_{NO_3}	83.71 amu Å^2		
b	1.30 Å		
E_{avail}	75 kcal/mol		
$h\nu_{248nm}$	115 kcal/mol		
D°(Cl-NO_3)	40 kcal/mol		
$\omega = 2\pi\nu/h$	D_{3h} [b,c,d]	$\nu = 1276$	C_{2v} [e,c,d] $\nu = 1519$
	ν_1 a_1' sym. N-O str.	1060	ν_1 a_1 sym. N-O str. 1051
	ν_3 e' degen. N-O str.	1492	ν_2 a_1 sym. N-O str. 1498
			ν_5 b_1 asym. N-O str. 2008

[a] Ref. 6

[b] Ref. 7-9

[c] Determined by averaging stretching frequencies (ν) for a particular symmetry group.

[d] All frequencies reported in cm^{-1}.

[e] Ref. 10, 11

III. FIGURE CAPTIONS

Figure 1. Ground state geometry of $ClONO_2$ showing the location of the c.m. of NO_3 and the impact parameter, *b*.

Figure 2. Effective potential energy surface for O-NO_2 using the rigid radical model and the fundamental frequencies for D_{3h} symmetry.

Figure 3. Effective potential energy surface for O-NO_2 using the soft radical model and the fundamental frequencies for D_{3h} symmetry.

Figure 4. Effective potential energy surface for O-NO_2 using the rigid radical model and the fundamental frequencies for C_{2v} symmetry.

Figure 5. Effective potential energy surface for O-NO_2 using the soft radical model and the fundamental frequencies for C_{2v} symmetry.

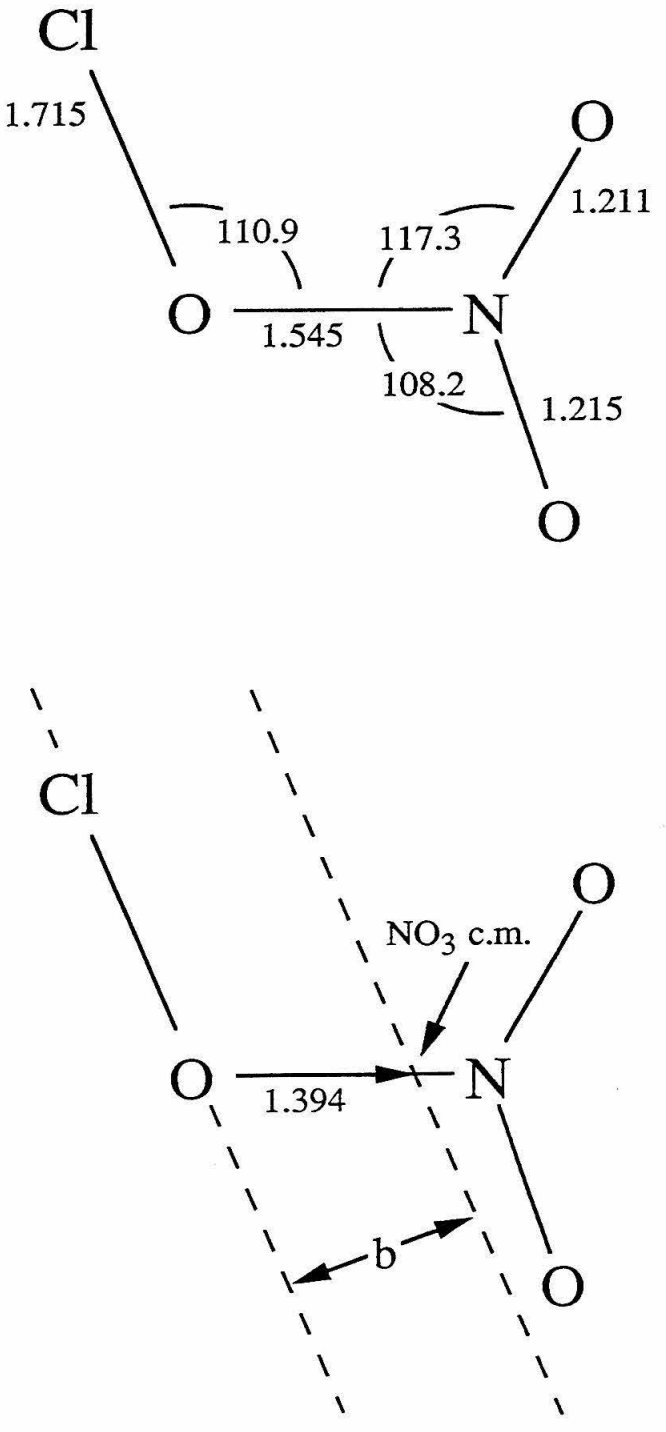
Cl
1.715
O
1.211
110.9
117.3
O
1.545
N
108.2
1.215
O
Cl
O
NO3 c.m.
O
1.394
N
b
O

Figure 1

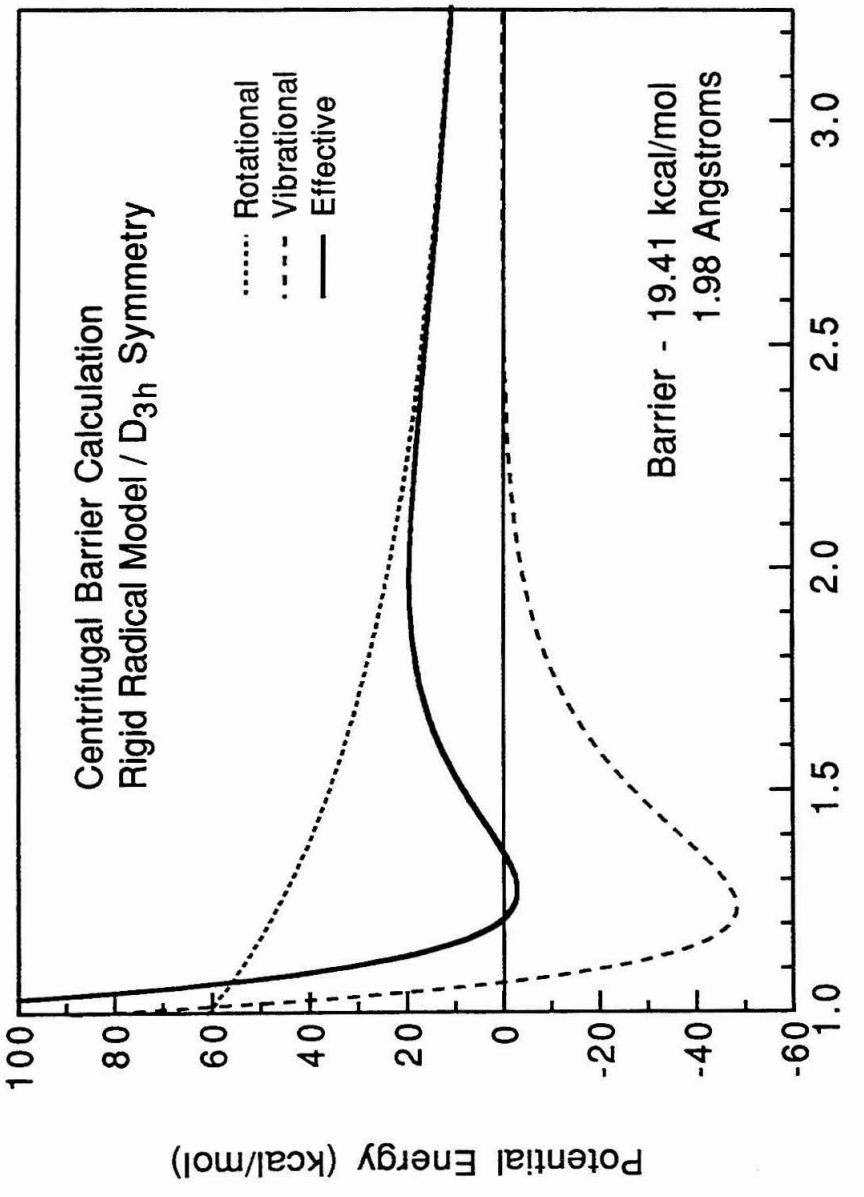
Centrifugal Barrier Calculation
Rigid Radical Model / D_{3h} Symmetry
Rotational
Vibrational
Effective
Barrier - 19.41 kcal/mol
1.98 Angstroms
Potential Energy (kcal/mol)
100
80
60
40
20
0
-20
-40
-60
1.0
1.5
2.0
2.5
3.0
O-NO_2 Bond Distance (Angstroms)

Figure 2

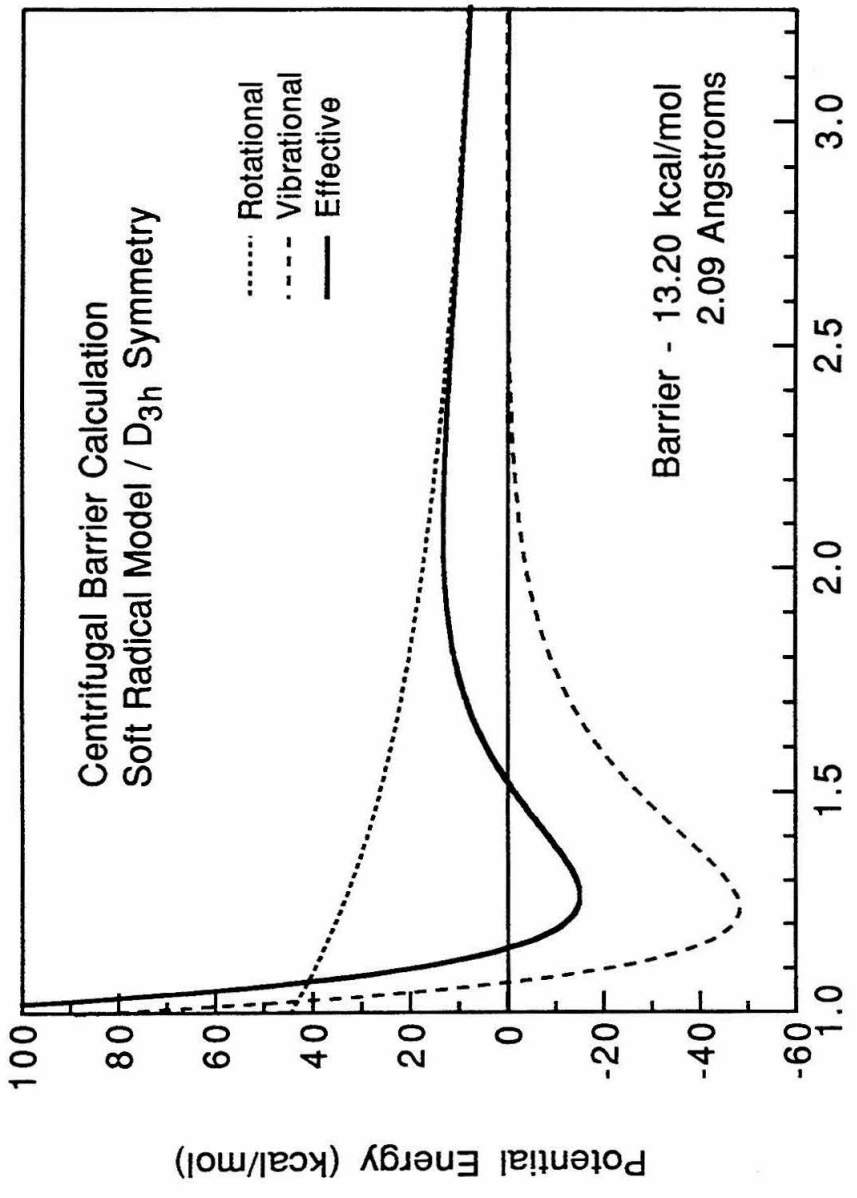
Centrifugal Barrier Calculation
Soft Radical Model / D_{3h} Symmetry
Rotational
Vibrational
Effective
Barrier - 13.20 kcal/mol
2.09 Angstroms
Potential Energy (kcal/mol)
100
80
60
40
20
0
-20
-40
-60
1.0
1.5
2.0
2.5
3.0
O-NO_2 Bond Distance (Angstroms)

Figure 3

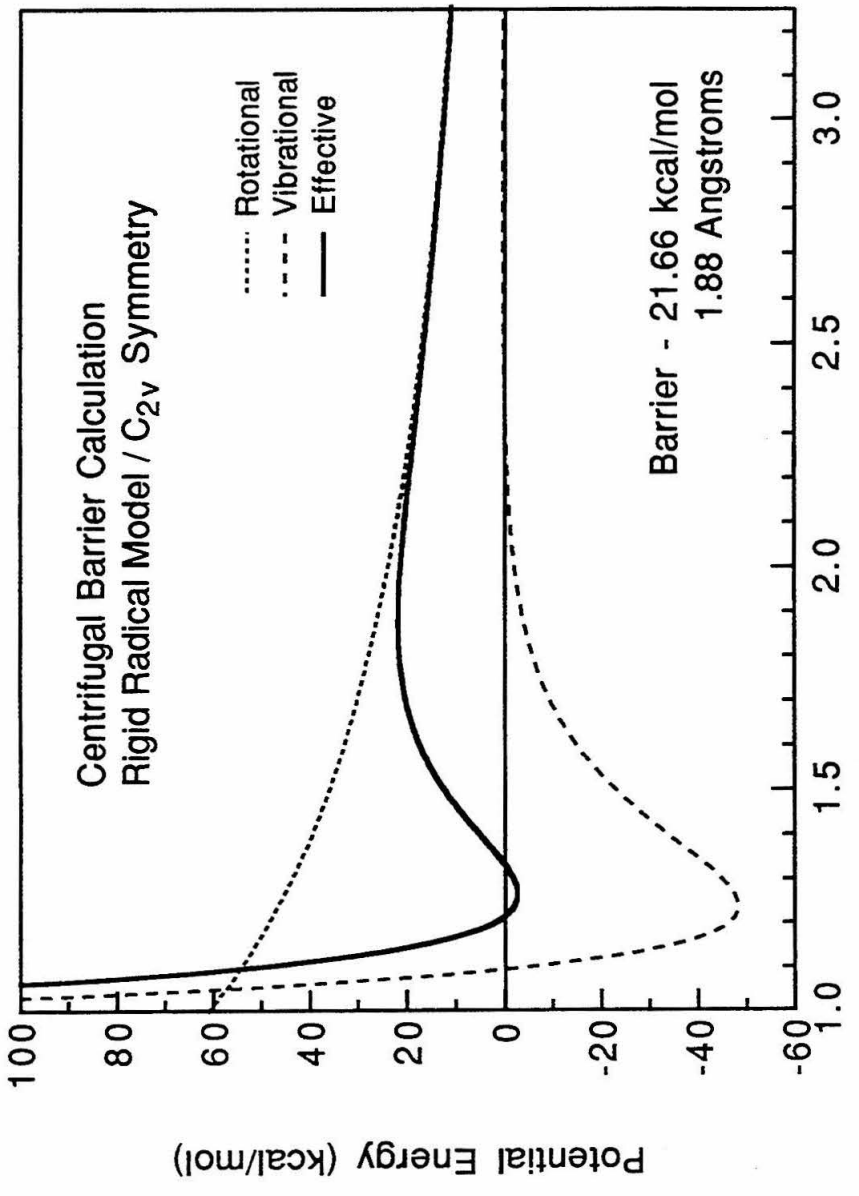
Centrifugal Barrier Calculation
Rigid Radical Model / C_{2v} Symmetry
Rotational
Vibrational
Effective
Barrier - 21.66 kcal/mol
1.88 Angstroms
Potential Energy (kcal/mol)
100
80
60
40
20
0
-20
-40
-60
1.0
1.5
2.0
2.5
3.0
O-NO_2 Bond Distance (Angstroms)

Figure 4

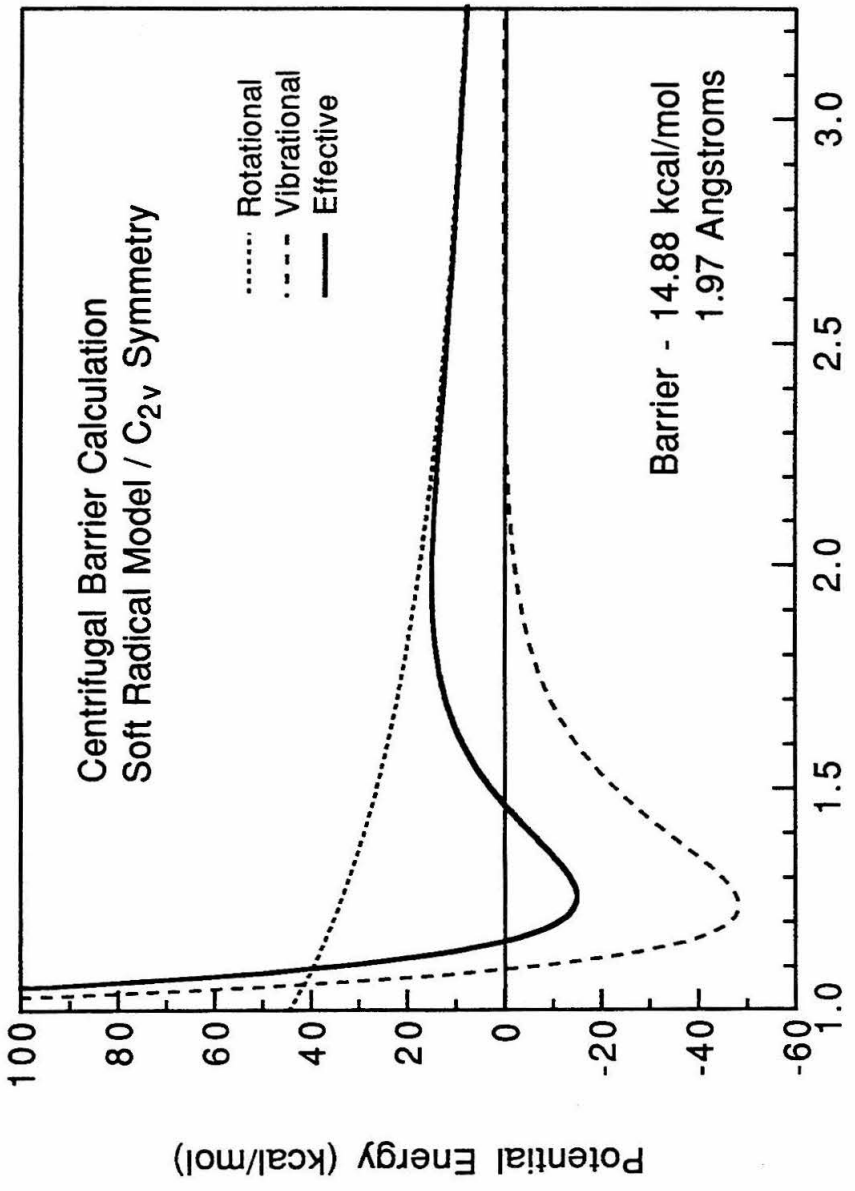
Centrifugal Barrier Calculation
Soft Radical Model / C_{2v} Symmetry
Rotational
Vibrational
Effective
Barrier - 14.88 kcal/mol
1.97 Angstroms
Potential Energy (kcal/mol)
O-NO_2 Bond Distance (Angstroms)
100
80
60
40
20
0
-20
-40
-60
1.0
1.5
2.0
2.5
3.0

Figure 5

APPENDIX C

I. Calculation to Determine the Orientation of the Electronic Transition Moment in $ClONO_2$

The orientation of the electronic transition moment in a parent molecule can be determined from the anisotropy parameter, β, using a simple recoil model. Assuming that the parent molecule dissociates instantaneously upon absorbing the photon and that the kinetic energy of dissociation is very large compared to the kinetic energy of rotation, β has the form

$$\beta = 2P_2(\cos\chi)$$

where P_2 is the second order Legendre polynomial

$$P_2(\cos\chi) = \frac{3\cos^2(\chi) - 1}{2}$$

and χ is the angle between the electronic transition moment and the recoil axis of the two counterfragments in the c.m. frame of reference.[1] The recoil axis is oriented along the line intersecting the centers of mass of the two product fragments. Thus, the two channels, Cl + NO_2 and Cl + NO_3, possess different recoil axes (see Figure 1).

Using the β values determined from the angular distributions, we solve for corresponding values of χ. The transition moment resides on a cone with a half-angle χ centered about the recoil axis, since any azimuthal orientation of the transition moment is possible. If a single electronic transition in the chlorine nitrate accounts for both channels, the transition moment must lie at the intersection of the two cones corresponding to the two channels.

At 248 nm, the angular distribution of the products from the Cl + NO_3 channel is characterized by a β of 0.5 and thus has a χ angle of 45°. The ClO + NO_2 channel, alternatively, has a β of 1.3 and a χ angle of 29°. Using the ground state geometry of chlorine nitrate, the intersection of the two cones is located and is found to lie essentially in the plane of the molecule (see Figure 2). In fact, if an in-plane transition is assumed and

the β and χ values from the $ClO + NO_2$ channel are used to determine the β and χ values for the $Cl + NO_3$ channel, a χ angle of 32° and a β of 1.2 are predicted (see Figure 1). These values all well within the error limits of our experiment.

At 193 nm, however, the $ClO + NO_2$ channel has a β of 0.25 and a χ angle of 50°, and the $Cl + NO_3$ channel has a β of 0.5 and a χ value of 45°. In order for the experimental β values to fit simultaneously, the transition moment must be located out of the plane of the molecule (see Figure 3). The experimental data from the $ClO + NO_2$ channel predict χ angles of 37° or 63° (β=0.9 or -0.4) for an in-plane electronic transition. The two angles represent the two possible projections of χ in the plane of the molecule.

II. References

1. G.E. Busch, K.R. Wilson, *J. Chem. Phys.* **56**, 3638 (1972).

2. R.N. Zare, *Mol. Photochem.* **4**, 1 (1972).

3. S. Yang, R. Bersohn, *J. Chem. Phys.* **61**, 4400 (1974).

III. Figure Captions

Figure 1. Ground state geometry of $ClONO_2$ showing the orientations of the transition moment cones which were calculated using the β values determined from the 248 nm experiment.

Figure 2. Ground state $ClONO_2$ showing the geometry the in-plane transition at 248 nm.

Figure 3. Ground state geometry of $ClONO_2$ showing the orientations of the transition moment cones which were calculated using the β values determined from the 193 nm experiment.

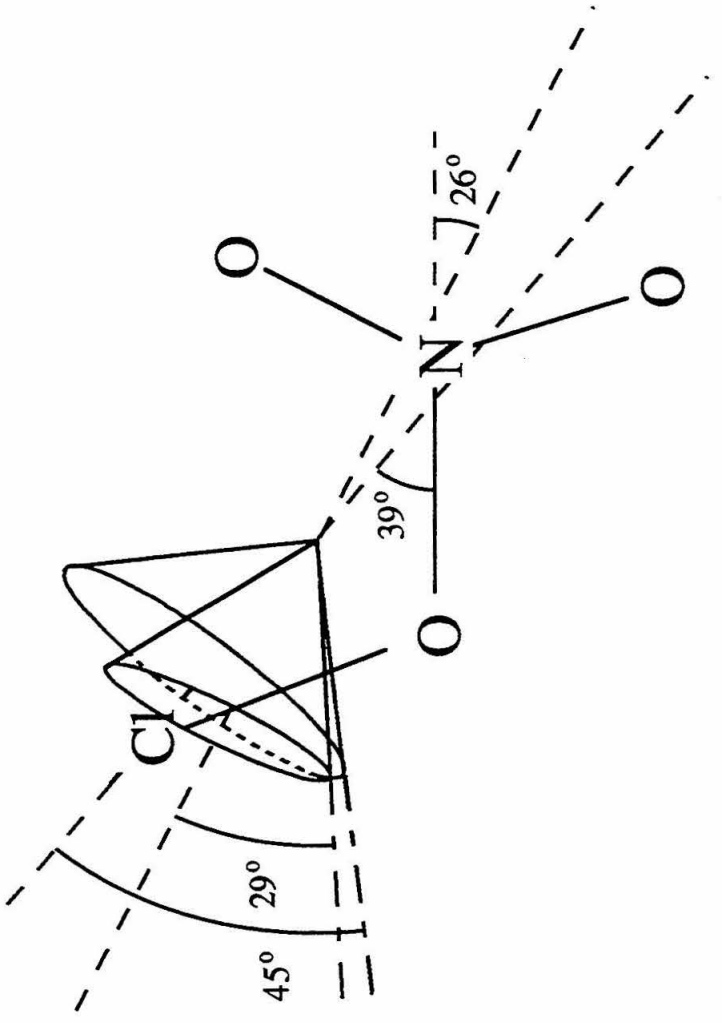

Figure 1

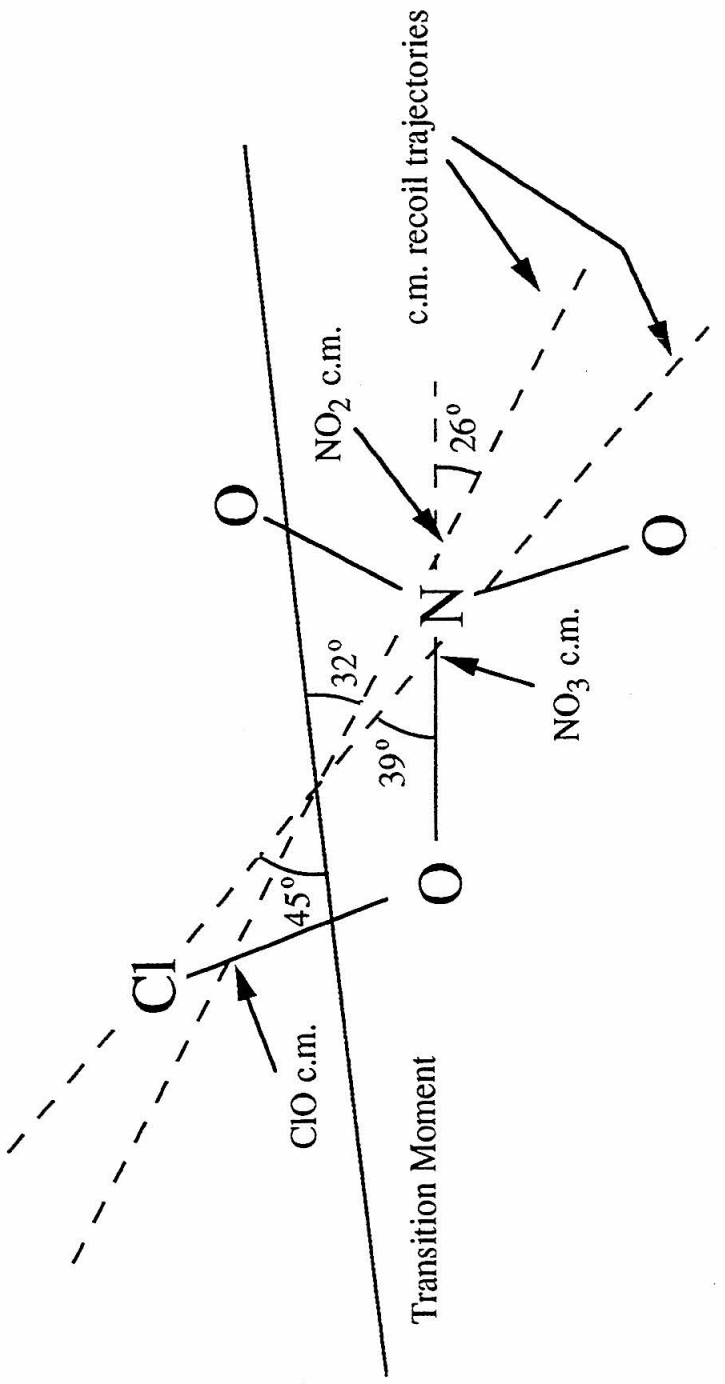
c.m. recoil trajectories
NO_2 c.m.
26°
O
N
O
32°
39°
NO_3 c.m.
248 nm
Cl
45°
O
ClO c.m.
Transition Moment

Figure 2

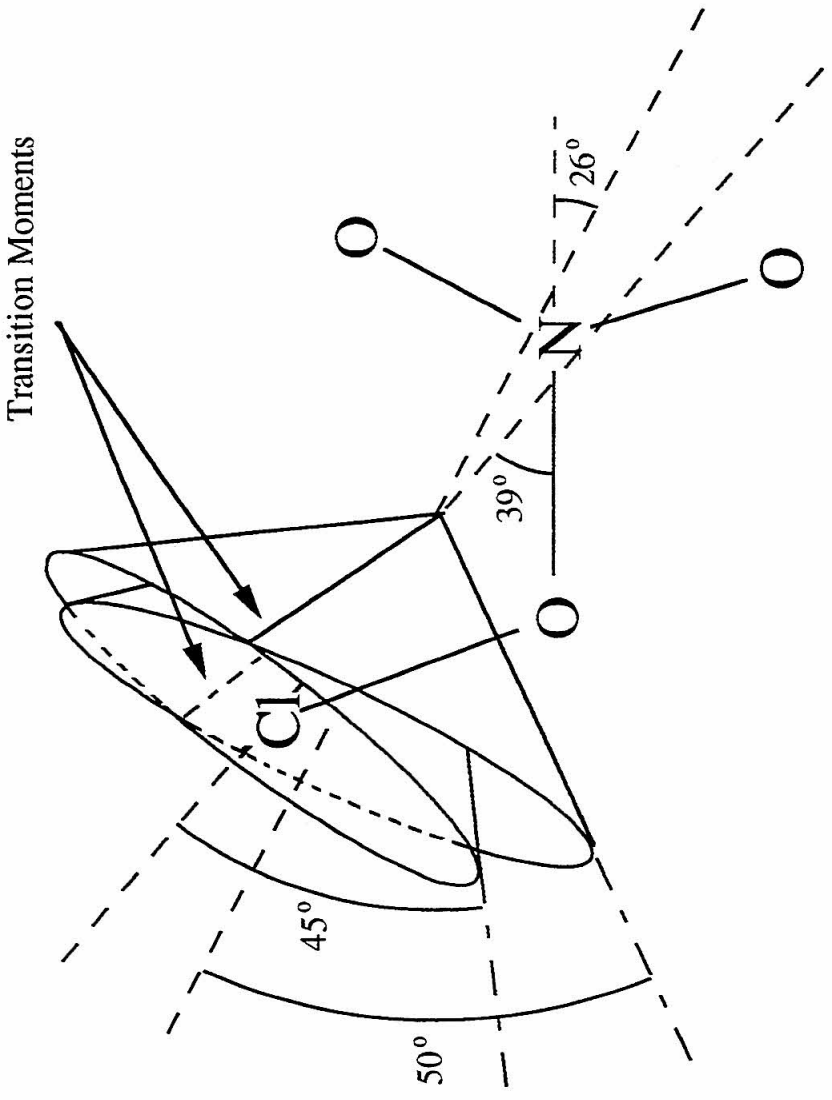

Figure 3